

UCH-FC  
DOC-F  
N 144  
C. 1



# SPATIALLY LOCALIZED MODES IN DISCRETE NONLINEAR OPTICAL SYSTEMS

Tesis

entregada a la

Universidad de Chile

en cumplimiento parcial de los requisitos

para optar al grado de

Doctora en Ciencias con mención en Física

Facultad de Ciencias

por

**Uta Naether**

Director de Tesis: **Dr. Mario I. Molina Galvez**

Codirector de Tesis: **Dr. Rodrigo A. Vicencio Poblete**

FACULTAD DE CIENCIAS  
UNIVERSIDAD DE CHILE  
INFORME DE APROBACIÓN  
TESIS DE DOCTORADO

Se informa a la Escuela de Postgrado de la Facultad de Ciencias que la Tesis de Doctorado presentada por la candidata

**Uta Naether**

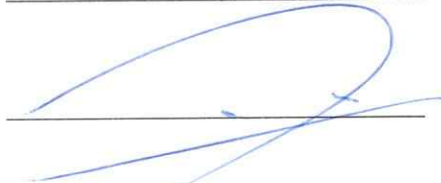
ha sido aprobada por la Comisión de Evaluación de la Tesis como requisito para optar al grado de Doctora en Ciencias con mención en Física, en el examen de Defensa de Tesis rendido el día 23 de Octubre de 2012.

**Directores de Tesis**

Dr. Mario Molina



Dr. Rodrigo Vicencio

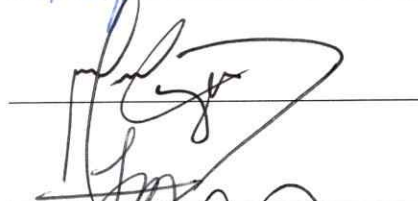


**Comisión de Evaluación de la Tesis**

Dr. Felipe Barra (Presidente)



Dr. Marcel Clerc



Dr. Luis Morales-Molina



Dr. Carlos Saavedra

## BIOGRAFÍA



Nací en 1980 y pasé mi infancia y mi vida escolar en Freiberg. Antes de comenzar mi formación universitaria hice un viaje a Sudamérica que duró un año, en el cual realicé diferentes actividades que me permitieron recorrer varios países. Durante ese viaje me topé con un libro de difusión científica que me ayudó a decidir mi futuro académico, así, de regreso en Alemania, me inscribí en la Universidad de Potsdam en el programa de física, donde permanecí por dos años. Al año siguiente me dediqué a trabajar en un taller de escultura en fierro y en forma paralela di clases particulares de matemáticas y física. El año 2004 me inscribí en la Universidad de Humboldt en Berlín para retomar mis estudios de física. A medida que iba avanzando, iba interesándome especialmente en el tema de la dinámica no lineal, fue este interés el que me llevó a presentar una tesis sobre la difusión de ondas epidémicas, con la que obtuve mi diploma el año 2008. Fue mi interés por seguir estudiando, como también el de volver a Sudamérica, lo que me hizo llegar a la Universidad de Chile; más específicamente, tenía interés en continuar estudiando sistemas no lineales, pero vistos a través de otras materias. En agosto del 2008 me integré al grupo de Óptica no lineal del Departamento de física donde fui muy bien recibida por los profesores Mario Molina y Rodrigo Vicencio con quienes he trabajado hasta ahora. Durante este período también hice una estadía en el Instituto Max Planck en Dresden donde trabajé con el profesor Magnus Johanson, y una pasantía en la Universidad de Jena en la cual estuve trabajando en el grupo del profesor Alex Szameit. Actualmente estoy defendiendo mi tesis que es la conclusión de estos cuatro años en Chile.

## AGRADECIMIENTOS

Deseo agradecer a todos los que no solamente hicieron posible, si no también una experiencia muy valiosa estos años del Doctorado. Desde que llegué al grupo de Óptica no lineal de la Facultad de Ciencias en la Universidad de Chile me sentí muy acogida. Además del gran apoyo académico Mario Molina y Rodrigo Vicencio me brindaron su amistad. Compartir la oficina con Santiago Rojas y Alejandro Martínez no solamente causó discusiones motivantes, si no también momentos de relaxo bien apreciados. Las discusiones con Magnus Johansson me enseñaron a poner mucha más dedicación a problemas, que a primera vista pueden parecer detalles, pero no lo son. El poder relacionar mis conocimientos y horizonte mas teórico con la realidad experimental se lo debo a Alexander Szameit y su grupo. A mi familia y mis amigos les debo muchísimo por su paciencia y por su comprensión y, finalmente, a Catalina no le puedo agradecer suficientemente todos los periódicos y las canciones mexicanas.

Mi permanencia en el programa fue posible gracias a una beca de Doctorado de CONICYT, quienes ademas me permitieron participar en una conferencia internacional. El Programa ICM, Proyecto Cod. P10-030-F financió el termino de mi tesis y me dió la posibilidad de participar en una conferencia. Agradezco la ayuda del Centro de Óptica y Fotónica, financiado a su vez por CONICYT a través del proyecto Basal No. FB0824/2008, que me permitió la participación en conferencias, y a Becas Chile por la posibilidad de una pasantía en Jena. Además, este trabajo ha sido parcialmente financiado por FONDECYT, proyectos No. 1070897, 1080374, 1110142 y 1120123.

# Contents

|  |           |
|--|-----------|
| List of Figures  | viii      |
| <b>1. Introduction</b>   | <b>3</b>  |
| <b>2. The discrete nonlinear Schrödinger equation</b>                | <b>9</b>  |
| 2.1. The Kerr nonlinearity . . . . .                                 | 12        |
| 2.2. The saturable nonlinearity . . . . .                            | 15        |
| 2.3. Linear properties and discrete diffraction . . . . .            | 19        |
| 2.4. Stationary and nonlinear localized solutions . . . . .          | 23        |
| <b>3. Techniques</b>   | <b>26</b> |
| 3.1. Stability Analysis . . . . .                                    | 26        |
| 3.2. Constraint method . . . . .                                     | 30        |
| <b>4. Fano resonances</b>  | <b>34</b> |
| 4.1. Linear Fano resonances in Split-ring resonator arrays . . . . . | 35        |
| 4.1.1. Magnetoinductive defects and Fano resonances . . . . .        | 38        |
| 4.1.2. Single external inductive defect: First case . . . . .        | 42        |

---

|   |            |
|---|------------|
| 4.1.3. Single external inductive defect: Second case . . . . .          | 44         |
| 4.2. Nonlinear Fano-Resonances in saturable waveguide arrays . . . . .  | 47         |
| <b>5. Disorder</b>  | <b>54</b>  |
| 5.1. Anderson localization . . . . .                                    | 54         |
| 5.2. Disorder in finite nonlinear arrays . . . . .                      | 55         |
| 5.3. Influence of a disordered boundary . . . . .                       | 68         |
| <b>6. Mobility</b>  | <b>74</b>  |
| 6.1. 1D systems . . . . .   | 75         |
| 6.2. Directional mobility of discrete solitons in 2D lattices . . . . . | 81         |
| 6.2.1. Description of PN surfaces . . . . .                             | 87         |
| 6.2.2. Mobility dynamics for isotropic lattices . . . . .               | 91         |
| <b>7. Vortices in discrete saturable arrays</b>                         | <b>97</b>  |
| 7.1. From discrete linear vortices to combined solutions . . . . .      | 98         |
| 7.2. Mode families . . . . .  | 101        |
| <b>8. Conclusion and Outlook</b>  | <b>107</b> |
| <b>Bibliography</b>   | <b>111</b> |
| <b>A. Multidimensional Newton Raphson</b>                               | <b>126</b> |
| <b>B. Finding the Hamiltonian for the symplectic integrator</b>         | <b>128</b> |
| <b>C. Fs-laser written waveguides</b>                                   | <b>131</b> |

---

D. Publications

133

## List of Figures

|   |    |
|---|----|
| 2.1. Discrete diffraction pattern for a 1D homogeneous array, top: $ u_n(z_{max}) $ ,<br>cross-section of bottom: evolution of $ u_n(z) $ for a single-site excitation<br>in the center . . . . .   | 22 |
| 3.1. Array scheme showing the constraint locations used to obtain the<br>energy surfaces below. . . . .   | 32 |
| 4.1. Two typical configurations for the SRR array. . . . .  | 37 |
| 4.2. Top: Capacitive defect embedded in SSR array, with couplings to<br>first-and second nearest neighbors. Bottom: (a)-(d) show the trans-<br>mission coefficient vs. wvector, for several parameter values: (a)<br>$\lambda = -0.1, \lambda' = (1/8)\lambda, \Delta = 0.7$ , (b) $\lambda = 0.4, \lambda' = 0.21, \Delta = -0.5$ , (c)<br>$\lambda = 0.4, \lambda' = 0.21, \Delta = 0.5$ , (d) $\lambda = 0.4, \lambda' = 0.21, \Delta = 1.0$ . . . . . | 40 |



- 4.3. (a) SRR array with external inductive defect. (b) Transmission coefficient vs wavevector, for different values of the relative coupling defect. The lines show the theoretical results, symbols the direct numerical integration:  $\lambda_1/\lambda = 1.25$ (circles), 1.5(squares), 1.75 (rhombi) and 2.0(stars). (c) Output profile after  $t = 1500$  as a function of wavevector and ring site, for  $\lambda_1/\lambda = 1$ . Impurity site is located at  $n = 0$ . 42
- 4.4. (a) External defect coupled symmetrically to the SSR array. Only couplings to first nearest neighbors are considered. (b) Transmission vs wavevector for several  $\lambda'/\lambda$  values: 0.5 (circles), 1.0 (rhombi) and 1.5 (triangles). (c) Output profile after  $t = 1500$  as a function of wavevector and ring site, for  $\lambda_1/\lambda = 1$ . . . . . 46
- 4.5. (a)  $P$  vs  $\lambda$  diagram for NLM. (b)  $\lambda$  vs  $U_0$  for NLM (black lines) and  $\omega_{cc}$  vs  $U_0$  for local modes (gray lines),  $\beta = 10$  and  $\epsilon = 5$ . . . . . 49
- 4.6. Transmission coefficient  $T$  as a function of beam angle  $k$  and amplitude  $U_0$ . Bright (dark) regions denote high (low)  $T$ . Dashed line marks places where  $\omega_k = \omega_{cc}$  and  $T = 0$ . . . . . 51
- 4.7. (a)  $t$  vs  $k$  for  $U_0 = 0.5$  (squares), 1.36 (diamonds), and 2 (circles). (Lines correspond to theoretical  $t$  and symbols to numerical simulations results.) (b) Linear output profile for different  $k$  and  $U_0 = 1.36$ . The dashed line marks the position of the impurity site. . . . . 52

- 5.1. (a) Sketch of the light propagation in a 1D waveguide array, when only one waveguide is excited. (b)-(d) Simulated intensity distribution in the lattice sites for ordered (b), single realization of on-site disorder degree  $W_c = 0.36$  (c) and  $W_c = 1$  (d) after propagation through the waveguide array when only the central waveguide is excited. (e) Simulated averaged PR  $R$  vs. on-site disorder for different levels of inter-site disorder after linear (low power) propagation. (f) Simulated averaged PR vs. Power  $P$  and onsite-disorder  $W_c$  after nonlinear propagation (black contour denotes  $R = R_0$ ). In all cases, the PR is normalized to  $R_0 \equiv R(W_c = 0)$ . . . . . 58
- 5.2. (a) Microscopic images of an ordered (top) and disordered (bottom) 1D array. (b) Experimental intensity output patterns. Upper row: ordered array; middle row: single realization disordered array; bottom row: averaged disordered output pattern. (c) Experimental PR  $R$  versus disorder strengths for different levels of input power. . . . . 62
- 5.3. (a) Microscope image of the fabricated ordered square lattice. (b) Corresponding averaged output intensity profile. (c) Numerical simulation of the PR for different mixed disorder:  $W_c = 0$  (black solid line),  $W_c = W_c/4$  (red dashed line),  $W_c = W_c/2$  (blue dotted line). (d) Experimental results for single-site (black solid line) and gaussian (red dashed line) input excitations, averaged over 25 realizations. All data is normalized to the ordered array  $R_0$ . . . . . 64

- 5.4. (a) Numerical output intensity pattern for an hexagonal lattice. (b) Numerical simulation of the PR for different mixed disorder:  $W_c = 0$  (black solid line),  $W_c = W_e/4$  (red dashed line),  $W_c = W_e/2$  (blue dotted line). The data is normalized to the ordered array  $R_0$ . . . . . 65
- 5.5. Scheme of a finite two-dimensional coupled array of elliptical waveguides with disordered boundary. . . . . 69
- 5.6. Comparison between simulations of the disordered boundary waveguide array of Eq.(5.2) (left column) with  $C_\alpha = 2$ ,  $C_\beta = 1.7$ ,  $\omega_\alpha = 11/28$ ,  $\omega_\beta = 4/17$ , averaged over 100 realizations and an ordered  $13 \times 5$  array (right column) . . . . . 71
- 5.7. Experimental results for the  $13 \times 5$  arrays: (a) Microscope image of one configuration of boundary-disordered, (b) ordered array, (c) mean output of 30 realizations of the boundary-disordered waveguide array,  $\lambda = 840 \text{ nm}$  (d) output of the ordered array, (e), (f) logarithmic plots of  $|u_{n,m_c}|$ ,  $|u_{n_c,m}|$ . . . . . 72
- 6.1.  $P$  versus  $\lambda$  for odd, even, and intermediate solutions in full, dashed, and thin lines, respectively. Inset: profiles corresponding to filled circles. 76
- 6.2. (a)  $g$  versus  $P$  for odd, even, and intermediate solutions in full, dashed, and thin lines, respectively. Inset:  $H$  versus  $P$ . (b)  $\Delta H_0$  (thick line) and  $\Delta H$  (thin line) versus  $P$ . (c) Energy surface where light (dark) color denotes a high (low)  $H$ -value. . . . . 79

- 6.3. (a) Output  $X_f$  versus input  $P$ . (b)-(d) Dynamical examples for  $P = 54, 300, \text{ and } 550$ , respectively.  $\gamma = 10, n_c = 26, k = 0.3, \alpha = 1/3, z_f = 50$ . . . . . 81
- 6.4. Examples of spatial profiles for (a) one-site (OO), (b) two-site horizontal (EO), (c) two-site vertical (OE), (d) four-site solutions (EE), (e) IS1, (f) IS2, (g) IS3-vertical, and (h) diagonal solutions, respectively, illustrated for an isotropic lattice. . . . . 83
- 6.5. Properties of fundamental stationary solutions for  $\gamma = 4$ : (a) Power versus frequency; (a)-inset:  $\Delta P/P$  versus  $\lambda$ ; (b)  $\Delta H$  versus power; (c) Stability versus power. Different solutions are plotted with different line-types: one-site (thick solid blue), two-site (thick dotted blue), four-site (thick dashed blue), IS1 (thin solid black), IS2 (thin dotted black), and IS3 (thin dashed black), respectively. . . . . 85
- 6.6. Energy surfaces for  $\gamma = 4$ , in the five different power regimes discussed in the text : (a)  $P = 5$ ; (b)  $P = 9.45$ ; (c)  $P = 10$ ; (d)  $P = 12$ ; (e)  $P = 35.5$ . The center of mass  $\{X, Y\}$  for the four stationary solutions are:  $\{8, 8\}$  (OO),  $\{8.5, 8\}$  (EO),  $\{8, 8.5\}$  (OE), and  $\{8.5, 8.5\}$  (EE). White dots denote local extrema corresponding to intermediate solutions. (System size  $N = M = 15$  and fixed boundary conditions were used.) . . . . . 88

6.7. Examples of mobility dynamics in the propagation direction  $z$ , corresponding to surfaces shown in Fig. 6.6(a), (c), (d), and (e), respectively. In each subfigure, top figures show profiles movement [(a) shows a colormap, where colors were normalized to the maximum amplitude of each plot; this colormap also applies to (b)-(d)], and bottom figures center of mass evolution for  $X$  (full line) and  $Y$  (dashed line). (a)  $P = 5$ ,  $k_x = k_y = 0.038$ ; (b)  $P = 10$ ,  $-k_x = k_y = 0.018$ ; (c)  $P = 12$ ,  $k_x = k_y = 0.015$ ; (d)  $P = 35.5$ ,  $k_x = 0.015$  and  $k_y = 0$ . (Other parameter values are the same as in Fig. 6.6.) . . . . . 92

7.1.  $P$  vs.  $\lambda$  continuation of linear vortices in the saturable case,  $\gamma = 10$ . For  $S = 1$ , two possible continuations were found (black and blue),  $S = 2$  is shown with a green line. The stable (unstable) regimes are plotted with full (dashed) lines, insets show amplitude and phase examples corresponding to the dots. . . . . 99

7.2. Scheme of a  $c = 1$  vortex structure . . . . . 101

7.3.  $P$  vs.  $\lambda$ , (a)  $c = 0$  for  $S = 1(2)$  shown with thin (thick) lines. (b) for  $c = 1$ ,  $S = 1(2, 3)$  shown in thin (thick, gray), and (c)  $c = 2$ ,  $S = 1(2, 3)$  showed in thin (thick, gray), The stable (unstable) regimes are plotted with full (dashed) lines, insets show amplitude and phase examples corresponding to the dots. . . . . 105

7.4. (a)  $P$  vs.  $\lambda$ ,  $c = 4$  for two different families:  $S = 2$  is shown with a thick black line, where dashed parts denote the instability, while all other families are completely unstable.  $S = 3$  is plotted with a dotted (dotdashed) line. Amplitude and phase examples correspond to the dots. (b)  $P$  vs.  $\lambda$ , for  $S = 1$  and  $c \geq 4$ , (c) profiles and phases, from (1)-(7) corresponding to the empty circle, empty square, star, filled square, circle, diamond and triangle, respectively . . . . . 106

C.1. Sketch of the fs-laser writing process . . . . . 132

## RESUMEN

En esta Tesis llevamos a cabo la exploración teórica y experimental de varios problemas en óptica no lineal y otros campos relacionados, los cuales caen en la categoría general de localización no lineal en estructuras discretas. En particular, nos enfocamos en la creación y propagación de solitones ópticos discretos en arreglos de guías de onda no lineales acopladas.

Los problemas abordados en esta Tesis incluyen:

- i) Resonancias de Fano en el contexto de metamateriales magnéticos.
- ii) Resonancia de Fano en arreglos de guía con no linealidad saturable.
- iii) Efecto del desorden sobre la propagación de un pulso inicialmente localizado en una red finita.
- iv) Problema de Anderson donde el desorden solo actúa en los bordes del sistema.
- v) Movilidad de solitones discretos en 1D y 2D para una red con no linealidad saturable.
- vi) Vórtices discretos en redes con no linealidad saturable.

## ABSTRACT

In this thesis, we explore theoretically and experimentally different problems of nonlinear optics and related fields, which are in the general class of nonlinear localization in discrete structures. In particular, we focus on the creation and propagation of discrete optical solitons in nonlinear coupled waveguide arrays.

The problems tackled in this thesis include:

- i) Fano resonances in the context of magnetic metamaterials.
- ii) Fano resonance in waveguide arrays with saturable nonlinearity.
- iii) Effect of disorder on the propagation of an initially localized pulse in a finite array.
- iv) Anderson problem in a system with disordered boundaries.
- v) Mobility of discrete solitons in one- and two-dimensional saturable nonlinear arrays.
- vi) Discrete vortices in waveguide arrays with saturable nonlinearity.



# 1. Introduction

Different physical systems can show surprising parallels when some spatial parameter is periodically modulated. Periodic potentials possess a discrete translational symmetry breaking up the linear wave spectrum, causing electrons in crystalline structures to be assembled in energy bands and (forbidden) gaps in between them. Light propagation in photonic crystals is limited to certain frequencies, whereas others are totally reflected. Similar properties are found for matter waves of Bose-Einstein condensates in optical lattices, spin waves in ferromagnets, phonons in crystals or electromagnetic waves in metamaterials. All these examples lead to band structures containing extended Bloch modes and gaps, where extended states are prohibited. These gaps are therefore a perfect place in the search of localized modes [1]-[4].

When one or few “impurities” are placed in an otherwise perfect periodic potential, the translational invariance is broken and the possibility of so called Fano resonances [5] emerges. This sharp, anti-symmetric resonances are characterized by the total reflection of plane waves with determined wave vectors in the impurity region. The wave propagation in the presence of a periodic and a scattering potential is characterized by a band-structure (of propagating waves) and a discrete frequency belonging

to a localized state. Total reflection occurs, when the discrete state is in resonance with the (continuous) band spectrum. Linear Fano resonances have been reported in a large number of systems (e.g. [5]-[18]), since the interaction of plane waves with discrete defect modes is ubiquitous in almost any physical system. We study the onset of linear Fano resonances in split-ring resonator arrays, which constitute a simple but useful model for magnetic metamaterials. Scattering of plane waves is not restricted to be caused by linear impurities, it is also observed in nonlinear waveguide arrays: Nonlinearity can generate several scattering channels leading to resonances due to destructive interference and, as a consequence, to total absence of transmission similar to the original Fano problem [19]-[23]. In a one dimensional (1D) waveguide-array with an embedded saturable nonlinear impurity we also observed a nonlinear Fano resonance.

Adding not only a few impurities, but disorder to the whole periodic system leads to the destruction of periodicity, the breaking up of the band structure and to the onset of a complete localization of the eigenmodes in 1D and 2D, known as Anderson localization [24]-[26]. Therefore, in infinite, not correlated 1D and 2D lattices, already the smallest amount of disorder causes exponentially localized modes and the absence of wave propagation. As disorder-induced localization is based on interference, it is a universal concept applicable to a variety of physical systems [27], such as the transport of acoustic waves [28], microwaves [29], spin [30] and matter waves [31]. Recent studies of the asymptotic behavior of wave packet spreading suggest, that the addition of nonlinearity to the system leads to the breakdown of complete

localization, but they take extremely long evolution scales and very large lattices [32], thus being very far from the regime of possible experimental observation. To focus on realistic systems, we concentrate our attention to lattices with a finite length and explore generic properties of nonlinear disordered lattice systems in the first stages of their evolution. We present theoretical and experimental evidence that the presence of weak disorder promotes a more uniform spreading and distribution of a wave packet; an effect that is further enhanced by the presence of a focusing nonlinearity. For the case where the disorder is not in the bulk of the system, but it affects only the boundary of the array, it was predicted [33] that an excitation initially located inside the bulk of the system would nevertheless undergo Anderson localization as well. We confirmed this experimentally by launching a light beam at the center of a rectangular waveguide array, whose boundary is disordered, and observing beam localization, after some evolution distance.

Localized modes can not only be caused by defects or disorder - discrete nonlinear systems are known to support self-localized modes that exist due to the balance between discrete diffraction and the nonlinearity of the medium. Such spatially localized modes of discrete lattices, which exist in the absence of defects, are known as discrete solitons or intrinsic localized modes. They have been predicted in the studies of the Bose-Einstein condensates, in optical lattices and photonic-crystal waveguides and circuits [2, 34, 35]. In nonlinear optics, discrete optical solitons were first theoretically predicted by Christodoulides and Joseph [36], and later observed in experiments in 1D [37] and in 2D [38] in nonlinear optical waveguide arrays [3], which

provide ample possibilities for controlling and changing for example the geometry, dimensionality and nonlinearity of the system. In contrast to the soliton solutions of the *continuous* and homogeneous nonlinear Schrödinger equation, which are mobile by definition, nonlinear localized stationary modes of discrete Schrödinger lattices are in general immobile. Discreteness and nonlinearity impose an energy barrier, known as Peierls-Nabarro (PN) potential [39], that any mode has to overcome in order to move from one lattice site to the next one. The PN potential barrier is usually defined as the difference in energy (Hamiltonian) at constant Power between the fundamental localized stationary modes. A particularly interesting property of the saturable DNLS model [40]-[46] is the existence of certain points, where this energy difference vanishes, leading to the claim, that spatial solitons may travel in the lattice without radiation.

We show that, in one and two dimensions and close to the points of vanishing energy difference, there are regions of stability exchange between the fundamental modes, associated in general with the appearance of a family of intermediate, asymmetric stationary solutions [47], connecting the types of symmetric solutions at the bifurcation points [48]. The *effective* energy barriers that depend on these intermediate solutions are be constructed using a constraint method and we show possible mobility directions.

In homogeneous media, phase singularities lead to the formation of optical vortices [49], but phase singularities can also be found in periodic media and discrete systems. Discrete optical vortices were first theoretically studied in discrete lat-

tices [50, 51] and in continuous models with an external potential [52, 53]. Experimentally they were found independently by two groups [54, 55]. Since then, a lot more work has been dedicated to analyze different vortex mode families and their stability in the discrete nonlinear Schrödinger model [56, 57]. Discrete vortices may come in many configurations. In general, they are characterized by their topological charge, which counts the number of  $2\pi$  phase turns along a closed contour around the phase singularity, but additional phase singularities [58] can lead to multi-charged vortex modes [59]. In contrast to square lattices, different lattice geometries can allow stability also for higher topological charges [60] or stable combinations of dipole vortices [61]. In the case of defocusing nonlinearity, higher-order modes were also found to be stable [62, 63]. We explore the families of vortices appearing in focusing photorefractive discrete Schrödinger lattices. We show, how they are connected to the linear bands and which kinds of discrete vortices of higher charges can be stable.

This thesis is organized as follows. In the introductory chapter we present the theory leading to the Discrete Non Linear Schrödinger equation including a presentation of the nonlinearities used in this thesis (Chapter. 2). Some linear properties of this equation sets are discussed in Sec. 2.3, followed by properties of nonlinear stationary solutions in Sec. 2.4.

In Chapter 3 we introduce some numerical methods, which were used and improved in the present thesis, like the stability analysis presented for general *complex* stationary solutions (Sec. 3.1) as well as a constraint method used to construct pseudo-potential

energy landscapes to explore the possibility of soliton mobility in Sec. 3.2.

Chapter 4 addresses the problem of Fano resonances, with a focus on linear properties in the context of magnetic metamaterials in Sec. 4.1, whereas a nonlinear Fano problem for saturable waveguide arrays is discussed in Sec 4.2.

The following Chapter 5 is dedicated to disorder. First, we present a brief introduction to the concept of Anderson localization (Sec 5.1), followed by a discussion of the effect of disorder on the spreading of a wavepacket in finite nonlinear arrays (Sec. 5.2). Finally, we study experimentally the influence of a disordered boundary on localization in a linear ordered array of optical waveguides (Sec. 5.3).

The mobility of nonlinear localized solutions is discussed in Chapter 6, for 1D (Sec. 6.1) and 2D lattices 6.2.

Discrete vortices, complex localized solutions with a phase singularity, are studied in Chapter 7 in the context of saturable nonlinear waveguide arrays.

Chapter 8 concludes this thesis and gives an outlook on possible future projects.

## 2. The discrete nonlinear Schrödinger equation

This derivation employs a Coupled-Mode-Theory approach for nonlinear waveguide arrays and essentially follow the line of derivation obtained in the PhD thesis of R.A. Vicencio [64].

In a source-free space the wave equation for the electric field  $\vec{E}$  is obtained from the Maxwell-equations,

$$\nabla^2 \vec{E}(\vec{r}, t) = \frac{1}{c^2} \frac{\partial^2 \vec{E}}{\partial t^2}. \quad (2.1)$$

Assuming that propagation of waves is confined to a propagation direction  $\hat{z}$  it is possible to completely decompose the fields, so the eigenmodes of (2.1) are of the form

$$\vec{E}(\vec{r}, t) = \frac{1}{2} \sum_j \vec{f}_j(x, y) a e^{i(k_j z - \omega_j t)} + cc. \quad (2.2)$$

with propagation constants  $k_j$ , frequencies  $\omega_j$  and amplitude  $a$ . In presence of polarization (source), the wave equation becomes

$$\nabla^2 \vec{E}(\vec{r}, t) = \frac{1}{c^2} \frac{\partial^2 \vec{E}}{\partial t^2} + \frac{1}{c^2 \epsilon_0} \frac{\partial^2 \vec{P}}{\partial t^2}. \quad (2.3)$$

The Ansatz for its Eigenmodes is inspired in (2.2) with an additional slowly varying envelope function  $a(z)$  of the amplitude in  $\hat{z}$ :

$$\vec{E}(\vec{r}, t) = \frac{1}{2} \sum_j \vec{f}_j(x, y) a(z) e^{i(k_j z - \omega_j t)} + cc. \quad (2.4)$$

Coupled waveguides are ideal to be modeled in a discrete scheme. The essential idea here is to assume that the linear interaction between the waveguides is weak, so there will be only nearest-neighbor coupling. This means, that only the tails of the modes interact. The nonlinear interaction is assumed to be local, hence there is no nonlinear coupling between neighboring waveguides<sup>1</sup>. For simplicity of notation the discrete part of the derivation considers only one waveguide interacting with one neighbor. Interaction with a second one could be implemented easily in principle, since it is implemented in the linear part of the equations. The same happens for higher dimensions or different geometries, since there are just more neighbors to assume in the linear interaction part. The indices of the field  $\vec{E}_\mu^\nu(\vec{r}, t)$  denote the waveguide  $\nu = \{1, 2\}$  under the influence of the field in waveguide  $\mu = \{1, 2\}$ . Note that the field  $\vec{E}_\mu^\nu(\vec{r}, t)$  still depends on the position  $\vec{r}$ , since we still are in a "semi-continuous" system, until now we only introduced a separation into two waveguides with modes defined in the entire space  $\vec{r}$ . Inserting the Ansatz of separable modes (2.4)

$$\vec{E}_\mu^\nu(\vec{r}, t) = \frac{1}{2} \sum_j \vec{f}_{\mu j}^\nu(x, y) a_{\mu j}^\nu(z) e^{i(k_j z - \omega_j t)} + cc.$$

into equation (2.3), we get

---

<sup>1</sup>It is also possible to study nonlinear nonlocal media like nematic liquid crystals [65], plasmas [66], or nonlocal photorefractive materials [67] as well as waveguides embedded in a Kerr-media with non-evanescent coupling leading to nonlinear interaction terms [68]



$$\begin{aligned}
\frac{1}{c^2 \epsilon_0} \frac{\partial^2 \vec{P}_\mu^\nu}{\partial t^2} &= \left( \overbrace{\frac{\partial^2}{\partial x^2} + \frac{\partial^2}{\partial y^2} + \frac{\partial^2}{\partial z^2} - \frac{1}{c^2} \frac{\partial^2}{\partial t^2}}^{=: \Delta_\perp} \right) \left[ \frac{1}{2} \sum_j \vec{f}_{\nu j}^\nu(x, y) a_{\nu j}^\nu(z) e^{i(k_j z - \omega_j t)} + cc. \right] \\
&= \frac{1}{2} \sum_j \left[ \left\{ a_{\nu j}^\nu(z) \overbrace{\left( \Delta_\perp - k_j^2 + \frac{\omega_j^2}{c^2} \right)}^{\equiv 0 \text{ for (2.1) and (2.2)}} \vec{f}_{\nu j}^\nu(x, y) + \right. \right. \\
&\quad \left. \left. \vec{f}_{\nu j}^\nu(x, y) \left( \frac{\partial^2 a_{\nu j}^\nu(z)}{\partial z^2} + 2ik_j \frac{\partial a_{\nu j}^\nu(z)}{\partial z} \right) \right\} e^{i(k_j z - \omega_j t)} + cc. \right] \\
&\simeq \sum_j \left[ ik_j \vec{f}_{\nu j}^\nu(x, y) \frac{\partial a_{\nu j}^\nu(z)}{\partial z} e^{i(k_j z - \omega_j t)} + cc. \right].
\end{aligned} \tag{2.5}$$

The last approximation is possible for slowly varying modes in  $\hat{z}$ , thus  $\frac{\partial^2 a_{\nu j}^\nu(z)}{\partial z^2} \ll k_j \left| \frac{\partial a_{\nu j}^\nu(z)}{\partial z} \right|$ .

In the second line we used the relation (2.1), the wave equation for the sourceless case, with its eigenmodes  $\vec{f}_{\nu j}^\nu(x, y)$ .

To treat the left-hand side of equation (2.5), one splits the polarization into a linear part depending on *all* other modes and a nonlinear, but *local* part,

$$\vec{P}_\mu^\nu(\vec{r}, t) = \vec{P}_\mu^{\nu, lin}(\vec{r}, t) + \vec{P}_\mu^{\nu, nl}(\vec{r}, t) = \sum_j [\vec{P}_{\mu, j}^{\nu, lin}(\vec{r}, t) + \vec{P}_j^{\nu, nl}(\vec{r}, t)].$$

The linear polarization inside the waveguide  $\nu$  for the mode  $j$  can be expressed as

$$\vec{P}_\mu^{\nu, lin}(\vec{r}, t) = \epsilon_0 \chi_j^{(1), \nu} \cdot \vec{E}_{\mu j}^\nu(\vec{r}, t) = \frac{1}{2} \epsilon_0 \chi_j^{(1), \nu} [(f_{1j}^\nu(x, y) a_{1j}^\nu(z) + f_{2j}^\nu(x, y) a_{2j}^\nu(z)) e^{i(k_j z - \omega_j t)} + c.c.].$$

If we insert it into eq. (2.5), do the temporal derivative for the linear part and reorder, we obtain for the mode  $j$  in waveguide  $\nu$

$$\begin{aligned} \frac{1}{c^2 \epsilon_0} \frac{\partial^2}{\partial t^2} P_j^{\nu, nl}(\vec{r}, t) = & \left\{ ik_j \vec{f}_{\nu j}^{\nu}(x, y) \frac{\partial a_{\nu j}^{\nu}(z)}{\partial z} + \right. \\ & \left. + \chi_j^{(1), \nu} \frac{\omega_j^2}{2c^2} [(\vec{f}_{1j}^{\nu}(x, y) a_{1j}^{\nu}(z) + \vec{f}_{2j}^{\nu}(x, y) a_{2j}^{\nu}(z))] \right\} e^{i(k_j z - \omega_j t)} + cc. \end{aligned} \quad (2.6)$$

### 2.1. The Kerr nonlinearity

In centrosymmetric media the polarization has to fulfill the inversion symmetry, so all terms depending on even powers of the field vanish, thus  $\chi^{(2)} = 0$ . Therefore, the first nonlinear correction term in the Taylor expansion which has to be considered is  $\chi^{(3)}$ . Although all materials exhibit a non-vanishing  $\chi^{(3)}$  response, only some are nearly loss-less. The most common examples are AlGaAs and fused silica glasses, which show a good ratio between nonlinearity and losses [3]. The linear dependency of the refractive index on the intensity is called Kerr effect. Without loss of generality, we consider only one mode, i.e.  $\omega_j \rightarrow \omega$  and  $k_j \rightarrow k$  and remember, that the nonlinear response is local and effectively instantaneous<sup>2</sup>. The nonlinear polarization can thus be expressed as

<sup>2</sup>The timescale  $\tau_f$  of the fluctuations of the beam has to be bigger than the response timescale  $\tau_r$ . This is especially important, when pulsed beams are used to observe a nonlinear response, thus  $\tau_r$  has to be in the order of  $10^{-15}$  sec for a nonlinear excitation with an fs-laser.

$$\begin{aligned}
P_j^{\vec{\nu},nl}(\vec{r}, t) &= \epsilon_0 \chi^{(3),\nu} |\vec{E}_\nu^{\vec{\nu}}(\vec{r}, t)| \vec{E}_\nu^{\vec{\nu}}(\vec{r}, t) \\
&= \frac{\epsilon_0}{8} \left[ 3\chi_\omega^{(3),\nu} |\vec{f}_\nu^{\vec{\nu}}|^2 |a_\nu^\nu|^2 \vec{f}_\nu^{\vec{\nu}} a_\nu^\nu e^{i(kz-\omega t)} + \chi_{3\omega}^{(3),\nu} (\vec{f}_\nu^{\vec{\nu}})^3 (a_\nu^\nu)^3 e^{i(kz-3\omega t)} + c.c. \right].
\end{aligned} \tag{2.7}$$

The generation of higher harmonics (for example  $3\omega$ ) is negligible not only because of the lower factor of production of  $1/3$ , but also because for the large phase mismatch[3]. Therefore we only keep the so called *self-focusing* or *self-phase modulation* term with  $\omega$ . Inserting (2.7) in (2.6), after the time derivative we end up with

$$\begin{aligned}
& -\frac{3\omega^2}{8c^2} \chi_\omega^{(3),\nu} |\vec{f}_\nu^{\vec{\nu}}|^2 |a_\nu^\nu|^2 \vec{f}_\nu^{\vec{\nu}} a_\nu^\nu e^{i(kz-\omega t)} + c.c. = \\
& = \left\{ ik \vec{f}_\nu^{\vec{\nu}}(x, y) \frac{\partial a_\nu^\nu(z)}{\partial z} + \chi^{(1),\nu} \frac{\omega^2}{2c^2} (\vec{f}_1^{\vec{\nu}}(x, y) a_1^\nu(z) + \vec{f}_2^{\vec{\nu}}(x, y) a_2^\nu(z)) \right\} e^{i(kz-\omega t)} + c.c.
\end{aligned} \tag{2.8}$$

Since (2.8) has to be true separately for the term of  $e^{i(kz-\omega t)}$  and its complex conjugate, we finally obtain

$$-\frac{3\omega^2}{8c^2} \chi_\omega^{(3),\nu} |\vec{f}_\nu^{\vec{\nu}}|^2 \vec{f}_\nu^{\vec{\nu}} |a_\nu^\nu|^2 a_\nu^\nu = ik \vec{f}_\nu^{\vec{\nu}} \frac{\partial a_\nu^\nu(z)}{\partial z} + \chi^{(1),\nu} \frac{\omega}{2c^2} (\vec{f}_1^{\vec{\nu}} a_1^\nu(z) + \vec{f}_2^{\vec{\nu}} a_2^\nu(z)). \tag{2.9}$$

If we now assume identical waveguides, all the transverse fields have the same form, since all waveguides have the same mode profile. To eliminate the transversal dependency, we multiply (2.9) with the complex conjugate  $\vec{f}_\nu^{\vec{\nu}*}$  and integrate over

$\int_{-a/2}^{a/2} dx \int_{-\infty}^{\infty} dy$ , since we have an 1D setting with periodicity  $a$  in the direction  $\hat{x}$ . We define the propagation constant

$$\beta \equiv \frac{\omega^2}{2kc^2} \chi^{(1),\nu}(\omega) = \frac{\omega}{2cn} \chi^{(1),\nu}(\omega). \quad (2.10)$$

The coupling coefficient is given by

$$C_\mu \equiv \beta \frac{\int_{-a/2}^{a/2} \int_{-\infty}^{\infty} \vec{f}_\mu \vec{f}_\nu^* dx dy}{\int_{-a/2}^{a/2} \int_{-\infty}^{\infty} |\vec{f}_\nu|^2 dx dy} \quad (2.11)$$

and the nonlinear coefficient by

$$\gamma \equiv \frac{3k\omega^2}{8c^2} \chi_\omega^{(3),\nu} \frac{\int_{-a/2}^{a/2} \int_{-\infty}^{\infty} |\vec{f}_\nu|^4 dx dy}{\int_{-a/2}^{a/2} \int_{-\infty}^{\infty} |\vec{f}_\nu|^2 dx dy}. \quad (2.12)$$

Now we can drop one of the indices and rewrite the equation (2.9) for a dimer as

$$-i \frac{da_1(z)}{dz} = \beta a_1(z) + C_2 a_2(z) + \gamma |a_1(z)|^2 a_1(z) \quad (2.13)$$

$$-i \frac{da_2(z)}{dz} = \beta a_2(z) + C_1 a_1(z) + \gamma |a_2(z)|^2 a_2(z).$$

The extension to the case of  $N$  coupled waveguides is straightforward and can be found in [64]. Therefore, we can write down the DNLS of the light amplitude  $a_n$  at a site  $n$ ,

$$-i \frac{da_n(z)}{dz} = \beta a_n(z) + C_n a_n(z) + C_{n+1} a_{n+1}(z) + \gamma |a_n(z)|^2 a_n(z). \quad (2.14)$$

When the waveguides furthermore are ordered equidistantly,  $C_n = C_{n+1}$ . By means of the transformations  $u_n = a_n \exp(-i\beta z)$ ,  $\tilde{C} = C/\gamma$ ,  $\xi = \gamma z$  and renaming  $C = \tilde{C}$ ,  $z = \xi$  we obtain the dimensionless DNLS:

$$-i \frac{du_n(z)}{dz} = C_n u_n(z) + C_{n+1} u_{n+1}(z) + |u_n(z)|^2 u_n(z). \quad (2.15)$$

## 2.2. The saturable nonlinearity

Photorefractive materials respond to an external bias electric field by altering their refractive index. For example, applying different beams, interference patterns can be used to create bright and dark regions and therefore induce an optic waveguide array, see e.g. [69] for an review. In regions of high intensity, electrons are excited into the conduction band, redistribute and get trapped in the darker regions creating a space-charge-field which acts as an effective screen to the external field modifying the refraction index through the electro-optic Pockels effect. The corresponding model is the Vinetskii-Kukhtarev model[71]. The basic equations[70, 71] which describe the photorefractive effect are the following:

The rate equation for the ionized donor density  $N_D^+$  out of a total of  $N_D$  is given by

$$\frac{\partial N_D^+}{\partial t} = \hat{s}(I + I_d)(N_D - N_D^+) - \gamma_r N_e N_D^+. \quad (2.16)$$

Here  $\hat{s}$  represents the photoionization cross section which is related to the absorption cross section.  $I$  is the intensity of the external, imposed beam, whereas  $I_d$  is the so called dark radiance, which accounts for the thermally generated electrons. The

carrier recombination constant is denoted by  $\gamma_r$  and  $N_e$  is the density of electrons in the conduction band. The continuity equation gives

$$\frac{\partial}{\partial t}(N_D^+ - N_e) + \frac{1}{e}\nabla \cdot \vec{J} = 0, \quad (2.17)$$

with  $e$  being the absolute value of the electron charge. The current density is composed by a diffusion and a drift component,

$$\vec{J} = eN_e\mu\vec{E} + k_B T\mu\nabla N_e, \quad (2.18)$$

where  $\mu$  is the so called electron mobility and  $k_B T$  is, as usual, the thermal energy. The total electric field is given by the sum of the external bias field and the field generated by the charges, applying Gauss law one obtains:

$$\nabla \cdot (\epsilon\vec{E}) = e(N_D^+ - N_e - N_A), \quad (2.19)$$

with  $\epsilon$  being the materials permittivity. It is of importance to note, that  $N_D \gg N_A \gg N_e$ , which reduces [73] under steady state conditions, where all temporal derivatives vanish, to

$$N_D^+ = N_A \left( 1 + \frac{\epsilon}{eN_A} \frac{\partial E}{\partial x} \right); \quad (2.20)$$

$$N_e = \frac{\hat{s}(N_D - N_A)}{\gamma_r N_A} (I + I_d) \left( 1 + \frac{\epsilon}{eN_A} \frac{\partial E}{\partial x} \right)^{-1}. \quad (2.21)$$

To simplify the notation, we assumed, that the space charge field has only one component parallel to  $\hat{x}$ . Assuming an imposed beam of finite dimension (thus

having a width smaller than the crystals extension), we denote the asymptotic limits of  $I_{\pm\infty} = I(x \rightarrow \pm\infty)$  and  $E_0 = E(x \rightarrow \infty)$  and determine the free electron density not effected by the external bias field by

$$N_{e0} = \frac{\hat{s}(N_D - N_A)}{\gamma_r N_A} (I_\infty + I_d). \quad (2.22)$$

Taking into account, that  $J$  is constant (steady state of eq. (2.17)), we obtain

$$N_{e0} E_0 = e N_e \mu E + k_b T \mu \frac{\partial N_e}{\partial x}$$

or

$$E = \frac{N_{e0} E_0}{N_e e \mu} - \frac{k_b T}{N_e e} \frac{\partial N_e}{\partial x}. \quad (2.23)$$

Combining eqs. (2.21) and (2.23), we finally obtain

$$E = E_0 \frac{I_\infty + I_d}{I + I_d} \left( 1 + \frac{\epsilon}{e N_A} \frac{\partial E}{\partial x} \right) - \frac{k_b T}{e} \frac{(\partial I / \partial x)}{(I + I_d)} \quad (2.24)$$

$$+ \frac{k_b T \epsilon}{e^2 N_A} \left( 1 + \frac{\epsilon}{e N_A} \frac{\partial E}{\partial x} \right)^{-1} \frac{\partial^2 E}{\partial^2 x}.$$

When a strong bias field is applied, the thermal terms are negligible, assuming furthermore a broad beam,  $|\partial E / \partial x| \ll 1$ , but still smaller than the crystal width. So, in a first, isotropic approximation [73, 74], the space-charge-field, which we now call  $E_{sc}$ , is given by

$$E_{sc} = E_0 \frac{I_\infty + I_d}{I + I_d}, \quad (2.25)$$

which represents the local, isotropic, instantaneous and nonlinear response of the crystal to the external bias field.

To determine the discrete equation set, we now present a different approach, taking into account already in the beginning the response of the material to the external field. Furthermore we consider, that some crystals as the commonly used SBN (Strontium Barium Niobate) are birefringent and restrain the treatment to the extraordinary polarization, which shows a stronger nonlinearity [72]. We start from the Helmholtz-equation

$$\nabla^2 \vec{E}(\vec{r}, t) + (k_0 n'_e)^2 \vec{E} = 0, \quad (2.26)$$

with  $k_0 = 2\pi/\lambda$  for the free-space wavelength  $\lambda$  and the propagation direction  $\hat{z}$ .

We assume, that the optical axis of the crystal, the polarization of the beam and the external bias field are oriented along the  $\hat{x}$ -direction. These conditions lead to the nonlinearly perturbed extra-ordinary refractive index  $(n'_e)^2 = n_e^2 - n_e^4 r_{33} E_{sc}$  [73]. Here  $n_e$  is the unperturbed extra-ordinary refractive index and  $r_{33}$  is the electro-optic coefficient, for the chosen parallel setting of polarization, crystal axis and external field we do not need to consider the full Pockels tensor  $\hat{r}$ . With the Ansatz of slowly varying envelope in  $\hat{z}$ :  $E = \hat{x}\phi(x, z) \exp(ikz)$  in eq. (2.26), we obtain the corresponding paraxial approximation [73]:

$$i \frac{\partial \phi}{\partial z} + \frac{1}{2k} \frac{\partial^2 \phi}{\partial x^2} = \frac{k_0}{2} (n_e^3 r_{33} E_{sc}) \phi. \quad (2.27)$$

Now we can insert eq. (2.25) into eq. (2.27) and normalize:  $z = kx_0^2 \xi$ ,  $x = sx_0$  with an arbitrary spatial width  $x_0$  and a new adimensional amplitude  $U = \phi \sqrt{\frac{n_e \mu_0^{1/2}}{2I_d \epsilon_0^{1/2}}}$ .



Furthermore, we use, that  $I = (n_e/2)\sqrt{\epsilon_o/\mu_o}|\phi|^2$ , define the nonlinear strenght  $\gamma = (k_0x_0)^2n_e^4r_{33}E_0/2(1 + I_\infty/I_d)$  and finally rename  $\xi \rightarrow z$  and  $s \rightarrow x$ , thus we obtain the saturable NLS

$$-i\frac{\partial U(z)}{\partial z} = \frac{\partial^2 U(z)}{\partial x^2} - \gamma \frac{U(z)}{1 + |U(z)|^2}. \quad (2.28)$$

We discretize the lattice following  $a_n = U(nd)$  with an adimensional lattice spacing  $d$ . The discrete second derivative is given by  $\frac{\partial^2 U(z)}{\partial x^2} \simeq a_{n+1} + a_{n-1} - 2a_n$  and furthermore we substitute  $u_n = a_n \exp(2iz)$ . Finally, the corresponding discrete lattice equation in 1D, the DNLS equation with saturable nonlinearity (s-DNLS), is given by

$$-i\frac{du_n}{dz} = u_{n+1}(z) + u_{n-1}(z) - \gamma \frac{u_n(z)}{1 + |u_n(z)|^2}. \quad (2.29)$$

The waveguide structure is optically induced in photorefractive crystals like SBN (Strontium Barium Niobate), Barium Titanate or Lithium Niobate. Currently there are two different ways to experimentally achieve lattice structures: One is using interfering laser beams to produce interference patterns constructing the lattice(e.g. [75, 76, 38]), the other one uses patterns produced by spatial light modulators (e.g. [77]-[81]) for the same purpose. In any case, the induced lattice structure has to be polarized perpendicular to the probe beam to avoid interference between the lattice and the probe beam.

### 2.3. Linear properties and discrete diffraction

To be able to consider nonlinear behavior of a system, the first step should be to study the linear limit. Periodic or discrete media show linear properties, which can not be

observed in homogeneous media, like linear localized modes at defects [82], photonic Bloch oscillations [83]-[86], Zener tunneling [87, 88] and dynamical localization [89]. The linear limit of the cubic DNLS [eq. (2.15)] equation is given for a 1D array by

$$i \frac{d}{dz} u_n(z) + C [u_{n+1}(z) + u_{n-1}(z)] = 0. \quad (2.30)$$

We look for extended solutions inserting a stationary plane wave Ansatz

$$u_n(z) = u_0 \exp [i(n\kappa + \lambda z)],$$

obtaining the dispersion relation

$$\lambda(\kappa) = 2C \cos(\kappa).$$

Here  $\kappa$  corresponds to the period of the Bloch vector and represents the phase differences between adjacent sites,  $\lambda$  is the propagation constant or spatial frequency. Using the periodicity of  $\lambda$  we can restrict to  $-\pi \leq \kappa \leq \pi$ , which leads to a band structure for cubic lattices within the interval  $\lambda \in [-2C, 2C]$ . Linear modes are restricted to exist inside this band.

In 1D s-DNLS lattices [eq. (2.29)] small-amplitude plane waves, correspond to the band  $\lambda \in [-2 - \gamma, 2 - \gamma]$ . In the high-amplitude limit, the saturable nature of our system allows to completely neglect the nonlinearity and implies a second band  $\lambda \in [-2, 2]$ . So the superior bound of  $\lambda = 2$  of this high-amplitude linear band corresponds as well to the upper limit of existence of unstaggered localized modes. Therefore 1D fundamental stationary localized solutions are limited to the region  $\lambda \in [2 - \gamma, 2]$ , with size  $\gamma$ .

Our discrete model possesses extended solutions in form of Bloch waves. Their propagation constant or (spatial) frequency  $\lambda$  in the cubic case is limited to one

band with two semi-infinite gaps, what clearly shows the limitations of the discrete model. The complete band-structure can be numerically obtained solving the full wave equation taking into account the periodic distribution of the refractive index [3]. Although the DNLS is only valid for materials with a large first band-gap, experiments have shown good agreement with the discrete theory [3]. Limitations of the model are discussed in Ref. [92].

The superposition of normal modes [3] is a solution to eq. (2.30)

$$u_n(z) = \int_{-\pi}^{\pi} d\kappa \tilde{u}(\kappa) \exp(in\kappa) \exp[i\lambda(\kappa)z], \quad (2.31)$$

with Fourier components

$$\tilde{u}(\kappa) = \frac{1}{2\pi} \sum_n u_n|_{z=0} \exp(-in\kappa).$$

The mode evolution is governed by the dispersion relation  $\lambda(\kappa)$ . Typical input beams cover only few guides, so the Fourier spectrum is finite with a central  $\kappa_0$  determined by the input angle. This can be used for effective diffraction management [90]. If the input is furthermore a single-site excitation ( $\delta$ -function), the corresponding Fourier coefficient is a constant  $\tilde{u}(\kappa) = u_0/2\pi$  and the integral 2.31 can be solved:

$$u_n(z) = i^n J_n(2Cz) u_0,$$

where  $J_n(z)$  is the  $n$ -th order Bessel function of the first kind. The extension to a 2D ordered array for a single site-excitation simply leads to the superposition of two solutions [3, 93]:

$$u_{n,m}(z) = i^{n+m} J_n(2Cz) J_m(2Cz) a_0.$$

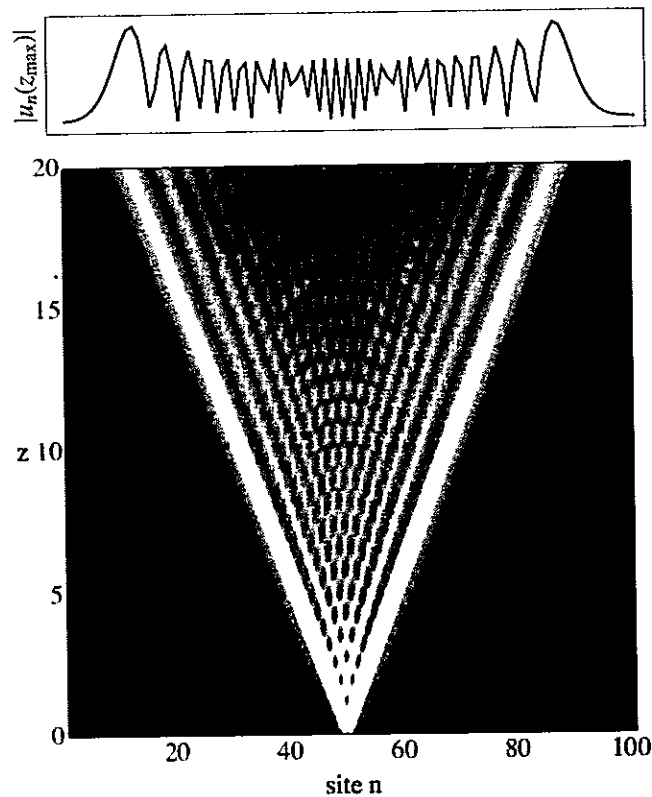


Figure 2.1.: Discrete diffraction pattern for a 1D homogeneous array, top:  $|u_n(z_{\max})|$ , cross-section of bottom: evolution of  $|u_n(z)|$  for a single-site excitation in the center

A plot (Fig. 2.1) of the numerical solution in 1D of Eq. (2.30) shows the characteristics of discrete diffraction in an homogeneous array, which is very different to diffraction in a continuous medium. Instead of diffractive broadening with the maximum of the distribution remaining in the excited site, the *discrete* diffraction pattern of a central single-site excitation exhibits distinct side lobes and small amplitudes around the initially excited site [91], which leads to new behavior when disorder and nonlinearity are considered as well, as discussed in section 5.2.

## 2.4. Stationary and nonlinear localized solutions

A stationary profile is defined by  $u_n(z) = u_n \exp(i\lambda z)$  with the propagation constant or spatial frequency  $\lambda$ . Using this Ansatz in the homogeneous 1D DNLS eq. (2.15), we obtain the following algebraic set of equations

$$\lambda u_n = C(u_{n+1} + u_{n-1}) + \gamma |u_n|^2 u_n. \quad (2.32)$$

In the case of the s-DNLS, the algebraic equations are given by

$$\lambda u_n = C(u_{n+1} + u_{n-1}) - \gamma \frac{u_n}{1 + |u_n|^2}. \quad (2.33)$$

Solutions can be found using, e.g., a multidimensional Newton-Raphson method (see App. A). Equations for higher dimensions or different geometries differ only in the linear part. One has to distinguish two different kinds of stationary solution, the ones having a real amplitude considered in most of the chapters of this thesis and the ones having complex amplitudes, thus an additional phase structure called vortices (see chapter 7). For each solution found one can compute different useful quantities for their characterization in the DNLS and s-DNLS models, which will be used all along this thesis. Model (2.15) possesses two conserved quantities, the optical Power (Norm)

$$P \equiv \sum_{\vec{n}} |u_{\vec{n}}|^2, \quad (2.34)$$

and the Hamiltonian

$$H \equiv - \left\{ \sum_{\vec{n}} \left[ C u_{\vec{n}}^* \Delta_{\vec{n}} u_{\vec{n}} + \frac{\gamma}{2} |u_{\vec{n}}|^4 \right] \right\}, \quad (2.35)$$

The coordinate  $\vec{n}$  depends on the dimension and lattice type [for example,  $\vec{n} = (k, l)$  in a 2D square lattice]. Furthermore,  $\Delta_{\vec{n}} u_{\vec{n}}$  denotes the summation over the nearest neighbors [for example,  $\Delta_{\vec{n}} u_{\vec{n}} = \Delta_n u_n = u_{n+1} + u_{n-1}$  in a 1D lattice] and can be related to the discrete Laplacian. In the case of the s-DNLS, the Power [eq. (2.34)] remains unchanged and the Hamiltonian is given by

$$H \equiv - \left\{ \sum_{\vec{n}} [C u_{\vec{n}}^* \Delta_{\vec{n}} u_{\vec{n}} - \gamma \log(1 + |u_{\vec{n}}|^2)] \right\}. \quad (2.36)$$

There is also a dynamic value, which is very useful. We can define an effective frequency, which considers an instantaneous profile as a stationary one. Using the equation sets for a stationary profile (2.32) or (2.33), one multiplies by  $u_{\vec{n}}^*$  and then sums over all lattice sites yielding, in the case of the cubic DNLS,

$$\lambda_{e,cub} \sum_{\vec{n}} |u_{\vec{n}}|^2 \equiv \lambda_{e,cub} P = \left\{ \sum_{\vec{n}} [C u_{\vec{n}}^* \Delta_{\vec{n}} u_{\vec{n}} + \gamma |u_{\vec{n}}|^4] \right\}. \quad (2.37)$$

and for a saturable system (2.33)

$$\lambda_{e,sat} \sum_{\vec{n}} |u_{\vec{n}}|^2 \equiv \lambda_{e,sat} P = \left\{ \sum_{\vec{n}} \left[ C u_{\vec{n}}^* \Delta_{\vec{n}} u_{\vec{n}} - \gamma \frac{|u_{\vec{n}}|^2}{1 + |u_{\vec{n}}|^2} \right] \right\}. \quad (2.38)$$

The effective frequency can be used to check for stationarity, for example, in dynamic or constraint simulations (see sec. 3.2).

Furthermore, we use the participation number as a quantity to count the number of sites with significant amplitude. It is defined as

$$R \equiv \frac{P^2}{\sum_{\vec{n}} |u_{\vec{n}}|^4}. \quad (2.39)$$

It is an indicator of how many lattice sites are effectively excited in a particular

profile, with the limits of

$$R = \begin{cases} 1 & \text{for } u_n = \delta_{n,n_0} \\ N & \text{for } u_n = \sqrt{P/N}. \end{cases} \quad (2.40)$$

Band edge linear modes tend to the value  $2N/3$  for large arrays.

### 3. Techniques

#### 3.1. Stability Analysis

In this section we will present a standard stability analysis [43] of the s-DNLS as an example, in a general geometry it is given by

$$-i\dot{U}_{n,m} = \Delta U_{nm} - \gamma \frac{U_{n,m}}{1 + |U_{n,m}|^2}, \quad (3.1)$$

where  $\Delta U_{nm}$  denotes the interaction with the neighboring sites, i.e.  $\Delta_{nm} = U_{n+1,m} + U_{n-1,m} + U_{n,m+1} + U_{n,m-1}$  in a 2D square array. We use a perturbed stationary solution Ansatz  $U_{nm} = (\tilde{u}_{nm} + \delta_{nm}) \exp(i\lambda z)$ , where  $\tilde{u}_{nm}$  represents a stationary solution of eq. (3.1) and  $\delta_{nm}$  a (linear) perturbation of this solution. So we get

$$\lambda \tilde{u}_{nm} + \lambda \delta_{nm} - i \frac{\partial \delta_{nm}}{\partial z} = \Delta \tilde{u}_{nm} + \Delta \delta_{nm} - \gamma \frac{U_{nm}}{1 + |U_{nm}|^2}. \quad (3.2)$$

For the last term in first order of the (small) perturbation one gets



$$\begin{aligned}
\gamma \frac{U_{nm}}{1 + |U_{nm}|^2} &\simeq \gamma \frac{\tilde{u}_{nm} + \delta_{nm}}{1 + |\tilde{u}_{nm}|^2 + \tilde{u}_{nm} \delta_{nm}^* + \tilde{u}_{nm}^* \delta_{nm}} = \gamma \frac{\tilde{u}_{nm} + \delta_{nm}}{1 + |\tilde{u}_{nm}|^2} \frac{1}{1 + \frac{\tilde{u}_{nm} \delta_{nm}^* + \tilde{u}_{nm}^* \delta_{nm}}{1 + |\tilde{u}_{nm}|^2}} \\
&\simeq \gamma \left( \frac{\tilde{u}_{nm}}{1 + |\tilde{u}_{nm}|^2} + \frac{\delta_{nm}}{1 + |\tilde{u}_{nm}|^2} \right) \left( 1 - \frac{\tilde{u}_{nm} \delta_{nm}^*}{1 + |\tilde{u}_{nm}|^2} - \frac{\tilde{u}_{nm}^* \delta_{nm}}{1 + |\tilde{u}_{nm}|^2} \right) \\
&= \gamma \frac{1}{1 + |\tilde{u}_{nm}|^2} \left( \tilde{u}_{nm} + \frac{\delta_{nm}(1 + |\tilde{u}_{nm}|^2)}{1 + |\tilde{u}_{nm}|^2} - \frac{\tilde{u}_{nm}^2 \delta_{nm}^*}{1 + |\tilde{u}_{nm}|^2} - \frac{|\tilde{u}_{nm}|^2 \delta_{nm}}{1 + |\tilde{u}_{nm}|^2} \right) \\
&= \gamma \frac{1}{1 + |\tilde{u}_{nm}|^2} \left( \tilde{u}_{nm} + \frac{\delta_{nm}}{1 + |\tilde{u}_{nm}|^2} - \frac{\tilde{u}_{nm}^2 \delta_{nm}^*}{1 + |\tilde{u}_{nm}|^2} \right).
\end{aligned}$$

So (3.2) can be written as

$$\begin{aligned}
-i \frac{\partial \delta_{nm}}{\partial z} + \lambda \delta_{nm} - \Delta \delta_{n,m} + \gamma \left( \frac{\delta_{nm}}{(1 + |\tilde{u}_{nm}|^2)^2} - \frac{\tilde{u}_{nm}^2 \delta_{nm}^*}{(1 + |\tilde{u}_{nm}|^2)^2} \right) \\
= -\lambda \tilde{u}_{nm} + \Delta \tilde{u}_{n,m} - \gamma \frac{\tilde{u}_{nm}}{1 + |\tilde{u}_{nm}|^2} \stackrel{\text{eq. (6.1)}}{=} 0.
\end{aligned}$$

Therefore the evolution equations for the perturbation reads

$$i \frac{\partial \delta_{nm}}{\partial z} - \lambda \delta_{n,m} + \Delta \delta_{nm} - \gamma \left( \overbrace{\frac{\delta_{nm}}{(1 + |\tilde{u}_{nm}|^2)^2} - \frac{\tilde{u}_{nm}^2 \delta_{nm}^*}{(1 + |\tilde{u}_{nm}|^2)^2}}^{=: f(x,y,\alpha,\beta)} \right) = 0. \quad (3.3)$$

Now we split this equation into its real and imaginary part,  $\tilde{u}_{nm} = x_{nm} + iy_{nm}$

$\delta_{nm} = \alpha_{nm} + i\beta_{nm}$ , with  $(x, y, \alpha, \beta) \in \mathbb{R}$ . We get for the fraction

$$\begin{aligned}
f(x, y, \alpha, \beta) &= \frac{\alpha_{nm} + i\beta_{nm} - (\alpha_{nm} - i\beta_{nm})(x_{nm} + iy_{nm})^2}{(1 + x_{nm}^2 + y_{nm}^2)^2} \\
&= \frac{\alpha_{nm}(1 - x_{nm}^2 + y_{nm}^2) - 2\beta_{nm}x_{nm}y_{nm}}{(1 + x_{nm}^2 + y_{nm}^2)^2} \\
&\quad + i \frac{\beta_{nm}(1 + x_{nm}^2 - y_{nm}^2) - 2\alpha_{nm}x_{nm}y_{nm}}{(1 + x_{nm}^2 + y_{nm}^2)^2}.
\end{aligned}$$

Ordering the evolution equations for the perturbations yields

$$\begin{aligned}
\dot{\alpha}_{nm} &= \overbrace{\left[ \frac{2\gamma x_{nm}y_{nm}}{(1 + x_{nm}^2 + y_{nm}^2)^2} \right]}{=: -C_{nm}} \alpha_{nm} + \overbrace{\left[ \lambda - \Delta + \frac{\gamma(1 + x_{nm}^2 - y_{nm}^2)}{(1 + x_{nm}^2 + y_{nm}^2)^2} \right]}{=: A_{nm}} \beta_{nm} \\
\dot{\beta}_{nm} &= \overbrace{\left[ \frac{2\gamma x_{nm}y_{nm}}{(1 + x_{nm}^2 + y_{nm}^2)^2} \right]}{=: C_{nm}} \beta_{nm} + \overbrace{\left[ -\lambda + \Delta - \frac{\gamma(1 - x_{nm}^2 + y_{nm}^2)}{(1 + x_{nm}^2 + y_{nm}^2)^2} \right]}{=: B_{nm}} \alpha_{nm}.
\end{aligned} \tag{3.4}$$

We define the vectors  $\vec{\alpha} = (\alpha_{11}, \dots, \alpha_{NM})$  (and  $\vec{\beta}$  accordingly) to shorten this expression to

$$\begin{pmatrix} \dot{\vec{\alpha}} \\ \dot{\vec{\beta}} \end{pmatrix} = \begin{pmatrix} -\mathbf{C} & \mathbf{A} \\ \mathbf{B} & \mathbf{C} \end{pmatrix} \begin{pmatrix} \vec{\alpha} \\ \vec{\beta} \end{pmatrix} =: \mathbf{M} \begin{pmatrix} \vec{\alpha} \\ \vec{\beta} \end{pmatrix}. \tag{3.5}$$

The submatrices  $\mathbf{A}, \mathbf{B}, \mathbf{C}$  are defined according to (3.4). The eigenvalue spectrum  $\{\omega_{kl}\}$  of the stability matrix  $\mathbf{M}$  yields the information we were looking for: When  $\{\omega_{kl}\}$  has no positive real part, all perturbations at least will not grow, the stability criterion is  $Max[\Re(\omega_{kl})] \leq 0$ .

When the modes are real solutions,  $y_{nm} = 0$ , the submatrix  $C$  vanishes and we end up with the set

$$\dot{\vec{\alpha}} - \mathbf{A}\vec{\beta} = 0$$

$$\dot{\vec{\beta}} - \mathbf{B}\vec{\alpha} = 0$$

or

$$\ddot{\vec{\alpha}} - \mathbf{A}\mathbf{B}\vec{\alpha} = 0$$

$$\ddot{\vec{\beta}} - \mathbf{B}\mathbf{A}\vec{\beta} = 0.$$

The wellknown solutions are harmonic oscillations,  $(\vec{\alpha}, \vec{\beta}) \sim De^{i\Omega_k z} + Ee^{-i\Omega_k z}$ , where  $\Omega_k^2$  are the Eigenvalues of  $(-\mathbf{A}\mathbf{B})$  and  $(-\mathbf{B}\mathbf{A})$ . The stability criterion here is  $\Omega_k \in R$ , since the perturbation mustn't grow. To determine  $\Omega_k = a + ig$ , we use

$$g = \sqrt{\frac{\sqrt{(\text{Re}(\Omega_k^2))^2 + (\text{Im}(\Omega_k^2))^2}}{2}},$$

and finally find stable solutions when the stability parameter  $g = 0$ .

It is also possible to determine the corresponding matrices  $\mathbf{A}$ ,  $\mathbf{B}$  and  $\mathbf{C}$  in eq. (3.5) for the stability analysis of a complex stationary solution of the cubic DNLS (2.15) with coupling  $C = 1$ , they are given by

$$A_{n,m} = -(\Delta - \lambda + \gamma x_{nm}^2 + 3\gamma y_{nm}^2)\delta_{n,m} \quad (3.6)$$

$$B_{n,m} = (\Delta - \lambda + 3\gamma x_{nm}^2 + \gamma y_{nm}^2)\delta_{n,m} \quad (3.7)$$

$$C_{n,m} = 2\gamma x_{nm}y_{nm}\delta_{n,m}, \quad (3.8)$$

with the Kronecker-Delta  $\delta_{n,m}$ .

### 3.2. Constraint method

The constraint method consists in a multidimensional Newton-Raphson method (see App. A) with an additional physical constraint. It is comparable to a Lagrange multiplier textbook method with the only specialty, that in our system we add only ONE constraint equation to a - in general- large set. The constraint method allows us to construct energy surfaces connecting stationary solutions for a given value of power. In that sense, it helps us to effectively predict and interpret the dynamics across the lattice. Critical points will represent stationary solutions, where a coherent movement across the lattice should transform one solution into the other by keeping the power constant [39]. The method was originally introduced by Aubry and Cretegny [48] and then implemented by Savin et al. [94] to study the mobility of kinks in nonlinear Klein-Gordon lattices (see also Ref. [95, 96] for a related approach to analyze travelling breathers in 1D oscillator chains in terms of an effective Hamiltonian.) Lately, it was numerically implemented to analyze surface states in one-dimensional semi-infinite systems [97, 98]. By adiabatically changing the amplitude in one particular site, specifically chosen as the one after the main peak (the peak is at  $n_c$  and the constrained amplitude at  $n_c + 1$ ), the one- and the two-site solutions could be connected. Ending the sweep when  $u_{n_c} = u_{n_c+1}$  and the center of mass of the constrained solution,  $X$ , has varied from  $n_c$  to  $n_c + 0.5$ , a one-dimensional energy surface,  $H$  vs  $X$ , can be sketched. Technically speaking, the method used in Ref. [97, 98] consists on eliminating one equation from the Newton-Raphson problem, the one of the constrained amplitude which is not anymore an unknown

variable. However, as the power is kept constant, an equation for  $P$  is added and the frequency  $\lambda$  becomes a variable completing the variable-equations set.

We implemented a method where we explicitly vary the center of mass instead of the amplitude. In 1D, the center of mass is given by

$$X \equiv \frac{\sum_n n |u_n|^2}{P}. \quad (3.9)$$

We choose the site  $n_A$  with fixed amplitude  $A$  given by

$$A = \sqrt{\frac{XP - \sum_{n \neq n_A} n |u_n|^2}{n_A}}. \quad (3.10)$$

Now we can start to slightly change  $X$  and solve the new set keeping  $P$  constant.

For the 2D lattice we also implement a constraint method for two fixed centers of masses (and amplitudes). Since we are interested in the energy landscape around the fundamental stationary solutions, we will assume also the amplitude  $u_{n,m}$  of the constrained solutions to be real and positive on the constraint sites. Then, from the definition of the center of mass coordinates in the horizontal and vertical directions,

$$X \equiv \frac{\sum_{nm} n |u_{n,m}|^2}{P} \quad \text{and} \quad Y \equiv \frac{\sum_{nm} m |u_{n,m}|^2}{P}, \quad (3.11)$$

we can solve for any pair of amplitudes  $A \equiv u_{n_A, m_A}$  and  $B \equiv u_{n_B, m_B}$  at places  $\{n_A, m_A\}$  and  $\{n_B, m_B\}$ :

$$A = \sqrt{\frac{m_B S_n - n_B S_m + P(n_B Y - m_B X)}{n_B m_A - n_A m_B}}, \quad (3.12)$$

$$B = \sqrt{\frac{n_A S_m - m_A S_n + P(m_A X - n_A Y)}{n_B m_A - n_A m_B}}.$$

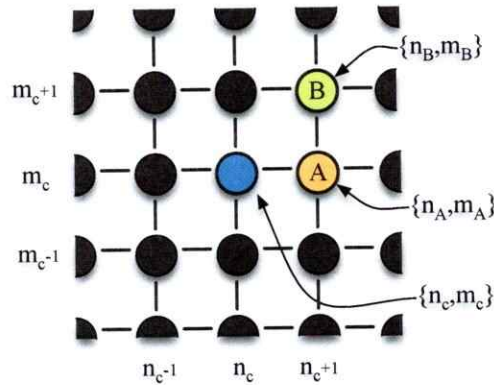


**Figure 3.1.:** Array scheme showing the constraint locations used to obtain the energy surfaces below.

where  $S_j \equiv \sum_{nm} (1 - \delta_{n,n_A} \delta_{m,m_A} - \delta_{n,n_B} \delta_{m,m_B}) j |u_{n,m}|^2$  with  $j = n, m$ . Thus, as before, the actual constraints will be in the amplitudes  $A$  and  $B$ , but now we can tune the center of mass as wished, from a given initially stationary solution towards any other. In general, the constrained solutions obtained in this way will of course not be stationary solutions of the full system. To identify any stationary solution - including the intermediate ones - we check whether the value of  $\lambda$  obtained from the constrained Newton-Raphson scheme coincides with the frequency of a hypothetical true stationary solution to the full equation set with the computed amplitude profile. Furthermore, constrained solutions allow us to calculate their Hamiltonian, and therefore to construct an effective energy landscape.

The choice for positions  $\{n_A, m_A\}$  and  $\{n_B, m_B\}$  is evidently not unique, but in order to most efficiently trace out a smooth energy landscape connecting the fundamental solutions (if it exists), the constraint sites should preferably be chosen within the unit cell where the amplitudes are large. It turned out that, starting from a stationary one-site solution centered at  $\{n_c, m_c\}$ , in most cases the best option is to choose

the first constraint at site  $\{n_c + 1, m_c\}$  or  $\{n_c, m_c + 1\}$ , and the other one at site  $\{n_c + 1, m_c + 1\}$ , as sketched in Fig. 3.1. The results shown in the following sections are obtained using these constraint sites. We also tried using constraint sites at  $\{n_c + 1, m_c\}$  and  $\{n_c, m_c + 1\}$  (i.e., along a diagonal); however, with this choice we typically were not able to find the solution centered in between four-sites when starting from the one-site mode. Instead, the NR method with constraints on these sites generally converges, at  $X = n_c + \frac{1}{2}, Y = m_c + \frac{1}{2}$ , to a two-site diagonal solution. This is an exact solution for the unconstrained cubic DNLS at high powers, but to the s-DNLS only for larger nonlinearities than the ones considered in Chap. 6.

## 4. Fano resonances

The eigenmodes of a linear periodic array are plane Bloch waves. In the presence of one or few “impurities” the translational invariance is broken; so the presence of judiciously placed defects makes possible interesting resonance phenomena, such as Fano resonances (FR)[5], where there is total reflection of plane waves through the impurity region, in an otherwise periodic potential. In a typical FR system, the wave propagation in the presence of a periodic scattering potential is characterized by open and closed channels. The open channel guides the propagating waves as long as the eigenfrequencies of closed channels do not match the spectrum of linear waves. The total reflection of waves in the open channel occurs when a localized state originating from one of the closed channels resonates with the open channel spectrum. The original setting [5] considered two weakly coupled harmonic oscillators, one of them driven by a periodic force. Since the interaction of plane wave eigenmodes (band) of a periodic potential with defects (discrete mode) is ubiquitous in physical systems, reported Fano resonances are nearly countless. To name only a few, they have been found in wells with a quantum dot in an Aharonov-Bohm interferometer[6], in the electronic transport through a single-electron transistor [7], in arrays of sub-



wavelength holes in metal films [8], quantum well structures [9], electron waveguides containing donor impurities [10], in a quantum wire with a side-coupled quantum dot [11], semiconductor quantum wells [12], weakly coupled single-electron transistors [13], bulk semiconductors [14], biased semiconductor superlattices [15], carbon nanotubes [16], and plasmonic nanowires [17]. These are only a few of the more than 6000 citations of the original work of Ugo Fano (see Ref. [18] for a review of recent findings).

Scattering of plane waves can not only be caused by linear impurities, but is also observed in nonlinear waveguide arrays: Nonlinearity generates several scattering channels which can lead to resonances due to destructive interference and, as a consequence, to total absence of transmission similar to the original Fano problem. As examples we can cite the prediction of Fano resonances in the context of nonlinear quadratic waveguide arrays [20] and also, in a very different research area, the prediction of similar resonances in Bose-Einstein condensates [21].

In this chapter we will consider different linear defects leading to Fano resonances in the context of metamaterials in section 4.1 and a nonlinear Fano setting in saturable waveguide arrays in section 4.2.

#### 4.1. Linear Fano resonances in Split-ring resonator arrays

The FR effect can be used to control the electromagnetic response in novel, man-made materials, such as metamaterials (MM). They are characterized for having negative dielectric permittivity and negative magnetic permeability over a finite frequency

range, endowing them with unusual electromagnetic wave propagation properties [105, 106]. One of the most studied MMs is a metallic composite structure consisting of arrays of wires and split-ring resonators (SRRs). The theoretical treatment of such structures relies mainly on the effective-medium approximation where the composite is treated as a homogeneous and isotropic medium, characterized by effective macroscopic parameters. The approach is valid, as long as the wavelength of the electromagnetic field is much larger than the linear dimensions of the MM constituents. The magnetic properties of SRR arrays have been explored in a number of works [107] - [114].

In this section, we consider Fano resonance effects due to few defects whose position, with respect to the periodic SRR array can be easily tuned, making this type of configuration an interesting one to probe experimentally.

Let us consider a one-dimensional, periodic array of split-ring resonators (SRRs), in the absence of nonlinearity, driving and dissipation. The most simple form of a split-ring resonator is that of a small, conducting ring with a slit. In general, each SRR unit in the array can be mapped to a resistor-inductor-capacitor (RLC) circuit featuring self-inductance  $L$ , ohmic resistance  $R$ , and capacitance  $C$  built across the slit. In our case, we will consider the case of negligible resistance  $R$ . Thus, each SRR unit possesses a resonant frequency  $\omega_0 \approx 1/\sqrt{LC}$ . In the array, each SRR is coupled to their nearest neighbor via mutual induction [107].

The evolution equation for the charge  $Q_n$  residing on the  $n$ th ring is

$$\frac{d^2}{dt^2} \left( LQ_n + \sum_{m \neq n} M_{nm} Q_m \right) + \frac{Q_n}{C} = 0, \quad (4.1)$$

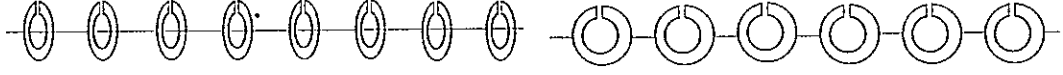


Figure 4.1.: Two typical configurations for the SRR array.

where  $M_{nm}$  is the mutual induction between rings  $n$  and  $m$ . We cast this equation in dimensionless form by defining  $\tau \equiv \omega_0 t$ ,  $q_n \equiv Q_n / CU_0$ ,  $\lambda_{nm} \equiv M_{nm} / L$ , where  $U_0$  is a characteristic voltage across the slits.

The dimensionless evolution equation for the charge  $q_n$  residing on the  $n$ th ring reads now

$$\frac{d^2}{d\tau^2} \left( q_n + \sum_{m \neq n} \lambda_{nm} q_m \right) + q_n = 0, \quad (4.2)$$

where  $\lambda_{nm}$  denotes the ratio of the mutual inductances between the  $n$ th and the  $m$ th ring to the self inductance of the rings, and decreases as the inverse cube of the ring-to-ring distance,  $\lambda_{nm} \propto |n - m|^{-3}$  ( $m \neq n$ ). In the limit of weak coupling (large distance between SRR units), it is customary to take  $\lambda_{nm} = \lambda \delta_{n,m}$ .

The two most simple SRR configurations are shown in 4.1. In one of them (left), all couplings are positive, while for the second (right), they are all negative, as a result of Lenz's law. The stationary modes of Eq.(4.2) are obtained by posing a solution in the form  $q_n(t) = q_n \exp(i\Omega\tau)$ . This leads to the stationary equations,

$$-\Omega^2 \left( q_n + \sum_{m \neq n} \lambda_{nm} q_m \right) + q_n = 0. \quad (4.3)$$

Magnetoinductive plane waves of the form  $q_n = A \exp(ikn)$ , lead to the dispersion relation

$$\Omega^2 = \frac{1}{1 + 2 \sum_{m>0} \lambda_{0m} \cos(km)}. \quad (4.4)$$

We must impose the physical condition  $\Omega^2 > 0$ . Using that  $\lambda_{0m}$  has the form

$\lambda_{0m} = \lambda/m^3$  leads to:

$$-\frac{1}{2\zeta(3)} < \lambda < \frac{2}{3\zeta(3)}, \quad (4.5)$$

or,  $-0.41595 < \lambda < 0.554605$ , where  $\zeta(s)$  is the Riemann Zeta function  $\zeta(s) = \sum_{k=1}^{\infty} k^{-s}$ . As we will see, the limits in condition (4.5) change a bit when one assumes a weak coupling limit where few or even only one of the  $\lambda_{0m}$  is retained.

#### 4.1.1. Magnetoinductive defects and Fano resonances

We consider now several simple cases involving defects coupled to the SRR array. These defects are created, for instance, by altering the electromagnetic characteristics of some rings, which can be achieved by changing one or more geometric features of the rings. Another way is by altering their relative coupling with respect to the array. In the case where nonlinearity and dissipation are not considered, two simple choices are to alter the slit width of a ring which alters its capacity only, affecting the value of its resonant frequency. Another simple choice is to couple the array to one or several external defect consisting of a ring placed outside the SRR array. This affects the value of the coupling between the SRR and the external ring only.

##### 4.1.1.1. Single capacitance impurity

The first case we study is a single capacitance impurity embedded in the array (Fig. 4.2), which, without loss of generality, we place at  $n = 0$ . This impurity is created by changing the slit width of the ring at  $n = 0$ . The stationary equation for this case

is

$$-\Omega^2(q_n + \sum_{m \neq n} \lambda_{nm} q_m) + (1 + \delta_{n,0} \Delta) q_n = 0, \quad (4.6)$$

where  $\Delta$  is the change in the (dimensionless) resonance frequency at the defect position. When the slit width tends to zero, its capacitance diverges, making the resonant frequency approach zero. This implies  $\Delta \rightarrow -1$ . On the other hand, when the slit width is large, the local capacitance goes to zero, and the resonant frequency diverges, implying that  $\Delta \rightarrow \infty$ . Thus,  $-1 < \Delta < \infty$ .

Usually, embedded defects coupled locally do not lead to Fano Resonance phenomena (perfect plane-wave reflection). In the SRR array, however, the couplings are dipolar and therefore, long-range, and non-local effects have to be considered. For computational simplicity we will work with couplings to first- and second nearest neighbors only. The hope is that interference between the path through nearest neighbors and the one through next-nearest neighbors will give rise to Fano Resonances. Equation (4.6) becomes:

$$-\Omega^2 [q_n + \lambda(q_{n+1} + q_{n-1}) + \lambda'(q_{n+2} + q_{n-2})] + (1 + \Delta_{n0}) q_n = 0. \quad (4.7)$$

where  $\lambda'$  is the coupling among next-nearest neighbors. We pose a plane wave solution of the form

$$q_n = \begin{cases} I e^{ikn} + R e^{-ikn} & , n < -1 \\ T e^{ikn} & , n > 1. \end{cases} \quad (4.8)$$

After replacing this *ansatz* into (4.7), one obtains after a little algebra:

$$\Omega^2 = \frac{1}{1 + 2\lambda \cos(k) + 2\lambda' \cos(2k)} \quad (4.9)$$

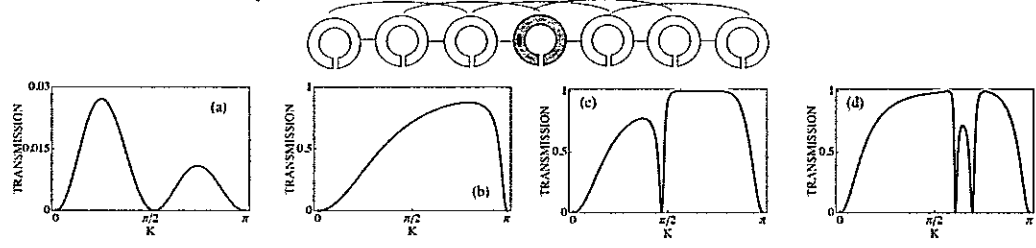


**Figure 4.2.:** Top: Capacitive defect embedded in SSR array, with couplings to first-and second nearest neighbors. Bottom: (a)-(d) show the transmission coefficient vs. wavenumber, for several parameter values: (a)  $\lambda = -0.1, \lambda' = (1/8)\lambda, \Delta = 0.7$ , (b)  $\lambda = 0.4, \lambda' = 0.21, \Delta = -0.5$ , (c)  $\lambda = 0.4, \lambda' = 0.21, \Delta = 0.5$ , (d)  $\lambda = 0.4, \lambda' = 0.21, \Delta = 1.0$ .

and

$$t \equiv |T/I|^2 = \left| \frac{A + \Delta B}{A + \Delta C} \right|^2, \quad (4.10)$$

where

$$\begin{aligned} A &= -2i \sin(k) [2\lambda'^3 \cos(3k) + 6\lambda\lambda'(\lambda \cos(k) + \lambda' \cos(2k)) \\ &\quad + \lambda(\lambda^2 + 3\lambda'^2)] \\ B &= -2i \sin(k) [2\lambda\lambda'(\lambda \cos(k) + \lambda' \cos(2k)) + \lambda\lambda'] \\ C &= [(1 + 2\lambda \cos(k) + 2\lambda' \cos(2k))(\lambda^2 + 2\lambda\lambda'e^{-ik} \\ &\quad - \lambda'^2 + 2\lambda'^3 \cos(2k))]. \end{aligned} \quad (4.11)$$

Now, for the SRR case where dipolar interactions fall with the inverse cube of the distance between SRR units, we have  $\lambda' = (1/8)\lambda$ . After inserting this into Eqs.(4.9) and (4.10) and after imposing  $\Omega^2 > 0$ , we conclude that  $-(4/9) < \lambda < (4/7)$  is the relevant coupling regime for this SRR configuration. Inside this regime it is possible to have a relatively weak Fano resonance, as shown in Fig. 4.2(a). As expected,

when coupling to second nearest neighbors is neglected ( $\lambda' = 0$ ), there is no FR at all, since in that case the transmission becomes

$$t = \frac{(2\lambda \sin(k))^2}{(2\lambda \sin(k))^2 + \Delta^2(1 + 2\lambda \cos(k))^2}, \quad (4.12)$$

which can only be zero at  $k = 0, \pi$ . For more general  $\lambda, \lambda'$  values, it is possible to have zero, one, and even two different strong Fano resonances, as shown in Fig. 4.2(b)-(d) respectively.

#### 4.1.1.2. Single inductive impurity

Another simple case is a single inductive impurity embedded in the array. This is achieved by placing a SRR unit at different distances from the left and right portions of the array, leading to asymmetrical couplings  $\lambda_L$  and  $\lambda_R$ . Only couplings between nearest-neighbors are assumed. This case was already considered [115]. In this case, it can be proven that there is no FR for any choice of  $\lambda_L, \lambda_R$ ; the transmission vs wavevector curve shows a single maximum at  $k = \pi/2$ . For the special symmetric case  $\lambda_L = \lambda_R$ , there is a transmission resonance ( $t = 1$ ) at  $k = \pi/2$ .

We move now to simple cases where the defect(s) lie(s) outside the SRR array, and thus, their coupling can be tuned by changing their distance to the array.

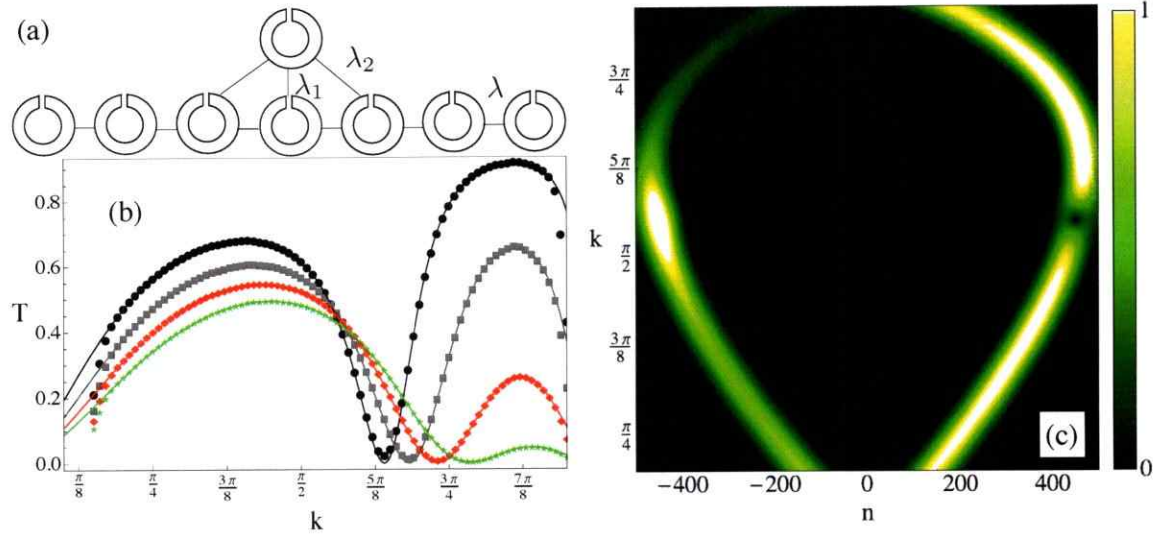


**Figure 4.3.:** (a) SRR array with external inductive defect. (b) Transmission coefficient vs wavevector, for different values of the relative coupling defect. The lines show the theoretical results, symbols the direct numerical integration:  $\lambda_1/\lambda = 1.25$ (circles), 1.5(squares), 1.75 (rhombi) and 2.0(stars). (c) Output profile after  $t = 1500$  as a function of wavevector and ring site, for  $\lambda_1/\lambda = 1$ . Impurity site is located at  $n = 0$ .

#### 4.1.2. Single external inductive defect: First case

The first case of this type is that of a single external inductive defect coupled to the SRR at  $n = 0$  *via* coupling to first and second nearest neighbors via coupling parameters  $\lambda_1$  and  $\lambda_2$ , respectively (Fig. 4.3(a)). From the geometry of the configuration, it is easy to obtain the relationship

$$\frac{\lambda_2}{\lambda} = \left[ 1 + \left( \frac{\lambda}{\lambda_1} \right)^{2/3} \right]^{-3/2}. \quad (4.13)$$

For simplicity, we assume only nearest neighbor coupling among the SRR units. For this approximation to be consistent, one must impose  $\lambda_1, \lambda_2 > (1/8)\lambda$ . From Eq.(4.13), this implies  $\lambda_1/\lambda > \text{Max}\{(1/8), 3^{-3/2}\} = 3^{-3/2} = 0.192$ .



The stationary equations for this case are

$$\begin{aligned} -\Omega^2[\lambda(q_{n+1} + q_{n-1}) + q_n + q_e(\lambda_1\delta_{n,0} + \lambda_2\delta_{n,\pm 1})] + q_n &= 0 \\ -\Omega^2(\lambda_1q_0 + \lambda_2q_{\pm 1} + q_e) + q_e &= 0, \end{aligned} \quad (4.14)$$

where  $q_e$  is the charge residing on the external defect ring. We assume a plane wave solution of the form

$$q_n = \begin{cases} I e^{ikn} + R e^{-ikn} & , n \leq -1 \\ T e^{ikn} & , n \geq 1. \end{cases} \quad (4.15)$$

The transmission coefficient for this configuration becomes

$$t \equiv |T/I|^2 = \left| \frac{4 \left( \left( \frac{\lambda_1}{\lambda} \right) \left( \frac{\lambda_2}{\lambda} \right) + \left( 1 + \left( \frac{\lambda_2}{\lambda} \right)^2 \right) \cos(k) \right) \sin(k)}{\left( \frac{\lambda_1}{\lambda} \right)^2 + 4e^{ik} \left( \frac{\lambda_1}{\lambda} \right) \left( \frac{\lambda_2}{\lambda} \right) + (1 + e^{2ik}) \left( \frac{\lambda_2}{\lambda} \right)^2 + 2i \sin(2k)} \right|^2, \quad (4.16)$$

where  $\lambda_2$  is given by Eq.(4.13) for the SRR system. The most interesting feature of this transmission coefficient is the presence of a Fano resonance, whose position varies with the value of  $\lambda_1/\lambda$  (see Fig. 4.3(b)). The FR occurs when  $\lambda_1\lambda_2 + (\lambda^2 + \lambda_2^2) \cos(k) = 0$ , which is possible, from Eq.(4.13), for all  $0 < |\lambda_1/\lambda| < 2.449$ . Therefore, the relevant interval where FR exists in our model is given by  $0.192 < \lambda_1/\lambda < 2.449$ . This can be achieved by simply changing the distance between the SRR array and the external defect. Note from Eq.(4.16) that, if we neglect the effect of  $\lambda_2$ , the position of the FR remains locked at  $k = \pi/2$ .

To get a better feeling for what would be expected to see in an actual experiment for this system, we perform a numerical simulation of a wide pulse impinging on the inductive impurity region. We used an array of  $10^3$  rings and resort to a symplectic algorithm (see App. B) to trace the time evolution of an initial broad gaussian pulse

$u_n(0) = A \exp[-\alpha(n-n_0)^2] \exp[ik(n-n_0)]$ , where  $n_0 = -300$ ,  $A = 0.1$  and  $\alpha = 0.001$  which means a width of about 120 sites, in order to simulate a plane wave with a well-defined  $k$ . The rings coupled to the inductive defect are placed at  $n = 0, \pm 1$ . Figure 4.3(b) shows numerical simulation results for the transmission coefficient vs wavevector for several  $\lambda'/\lambda$  values, with  $\lambda = 0.4$ . The agreement between analytics (lines in Eq.(4.16)) and numerics (symbols) is excellent, and the Fano resonances are clearly shown. The numerical discrepancies at wavevectors close to  $k = 0, \pi$  are due to the long integration times needed since the pulse is quite slow at these  $k$  values. In Fig. 4.3(c) we show the output profile of the gaussian pulse for different  $k$ -values, after an integration time  $t = 1500$ . The transmission increases monotonically up to  $k \approx 0.389 \pi (0.868 \pi)$  from the bottom (top), then decreases steadily until it vanishes completely at  $k \approx 0.601\pi$ , where the Fano Resonance is located.

#### 4.1.3. Single external inductive defect: Second case

The next case we consider is a variation of the previous one, where the external defect is now located halfway between two SRR units (Fig. 4.4(a)). Without loss of generality, we take the external defect coupled symmetrically to the units at  $n = 0$  and  $n = 1$ , with coupling  $\lambda'$ . As before, the units in the array interact through nearest-neighbor couplings  $\lambda$  only. In order for this approximation to be consistent, and taking into account the dipolar nature of the inductive couplings, we need  $|\lambda'| > (1/8)\lambda$ .

The stationary equations read

$$\begin{aligned} -\Omega^2[\lambda(q_{n+1} + q_{n-1}) + q_n + \lambda'q_e(\delta_{n,0} + \delta_{n,1})] + q_n &= 0 \\ -\Omega^2[\lambda'(q_0 + q_1)] + q_e &= 0, \end{aligned} \quad (4.17)$$

where  $q_e$  is the charge on the external defect ring. We pose a plane wave solution of the type

$$q_n = \begin{cases} I e^{ikn} + R e^{-ikn} & , n \leq -1 \\ T e^{ikn} & , n \geq 2. \end{cases} \quad (4.18)$$

leading to a transmission coefficient:

$$t \equiv \left| \frac{T}{I} \right|^2 = \left| \frac{(e^{ik} - 1)(\lambda'^2 + 2\lambda^2 \cos(k))}{2(\lambda'^2 + \lambda^2 \cos(k)(1 - e^{ik}))} \right|^2. \quad (4.19)$$

Fano resonances are possible when  $\lambda'^2 + 2\lambda^2 \cos(k) = 0$ . This implies,  $k_F = -(1/2)(\lambda'/\lambda)^2$ , which is possible only if  $|\lambda'/\lambda| < \sqrt{2}$ . This constraint plus the consistency condition, give us the relevant coupling parameter window for this SRR configuration:

$$(1/8) < \left| \frac{\lambda'}{\lambda} \right| < \sqrt{2}. \quad (4.20)$$

Figure 4.4(b) shows some transmission curves for parameter values inside and outside this window. The position and width of the Fano resonance depend on the ratio  $|\lambda'/\lambda|$ , which can be externally tuned by changing the distance between the defect and the array. Figure 4.4(c) shows output intensity profile after propagation of  $t = 1500$  as a function of wavevector and site position.

In conclusion, we have examined extensively Fano resonance effects in a SRR array coupled to internal (capacitive) and external (inductive) defects. In the case of internal or embedded defects, the presence of coupling to second neighbors, in addition to

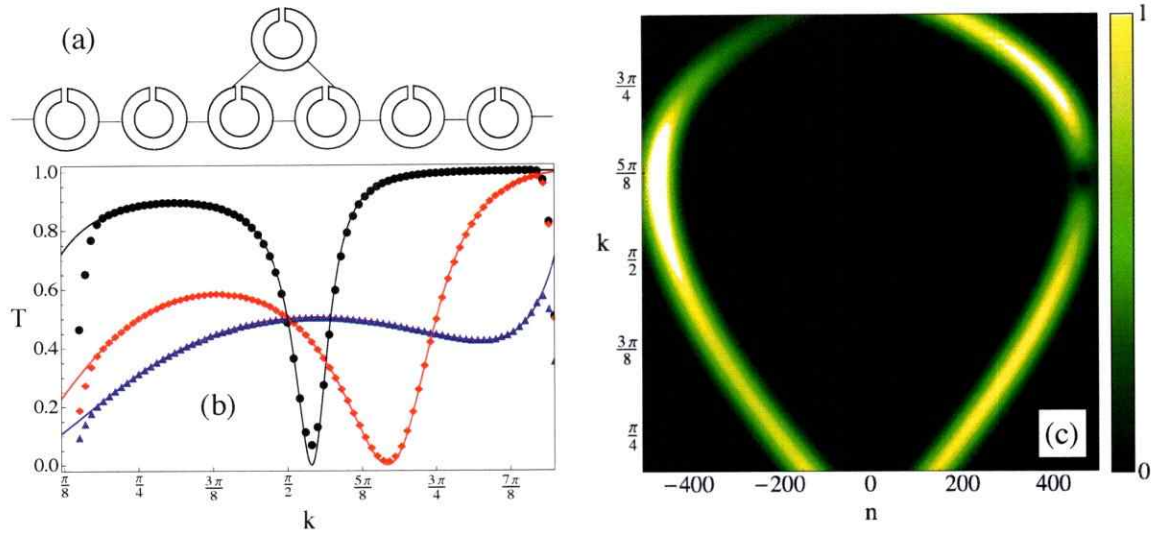


**Figure 4.4.:** (a) External defect coupled symmetrically to the SSR array. Only couplings to first nearest neighbors are considered. (b) Transmission vs wavevector for several  $\lambda'/\lambda$  values: 0.5 (circles), 1.0 (rhombi) and 1.5 (triangles). (c) Output profile after  $t = 1500$  as a function of wavevector and ring site, for  $\lambda_1/\lambda = 1$ .

the customary first neighbor coupling, is necessary to induce the FR phenomenon. For external defects, the FR phenomenon depends mainly of the geometric configuration between the defect(s) and the SRR array. The position and strength of these FR could be easily tuned in current experiments, and constitute a clear example of the possibility of controlling the transport of electromagnetic waves across a periodic magnetic metamaterial.

## 4.2. Nonlinear Fano-Resonances in saturable waveguide arrays

In the present section, we study a saturable nonlinear impurity embedded in a linear waveguide array as a new possible experimental setup to observe Fano resonances. Recently, scattering of plane waves by bright and dark solitons has been experimentally studied in saturable nonlinear media [116] but, to the best of our knowledge, no direct observation of Fano resonances has been implemented yet in discrete media. We also characterize the main properties of nonlinear impurity modes (NLM) in this type of system and suggest the possibility of a switching-mode scheme, based on a judicious tuning of the system parameters.

We consider the s-DNLS (2.29) equation in a dimensionless form with a defect, composed by a linear and a nonlinear part at one site ( $n = n_i$ ) of a 1D waveguide array:

$$-i \frac{\partial u_n}{\partial z} = (u_{n+1} + u_{n-1}) + \left( \epsilon - \frac{\beta}{1 + |u_n|^2} \right) u_n \delta_{n, n_i}. \quad (4.21)$$

$\epsilon$  is the strength of the linear defect and  $\beta$  the nonlinear coefficient. We include both type of defects, linear and nonlinear, in order to deal with a more general problem. A linear site impurity can be created by altering the geometry of a given waveguide, while at the same time tuning the spacing with its nearest-neighbors in order to keep its coupling with the rest of the array unaltered. On the other hand, the nonlinear response at the impurity site can be boosted by a judicious amount of extra metal doping [117].

First, we look for stationary localized solutions centered at site  $n_i$ . We insert

into (4.21) the ansatz  $u_n(z) \equiv U_n(z) = U_0 x^{|n-n_i|} e^{i\lambda z}$  with  $U_0, x \in R$ .  $U_0$  is the impurity-mode amplitude and  $x$  determines its localization length. By defining  $g \equiv \beta/(1 + U_0^2)$  and imposing  $|x| < 1$  we obtain:  $x = (g - \epsilon)/2 \pm \sqrt{1 + (g - \epsilon)^2/4}$  and  $\lambda = \pm \sqrt{4 + (g - \epsilon)^2}$ . The relation between  $g$  and  $\epsilon$  determines the sign of  $\lambda$ . For  $g > \epsilon$  ( $g < \epsilon$ ) the sign is minus (plus),  $x$  and  $\lambda < 0$  ( $x$  and  $\lambda > 0$ ), and the solution is staggered (unstaggered). The optical power is defined as  $P \equiv \sum_n |u_n|^2 = U_0^2 \sqrt{4 + (g - \epsilon)^2} / |g - \epsilon|$ . Hereafter, we fix  $\beta = 10$  and  $\epsilon = 5$  (Thus, if  $U_0 = 1 \rightarrow g = \epsilon$ ). Figure 4.5 shows power vs propagation constant of the impurity mode. From Fig.4.5(a) we see that there is no power threshold for staggered modes (which are always linearly stable). On the other hand, unstaggered modes possess a threshold that separates two regimes:  $\partial P/\partial \lambda < 0$  unstable and  $\partial P/\partial \lambda > 0$  stable solutions. When nonlinear modes approach the linear band ( $|g - \epsilon| \rightarrow 0$ ), the optical power diverges. This amplitude-dependent “transition” implies that, unlike other impurity systems, for a single saturable impurity, one could switch from a staggered to an unstaggered mode just by varying the input power.

Now, we look for Fano resonances, i.e. what would happen, if a small-amplitude plane wave is scattered by our nonlinear impurity mode. In the impurity region, where the interaction takes place, a “local mode” can be generated [21]. This mode corresponds to an extra channel, which is created by the interaction. When this mode is fully excited, a zero transmission of plane waves may occur due to destructive interference, and a Fano resonance appears [18]. We assume the plane wave amplitude  $\phi_n(z)$  to be much smaller than the impurity-mode amplitude, i.e.  $|\phi_0| \ll |U_0|$ . We insert

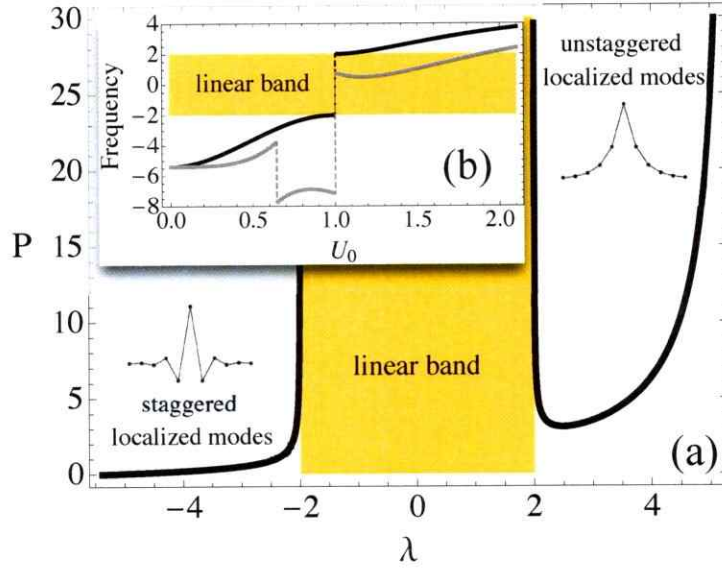


**Figure 4.5.:** (a)  $P$  vs  $\lambda$  diagram for NLM. (b)  $\lambda$  vs  $U_0$  for NLM (black lines) and  $\omega_{cc}$  vs  $U_0$  for local modes (gray lines),  $\beta = 10$  and  $\epsilon = 5$ .

$u_n(z) = U_n(z) + \phi_n(z)$  and linearize (4.21) with respect to  $\phi_n(z)$  obtaining:

$$-i \frac{\partial \phi_n}{\partial z} = \phi_{n+1} + \phi_{n-1} + \left( \epsilon - \frac{g^2}{\beta} \right) \phi_0 \delta_{n,n_i} + \frac{g^2}{\beta} U_0^2 e^{2i\lambda z} \phi_0^* \delta_{n,n_i}. \quad (4.22)$$

To solve this problem, we use the ansatz  $\phi_n(z) = a_n e^{i\omega z} + b_n^* e^{i(2\lambda - \omega)z}$  in (4.22), obtaining two coupled discrete equations:

$$\omega a_n = (a_{n+1} + a_{n-1}) + L a_n \delta_{n,n_i}, \quad (4.23)$$

$$(2\lambda - \omega) b_n = (b_{n+1} + b_{n-1}) + L b_n \delta_{n,n_i}, \quad (4.24)$$

where  $Lc_n \equiv (\epsilon - g^2/\beta) c_n + (g^2 U_0^2/\beta) d_n$  with  $c_n \neq d_n$  ( $c_n, d_n = a_n, b_n$ ).  $a_n$  corresponds to the open channel, i.e. a traveling plane wave with a frequency given by  $\omega_k = 2 \cos k$ .  $k$  is the plane wave vector which, in a experiment, is related to the input angle. Therefore, the linear band covers the region  $[-2, 2]$ .  $b_n$  corresponds to a closed channel, whose frequency is determined by the interaction. The resonance

occurs when the open channel amplitude at the impurity site is zero and the local mode is fully excited. Therefore, we decouple (4.24) [taking  $a_0 = 0$ ] and look for localized solutions of the form  $b_n = b_0 y^{|n-n_i|}$  with  $|y| < 1$ . We find that the frequency of this mode is  $\omega_{cc} = 2\lambda \pm \sqrt{4 + (\epsilon - g^2/\beta)^2}$ , where the plus (minus) sign holds for  $\epsilon < g^2/\beta$  ( $> g^2/\beta$ ), and  $\lambda > 0$  ( $< 0$ ) if  $g < \epsilon$  ( $> \epsilon$ ). We notice that a resonance is only possible when the frequency of the open channel matches the frequency of the closed one. It can be proved that  $\omega_{cc} \in [-2, 2]$  for  $\beta > \epsilon > 0$ . In any other case,  $\omega_{cc}$  will be outside of the band and no resonances will be observed. This condition also implies that the linear impurity is absolutely necessary for having Fano resonances in the present model. Fig.4.5(b) shows the existence region of the local nonlinear mode as a function of  $U_0$ . The frequency  $\omega_{cc}$  lies inside the linear band approximately for  $U_0 \in [1, 1.9]$  and, therefore, only in such a region a plane wave can excite a local mode and, in principle, be totally reflected.

The scattering problem is studied by considering an incoming plane wave and a localized local mode:

$$a_n = \begin{cases} I e^{ik(n-n_i)} + R e^{-ik(n-n_i)} ; & n < n_i \\ T e^{ik(n-n_i)} & ; n \geq n_i \end{cases},$$

$$b_n = b_0 y^{|n-n_i|}.$$

By inserting this ansatz in (4.23) and (4.24) at sites  $n = n_i, n_i \pm 1$  we find, that  $T = I + R$  and  $\omega \equiv \omega_k = 2 \cos k$ . By solving the algebraic problem we get the transmission coefficient  $t \equiv |T/I|^2$  in closed form as  $t = 4 \sin^2 k / [4 \sin^2 k + \Omega^2(k)]$



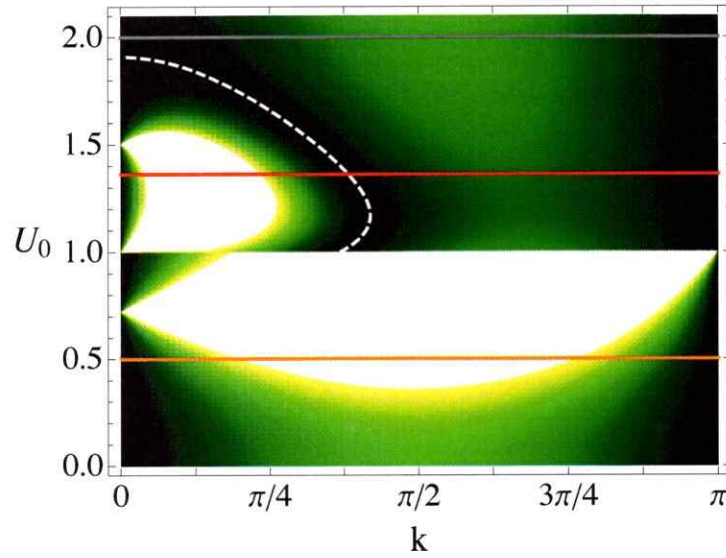


**Figure 4.6.:** Transmission coefficient  $T$  as a function of beam angle  $k$  and amplitude  $U_0$ . Bright (dark) regions denote high (low)  $T$ . Dashed line marks places where  $\omega_k = \omega_{cc}$  and  $T = 0$ .

where,

$$\Omega(k) = \left[ \epsilon - \frac{g^2}{\beta} + \frac{g^4 U_0^4 / \beta}{\pm 2 \sqrt{(\lambda - \cos k)^2 - 1} + \frac{g^2}{\beta} - \epsilon} \right], \quad (4.25)$$

where the plus (minus) sign is used if  $\lambda - \cos k > 1$  ( $< 1$ ). By fixing  $\beta$  and  $\epsilon$ , the remaining free parameters are the beam angle  $k$  and the amplitude  $U_0$ . Figure 4.6 shows the transmission coefficient in terms of  $k$  and  $U_0$ . First, we clearly see that  $t = 0$  (Fano resonance) appears only in the range  $U_0 \sim \{1, 1.9\}$  where the frequency of the open channel can coincide with the frequency of the closed channel. Second, resonances are only possible when the NLM is unstaggered ( $U_0 > 1$ ). This picture suggests a high degree of controllability of the transmission coefficient: By choosing different input powers and/or different input beam angles, we can efficiently control the amount of light going through or reflected back from the impurity region.

We perform numerical simulations of (4.21) in order to confirm our theoretical find-

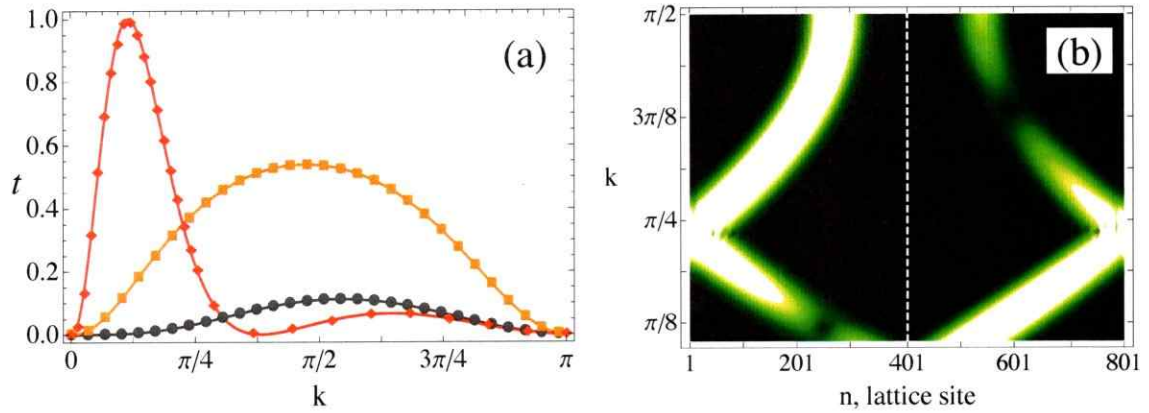


**Figure 4.7.:** (a)  $t$  vs  $k$  for  $U_0 = 0.5$  (squares), 1.36 (diamonds), and 2 (circles). (Lines correspond to theoretical  $t$  and symbols to numerical simulations results.) (b) Linear output profile for different  $k$  and  $U_0 = 1.36$ . The dashed line marks the position of the impurity site.

ings. As an initial condition, we take a localized nonlinear impurity mode  $U_0 x^{|n-n_i|}$  and an incoming plane wave initially centered at  $n_0$ :

$$\phi_n = \phi_0 \exp[-\alpha(n - n_0)^2] \exp[ik(n - n_0)].$$

The initial amplitude  $\phi_0 = 0.01$  was chosen very small compared to  $U_0$  to fulfill the analytical criteria.  $n_0 \ll n_i$  in order to avoid a possible initial overlap.  $\alpha = 0.001$  provides a wide spacial distribution ( $\sim 120$  sites) to correctly simulate the scattering of a “plane wave” with a well defined  $k$ . In Fig.4.7(a) we show results for three different values of  $U_0$ . The agreement between the theoretical  $t$  (lines) and direct numerical simulations (symbols) is excellent. This result validates our theory and provides a good support for observing this phenomenon in real experimental setups. Below the critical amplitude  $U_0 = 1$ , no resonance exist because no local mode can be excited. The transmission profile is similar to the one found for the scattering of a plane wave against a linear impurity ( $U_0 = 0$ ) [150]. For  $U_0 > 1$ , the observation

of Fano resonances is allowed. However, the stability of the nonlinear mode should also be considered. A small-amplitude plane wave can be viewed as a linear perturbation, therefore the localized solution has to be stable in order to numerically (and experimentally) observe the resonance. For  $U_0 = 1.36$ , the red theoretical curve matches perfectly the numerical one (diamonds) where the unstaggered solution is stable. Stability is an extra condition that should be fulfilled (for nonlinear cubic impurities[21], the nonlinear localized mode is always stable). Finally, for large amplitudes no resonances are possible, because  $\omega_{cc}$  lies outside the band. The NLM grows in power and becomes an effective wall for the plane wave. Therefore, total absence of transmission is expected for large  $U_0$ .

Finally, for a fixed  $U_0 = 1.36$  we construct the output profile for different angles [see Fig.4.7(b)]. For small  $k$ -values, the transmission is very high achieving its maximum ( $t = 1$ ) around  $\pi/8$ . As  $k$  is increased, the transmission and reflection coefficients becomes of the same order of magnitude. For  $k > \pi/4$ , most of the energy is reflected, becoming a maximum exactly at the Fano resonance, where no transmitted light is observed.

In conclusion, we proposed a new possible setup for observing Fano resonances in optical waveguide arrays. We found a very good agreement between theory and numerical simulations showing that, in principle, this phenomenon could be observed in current experiments.

## 5. Disorder

### 5.1. Anderson localization

The original concept of Anderson localization assumes a periodic structure where disorder is introduced via a random change of the local properties at each site of the lattice, leading to wave localization due to interference between multiple scattering paths [24]. Although it was first described in the context of condensed matter [24, 25], there are now examples in many other fields: Acoustics [28], microwaves [29], Bose-Einstein condensates [31] and optics [118]-[122], to name a few. This problem assumes, in general, a linear 1D Hamiltonian system plus disorder,

$$H = \sum_n [\epsilon_n |u_n|^2 + C_n u_n u_{n+1}^* + C_n u_{n+1} u_n^*].$$

In 1D and 2D all Eigenstates are exponentially localized ( $e^{-\xi n}$ ) within the localization length " $\xi$ ". For diagonal (on-site) disorder in the propagation constant  $\epsilon_n \in [-\frac{W}{2}, \frac{W}{2}]$  (i.e., "site energy" in the quantum mechanical context), an upper bound of the localization length is given by  $\xi \simeq 96C^2/W^2$ , as was shown in [124]. But what happens for weak disorder, when the localization length grows so much, that it is no longer observable in experiments. And what happens, when furthermore

nonlinearity comes into the mix?

Recently, optical waveguide lattices [3] have emerged as ideal systems to study the interplay of disorder and nonlinearity in simple table-top experiments. After a first experimental study of wave evolution in a disordered nonlinear fiber array [140], the averaging of multiple individual realizations of disorder was introduced [121] as a fundamental concept, resulting in the first-time-ever experimental demonstration of genuine Anderson-localization, i.e. exponentially localized modes. Furthermore, in the optical domain it was proven in experiment and theory that a random displacement of the inter-guide distance (off-diagonal disorder) also shows exponential localization similar to the results when changing the local properties (propagation constants) of the individual sites [123, 125].

## 5.2. Disorder in finite nonlinear arrays

When a weak nonlinearity is added to the disordered system, it has been predicted that the nonlinearity will either promote or inhibit the wave packet spreading, depending on the systems details and the relative strength of disorder and nonlinearity [133]-[139]. The problem of wave packet spreading under the impact of disorder and nonlinearity was studied by several authors (see, e.g., Ref. [141] and references therein), who tried to observe the asymptotic behavior of the wave-packet by employing extremely long evolution scales and very large lattices, observing the breakdown of complete localization. However, these studies are detached from currently realistic experimental setups and possible applications [32]. Nevertheless, it is a general con-

sensus that a (stronger) focusing nonlinearity will facilitate localization [2], what was also shown experimentally in [121]. Whereas this work was performed in a 2D system, in a subsequent experiment [122] the impact of nonlinearity on localization, in a 1D system, was experimentally analyzed, culminating in the same result: focusing nonlinearity indeed enhances localization of propagating waves. Thus, a general picture of the effects of the interplay between disorder and nonlinearity remains unclear. Interestingly, very recently disorder-induced transport enhancement was demonstrated in a photonic quasicrystal [142]. In such systems, the fractal band-structure in the ordered system is “smoothened” by disorder, which results in an increased spreading of the evolving wave packet. However, it is important to note that such a system is fundamentally different from common 1D and 2D lattices where the band structure is smooth when disorder is absent (i.e., the second derivatives on the band exist).

We will show, that an increase of disorder can result in the smoothing of the light distribution for an initially localized excitation. This effect is even further facilitated by a focusing nonlinearity. We focus on realistic systems and lattices at a finite propagation length, where the dynamical evolution is bound and the system dimensions can be smaller than the localization length. Hence, we aim to identify generic properties of nonlinear disordered lattice systems in the first stages of their evolution.

We find a clear transition between weakly and strongly disordered systems.

The light evolution is again modeled by a set of normalized DNLS equations:

$$-i \frac{du_{\mathbf{n}}}{dz} = \epsilon_{\mathbf{n}} u_{\mathbf{n}} + \sum_{\mathbf{m}} C_{\mathbf{n},\mathbf{m}} u_{\mathbf{m}} + |u_{\mathbf{n}}|^2 u_{\mathbf{n}}. \quad (5.1)$$

The coordinate  $\mathbf{n}$  depends on the dimension and lattice type [for example,  $\mathbf{n} = (k, l)$  .

in a 2D square lattice]. The quantity  $\epsilon_{\mathbf{n}}$  is the propagation constant (i.e., “site energy” in the quantum mechanical context) of the  $\mathbf{n}$ -th guide. The hopping between adjacent lattice sites  $\mathbf{n}$  and  $\mathbf{m}$  is described by the coupling constant  $C_{\mathbf{n},\mathbf{m}}$ . In our model we impose disorder on both, the propagation constant [ $\epsilon_{\mathbf{n}} \in \{-W_\epsilon/2, W_\epsilon/2\}$ ] and the coupling constants [ $C_{\mathbf{n},\mathbf{m}} \in 1 + \{-W_c/2, W_c/2\}$ ]; the disorder is thereby characterized by the disorder strengths  $W_\epsilon$  and  $W_c$ , respectively. Note that we limited  $W_c$  to the interval  $\{0, 2\}$ , to assure that the inter-site coupling is always positive. A simulation of light propagation in a waveguide array is shown in Fig. 5.1(a).

One of the most useful measures used for the description of localization phenomena in finite systems is the participation ratio (PR) [142] that is measured after a fixed propagation distance and yielding a rough estimate of the number of sites that are occupied by the wave packet [see eq. (2.39)], i.e., where the light has a significant amplitude at the output facet of the sample. As pointed out in [142], in order to get meaningful data for finite lattices, one has to average over  $k$  different realizations of disorder, requiring also an averaged PR:  $R = \left\langle \sum_{\mathbf{n}=1}^N |u_{\mathbf{n}}|^4 / P^2 \right\rangle^{-1}$  [143]. The quantity  $P$  is the total optical power evolving in the system, and  $N$  is the total number of lattice sites.

We start our analysis by carrying out extended numerical simulations in 1D lattices, using Eq. (5.1) In our theoretical analysis, we numerically integrate Eq. (5.1), considering multiple random realizations and performing an averaging process for the relevant quantities. In the 1D case, we use  $N = 81$  waveguides with an initially localized excitation:  $u_n(0) = \sqrt{P}\delta_{n,n_c}$ , where  $n_c$  corresponds to the input position.

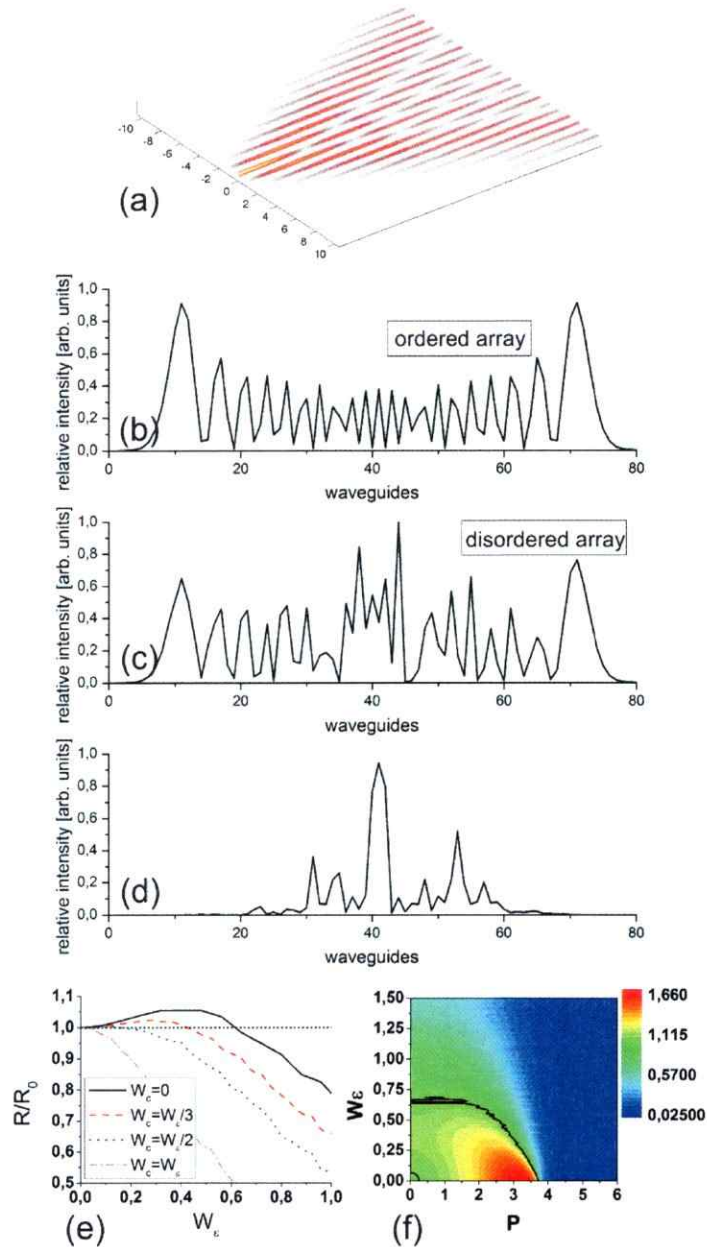


**Figure 5.1.:** (a) Sketch of the light propagation in a 1D waveguide array, when only one waveguide is excited. (b)-(d) Simulated intensity distribution in the lattice sites for ordered (b), single realization of on-site disorder degree  $W_\epsilon = 0.36$  (c) and  $W_\epsilon = 1$  (d) after propagation through the waveguide array when only the central waveguide is excited. (e) Simulated averaged PR  $R$  vs. on-site disorder for different levels of inter-site disorder after linear (low power) propagation. (f) Simulated averaged PR vs. Power  $P$  and onsite-disorder  $W_\epsilon$  after nonlinear propagation (black contour denotes  $R = R_0$ ). In all cases, the PR is normalized to  $R_0 \equiv R(W_\epsilon = 0)$ .



The participation ratio was taken at the propagation distance  $z_{max} = N/4$  (in normalized units). In order to simulate linear propagation, the total optical power  $P$  is chosen very small ( $< 0.01$ ). In order to recapitulate Anderson's results [24], we show in Fig. 5.1(b)-(d) output distributions for the ordered lattice and two levels of pure on-site disorder, showing a ballistic spreading for the ordered ( $W_\epsilon = 0$ ) case [Fig. 5.1(b)]. The diffraction pattern exhibits distinct side lobes and small amplitudes around the initially excited central site. When weak disorder is introduced [ $W_\epsilon = 0.36$ , Fig. 5.1(c)], the part of the power contained in these lobes is redistributed to the waveguides close to the center. By increasing the disorder further, a localization around the excited site is observed, with exponentially decreasing tails on both sides [Fig. 5.1(d)]. However, an important aspect hereby is the occupation of the individual lattice sites, that defines the PR, i.e. the effective width of the diffraction pattern. Our simulations reveal something very surprising: As the (weak) disorder strength is increased, the average PR increases too [black solid line in Fig. 5.1(e)], although the second moment decreases [144]. Upon further increment of the disorder, the spatial profile reduces its expansion and the PR decreases henceforth. The figure shows a clear maximum of the number of excited sites which separates regimes of expansion and localization [144].

Additionally, we investigated how mixed disorder influences the light propagation by increasing the amount of inter-site disorder  $W_c$ . The results for  $W_c = W_\epsilon/3$ ,  $W_\epsilon/2$ , and  $W_\epsilon$ , are shown in Fig. 5.1(f) as the red dashed line, the blue dotted line, and the pink dash-dotted line, respectively. From our simulations it is evident that, as the inter-site disorder increases, the initial growth of the PR is reduced, and eventually

vanishes (i.e.  $R/R_0 < 1$  for all disorder levels) for sufficiently high inter-site disorder. In a next step, we analyzed the impact of nonlinearity, i.e. the propagation of high-power light fields. A focusing nonlinear term in Eq.(5.1) facilitates the self-focusing of the excitation around the initially excited site [145]. Therefore we find in the weak-disorder regime the increase of the PR is enhanced in the presence of a small amount of nonlinearity. Figure 5.1(e) shows the average participation ratio of the profile after propagating a defined distance in the presence of on-site disorder  $W_e$  and power (nonlinearity)  $P$  in a 1D lattice. For  $P \approx 0$ , we find an increasing PR for weak disorder. Switching off the disorder and consider only nonlinearity, the picture is similar: the PR increases up to some maximum value due to redistribution of the power in the waveguides and then drops as the wave packet localizes [146]. Therefore, for  $P < 4$  nonlinearity may facilitate the delocalization process. Below the critical nonlinearity  $P < 4$  for 1D lattices there is a mixture of localization induced by disorder and nonlinear, resulting in a higher number of excited sites. This causes an increase of the PR with the maximum shifted to smaller values of the disorder strength.

During my visit in Jena in 2011, our experiments are carried out in fs-laser written waveguide arrays (see App. C ). For the analysis of 1D samples, we fabricated several arrays with  $N = 81$  sites each: One without disorder, and nine with varying degrees of disorder (and 30 realizations for each degree of disorder). Disorder was introduced by varying the spacing between the guide centers:  $d = (23 \pm \delta_d)[\mu\text{m}]$ ,  $\delta_d = (0, 0.25, 0.5, 0.75, 1, 1.5, 2, 3, 4, 6)$ . The difference in overlap of the individual waveguide modes additionally creates a statistic detuning of the guides and, there-

fore, an on-site disorder besides the inter-site disorder. An input-beam at  $\lambda = 800$  nm from a Ti:Sapphire laser was launched into a single waveguide in the center of the array using a standard microscope objective. At the end facet of the sample, the intensity patterns were recorded using a CCD camera. Whereas the linear regime ( $P_{lin}$ ) was measured by using the continuous wave-mode of the laser (i.e., the laser power was only a few mW), the nonlinear regime was studied in the pulsed regime with pulse peak power of  $P_{nl1} \simeq 1\text{MW}$  and  $P_{nl2} \simeq 2.7\text{MW}$ . The participation number  $R$  was computed for all the different settings, including its standard deviation, and normalized to the value of the linear single-site excitation of an ordered array ( $R_{ino}$ ). Our numerical predictions are confirmed by our experimental results, summarized in Fig. 5.2. A microscope image of the front facet of an ordered and a disordered 1D lattice is shown in Fig. 5.2(a). Fig. 5.2(b) shows different propagation patterns of an ordered array (upper row), a single disordered realization (middle row), and an averaged output profile for the same disorder level (lower row). From each realization, the PR was computed and then averaged. As it can be clearly seen from our experimental data [see Fig. 5.2(c)], in the linear regime, we indeed observe the delocalization tendency with the increase of weak disorder and a diffusion-peak at a disorder level of  $\delta_d = 1.5 \mu\text{m}$  spacing variation between the guides. When non-linearity comes into play, the diffusion-peak shifts towards smaller disorder levels, and additionally maximum significantly increases. However, the delocalization is only observed for sufficiently small nonlinearities. If the nonlinearity is too high, the smoothing effect vanishes as the self-focusing is sufficiently strong to inhibit any diffusion/expansion process.

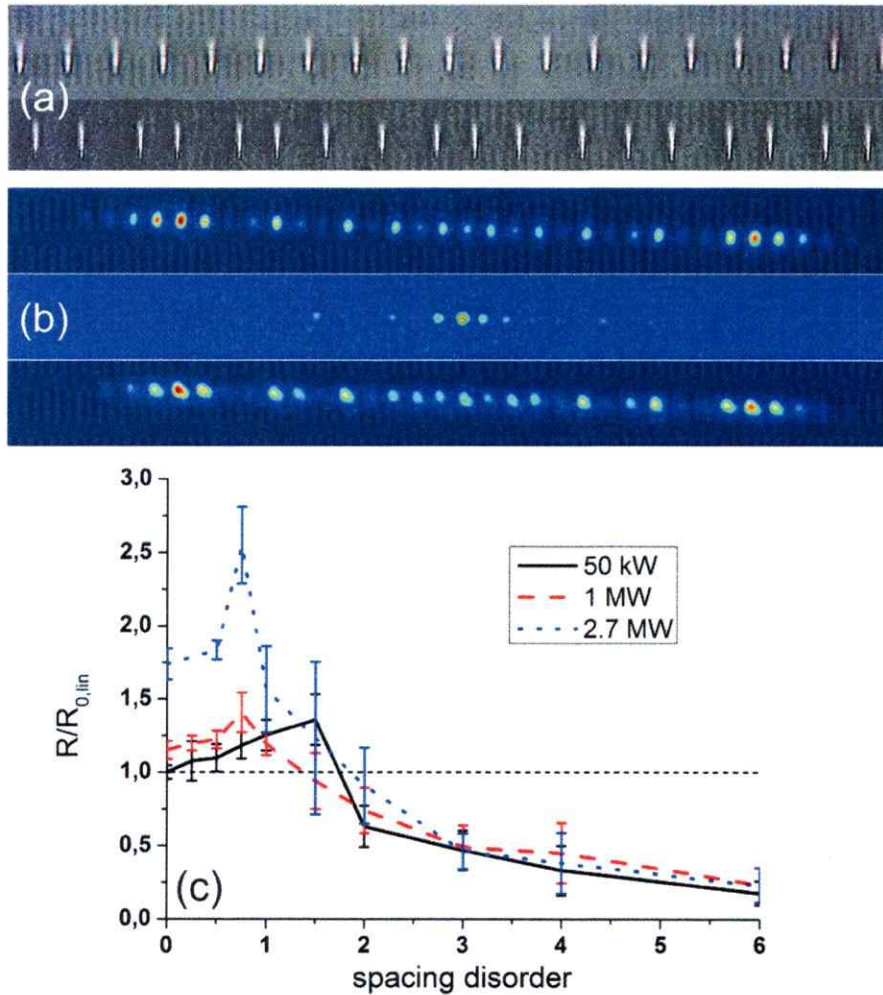


**Figure 5.2.:** (a) Microscopic images of an ordered (top) and disordered (bottom) 1D array. (b) Experimental intensity output patterns. Upper row: ordered array; middle row: single realization disordered array; bottom row: averaged disordered output pattern. (c) Experimental PR  $R$  versus disorder strengths for different levels of input power.

In 2D waveguide arrays, various different settings are possible that have a different impact on the localization/delocalization behavior of the propagation wave packet. One of the simplest 2D structures is the square lattice where each lattice site is coupled to four nearest-neighbors only. Hence, in the ordered linear case, a square

lattice constitutes a "superposition" of two perpendicular 1D arrays. A microscope image of a square waveguide lattice is shown in Fig. 5.3(a), and an experimental output intensity pattern of such a structure is shown in Fig. 5.3(b). After exciting a single waveguide at the center of the structure, the diffraction pattern exhibits four distinct side lobes. Similar to the 1D system, when on-site disorder is introduced in model (5.1), an increase of the PR is found [see Fig. 5.3(c)]. When additionally inter-site disorder is introduced, at some point the diffusion-peak vanishes and localization is observed for all disorder levels.

For the experimental analysis of the 2D square sample, we fabricated lattices with  $21 \times 21$  sites with three different levels of disorder and one ordered array. The mean distances  $d_{hor} = (17 \pm \delta_h)[\mu m]$  with  $\delta_h = (0, 2, 4, 6)$ . Although the vertical distance was kept fixed at  $d_v = 23[\mu m]$ , this setting is equivalent to a 2D fully disordered lattice [149].

These theoretical considerations are fully proven by our experimental results, which are summarized in Fig. 5.3(d). For small inter-site disorder the PR significantly grows, and for further increase of the disorder the PR drops, resulting in localization of the wave packet (black solid line). Importantly, distinct side lobes in the diffraction pattern only occur when a single waveguide is excited [2, 3]; wide Gaussian beams create a homogeneous Gaussian shaped propagation pattern. Such a pattern continuously narrows for increasing disorder. In the experiments we used a Gaussian beam that covers approximately 9 sites. We clearly see that there is no delocalization enhancement for such initial condition [Fig. 5.3(d), red dashed line]. As for pure inter-site disorder no diffusion-peak is observed in our simulations, we therefore

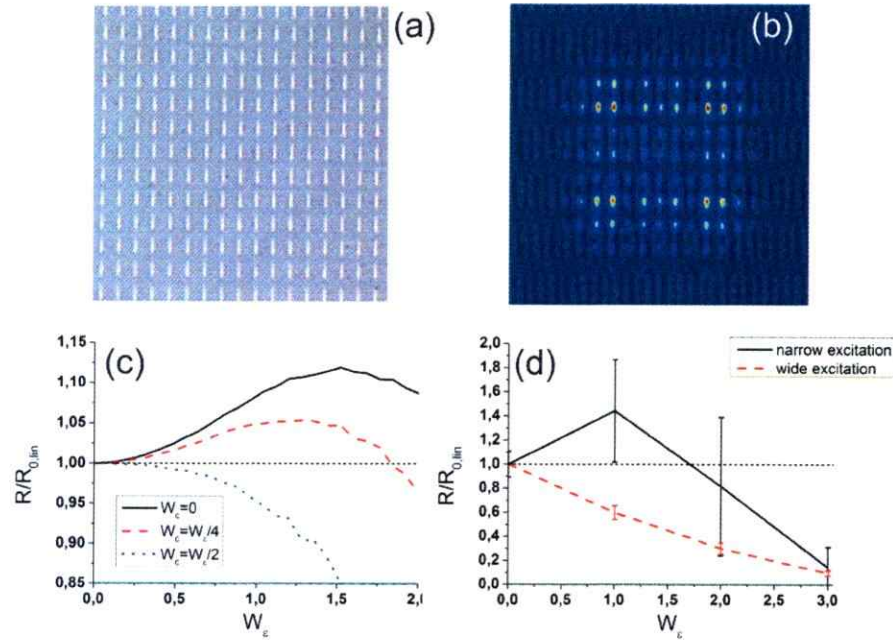


**Figure 5.3.:** (a) Microscope image of the fabricated ordered square lattice. (b) Corresponding averaged output intensity profile. (c) Numerical simulation of the PR for different mixed disorder:  $W_c = 0$  (black solid line),  $W_c = W_\epsilon/4$  (red dashed line),  $W_c = W_\epsilon/2$  (blue dotted line). (d) Experimental results for single-site (black solid line) and gaussian (red dashed line) input excitations, averaged over 25 realizations. All data is normalized to the ordered array  $R_0$ .

conclude that the variation of the inter-site spacing results in a mixed disorder in the fabricated samples.

Another example of 2D arrays are the hexagonal lattices, where each site is coupled to six nearest-neighbors. Its band structure is very different to the one found in the square-lattice. Additionally, the diffraction pattern of a delta-like input beam does not exhibit the distinctive outer lobes that were characteristic for the square lattice. A typical diffraction pattern of such a structure is shown in Fig. 5.4(a). Adding disorder only leads to an increased localization, as shown in Fig. 5.4(b), which matches the experimental results reported in Ref. [121].

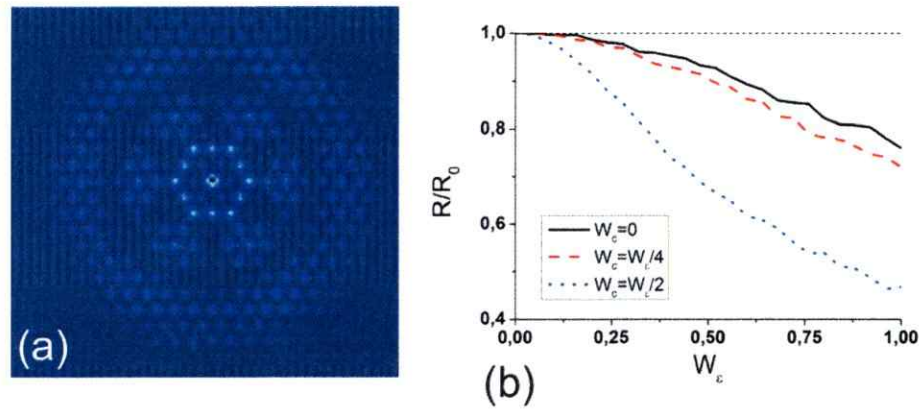


**Figure 5.4.:** (a) Numerical output intensity pattern for an hexagonal lattice. (b) Numerical simulation of the PR for different mixed disorder:  $W_c = 0$  (black solid line),  $W_c = W_c/4$  (red dashed line),  $W_c = W_c/2$  (blue dotted line). The data is normalized to the ordered array  $R_0$ .

Most explanations concerning diffusion and expansion processes in disordered lattices resort to band structure changes. However, the reduction of the pseudo-gaps in a disordered lattice [142] does not necessarily imply that a particular excitation located at any input position will be able to excite more states. Even if this were so, it is not clear that more excited states will give rise to a better expansion or the distribution of the power of the wave packet. The excitation of the “correct”, i.e., well delocalized eigenstates, is probably more relevant. For weak disorder it is not possible to claim that, by considering a single-site excitation, a particular state will get excited; this may be only possible for strong disorder when all linearstates are very localized. Therefore, in our view it is not useful to discuss a precise excitation of states, as this would be certainly a matter of probability [32] and it will not correspond to a representative case.

Instead, we use a different approach to validate our observations based on simple

dynamical arguments. A wave packet initially localized in a single waveguide can be decomposed into a superposition of plane waves, each one with a different transverse velocity. In the absence of disorder, during propagation this wave packet will form the typical side lobes of the diffraction pattern [2, 3] where the waves possess a high transverse velocity, and most of the propagating power is concentrated in these lobes. For weak disorder one can assume that launching light into a single waveguide excites a number of different linear modes with different transverse velocities. Therefore, the main lobes still propagate without strong distortions as those plane waves possess sufficient kinetic energy to overcome the disordered potential wells and to move across the lattice. However, some waves with less kinetic energy will get trapped in the impurity regions of the particular disorder distribution. As a consequence, the wave will expand more homogeneously, localizing energy in the input region (small velocity waves), in the lobes (high velocity waves), and in between (intermediate velocities). When the disorder is further increased, also the waves in the side lobes will get trapped as their energy becomes comparable to the deeper disordered potential wells. Therefore, light reduces its expansion and the localization starts to dominate the picture (see Fig. 5.1 and Refs. [140, 121, 122]). In this vein, the PR will increase at small disorder strength and decrease only at sufficiently high disorder. It is important to clarify that this process does not have implications in the *edge-to-edge-diameter* of the wave packet; it rather implies a smoother distribution of the light and therefore a higher PR. As the side lobes remain the dominating feature of the propagation pattern even in the far field [147], the effect reported here is not connected to the initial diffusive spreading at short propagation distances [148]. At



low disorder strengths, the distribution of energy across the lattice is dominated by the side lobes, as they can be found in various lattices such as 1D, 2D square and honeycomb, and 3D lattices - all of these structures will therefore exhibit the initial increase of the PR for small disorder and, therefore, a diffusion-peak.

Assuming a disorder level in the vicinity of the maximum of PR, adding a weak nonlinearity will increase the (random) refractive index at each site, in an amount proportional to the light intensity on the site. This causes the high-intensity side lobes to be affected the most, whereas the 'slow' waves in the center are not affected much. However, the latter are already localized, as their energy content is insufficient to overcome the disordered potential wells. Thus, the nonlinear deepening of the random potential wells, renormalizes the disorder strength of the individual lattice sites. This, in turn, causes the increment of the participation ratio to be higher and to occur at smaller values of disorder strength than in the linear case, in agreement with our experimental and numerical results.

An exception is found in the triangular (hexagonal) lattice that, due to the high number of next-neighbors (6), possesses an unusual discrete diffraction pattern with no distinct lobes, resembling the diffraction pattern of a continuous medium. Thus, for the triangular lattice no enhancement of the PR, even at weak disorder, is found, in agreement with the experimental findings reported in [121].

Our results, that hold in any periodic system that is described by our model, shed new light on the old question how disorder and nonlinearity impact the evolution of wave packets. We claim that these results may hold for any lattice that, in the absence of disorder and/or nonlinearity, presents clear signatures of discrete diffraction.

### 5.3. Influence of a disordered boundary

In rough or corrugated channels, the phenomenon of Anderson localization is connected to the transmission of electrons or optical pulses. In these systems, the channel surface is disordered along the propagation direction. Theoretical studies showed transitions between diffusive and localized regimes [126]-[128]. Transport behavior was also considered in [129]-[131], where multiple scattering from longitudinal surface roughness caused localization of waves, although regimes of coexistence between ballistic, diffusive and localized transport, depending on the symmetry of the corrugation profile, have been predicted [132].

Recently, a different kind of “corrugated waveguide” was considered theoretically [33]. Here the disorder is only in the transverse direction, and does not change along the direction of propagation. Also, the optical medium in the bulk, away from the corrugated surface, possesses a periodic index of refraction along the two transverse directions. The disorder is imposed on the boundary by random displacement. Despite the weak disorder, a light beam still tends to localize in the center of such a system far from the boundary.

Let us consider a 2D rectangular  $N \times M$  waveguide array (Fig.5.5). The linear evolution equations for the mode amplitudes  $u_{\mathbf{n}}$  are

$$\sum_{j=p\pm 1} C_{v_j} u_{j,q} + \sum_{j=q\pm 1} C_{h_j} u_{p,j} = -i \frac{du_{pq}}{dz}, \quad (5.2)$$

where  $\mathbf{n} = (p, q)$  denotes the position of the guide center.  $C_{v,h}$  are the coupling coefficients between nearest-neighbors guides. They decay exponentially with the mutual distance between the guides. To keep our approach general, we assume anisotropic

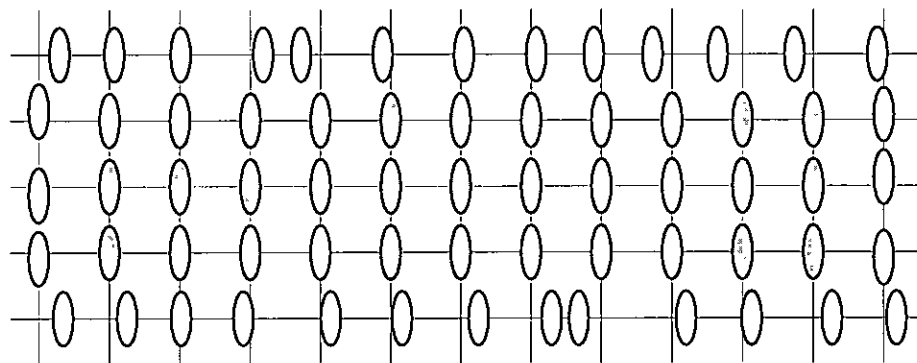


**Figure 5.5.:** Scheme of a finite two-dimensional coupled array of elliptical waveguides with disordered boundary.

coupling in the horizontal and vertical direction. At the boundary of the array, randomness is introduced by displacing the guides from their (ordered) positions, along the boundary surface. This creates random couplings among the boundary guides, for the horizontal coupling  $C_h \rightarrow C_h e^{-\omega_h \Delta}$  as well as for the vertical coupling  $C_v \rightarrow C_v e^{-\omega_v \Delta}$ . The quantity  $\Delta$  is a random number in  $[-1, 1]$  and the randomness strengths  $\omega_h$  and  $\omega_v$  along the horizontal and vertical boundaries respectively are different due to the ellipticity of the guides. The bulk, that represents the ordered part of the array, is connected to the disordered boundary layer with coupling values computed from the mean pythagorean distance. These conditions are close to the possibilities of experimental realization [125].

First, in order to illustrate the localization mechanisms in the system under consideration, we analyze a waveguide array with  $13 \times 5$  waveguides and disordered boundary and perform a direct numerical integration of Eq.(5.2) with a single-site excitation at the array center  $(n_c, m_c) = (7, 3)$ . The parameters chosen for the simulation of the disordered case (left column of Fig. 5.6) are:  $C_h = 2$ ,  $C_v = 1.7$ ,

$\omega_h = 11/28$ ,  $\omega_v = 4/17$  [103]. For comparison, we compute the evolution of the ordered case and its pure discrete diffraction (right column of Fig. 5.6). For small propagation distances ( $z \simeq 5$ ), both systems show discrete diffraction with maxima at the outer lobes. The amplitude of the initially excited site decreases steadily with  $z$ . However, after a transition distance of  $z_t \simeq 10$ , that is necessary for a complete backscattering cycle, the influence of the boundary layer becomes apparent. In the boundary-disordered case, for  $z > 10$ , the amplitude of the center site is non-vanishing for all propagation lengths. It continues to oscillate with  $z$ , but finally saturates to a nearly stationary mode, showing the persistence and stability of localization due to the disordered boundary. The main difference to the case of a completely disordered system (bulk + surface) is that the initial oscillations due to discrete diffraction are stronger. In addition, simulations done for unsymmetrical excitations, also show localization at the initial excited waveguide.

We prepared 30 disordered-boundary waveguide arrays with a length of 101 mm with  $N \times M = 13 \times 5$  waveguides each. The inter-guide separation in the ordered bulk, which is also the mean separation at the (disordered) boundary, was of  $14 \mu\text{m}$  and  $17 \mu\text{m}$ , along the horizontal and vertical directions, respectively. Disorder in the waveguide spacing was induced by varying the inter-guide distance:  $d_h = 14 \pm 5.5\Delta \mu\text{m}$  and  $d_v = 17 \pm 4\Delta \mu\text{m}$ , with  $\Delta \in [-1, 1]$  randomly equally distributed.

In each array the individual central waveguide was excited using a Ti:Sapphire laser system at low input power to ensure linear propagation. At the end facet, the intensity patterns were recorded with a CCD camera. For the observation of localization a wavelength of 840 nm was used, corresponding to coupling coefficients [103] of

$$C_h(C_v) \simeq 2.2(1.8) \text{ cm}^{-1}.$$

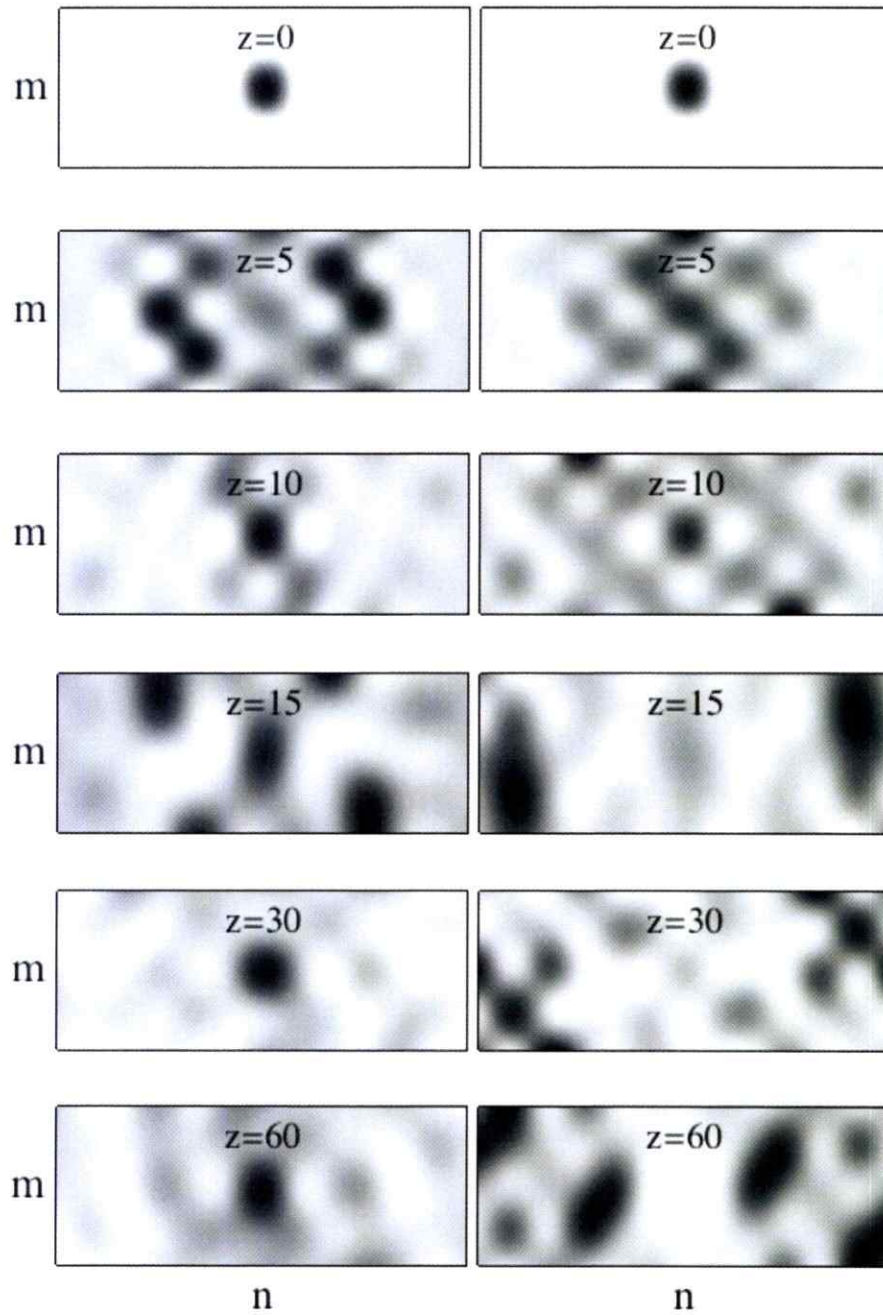


**Figure 5.6.:** Comparison between simulations of the disordered boundary waveguide array of Eq.(5.2) (left column) with  $C_\alpha = 2$ ,  $C_\beta = 1.7$ ,  $\omega_\alpha = 11/28$ ,  $\omega_\beta = 4/17$ , averaged over 100 realizations and an ordered  $13 \times 5$  array (right column)

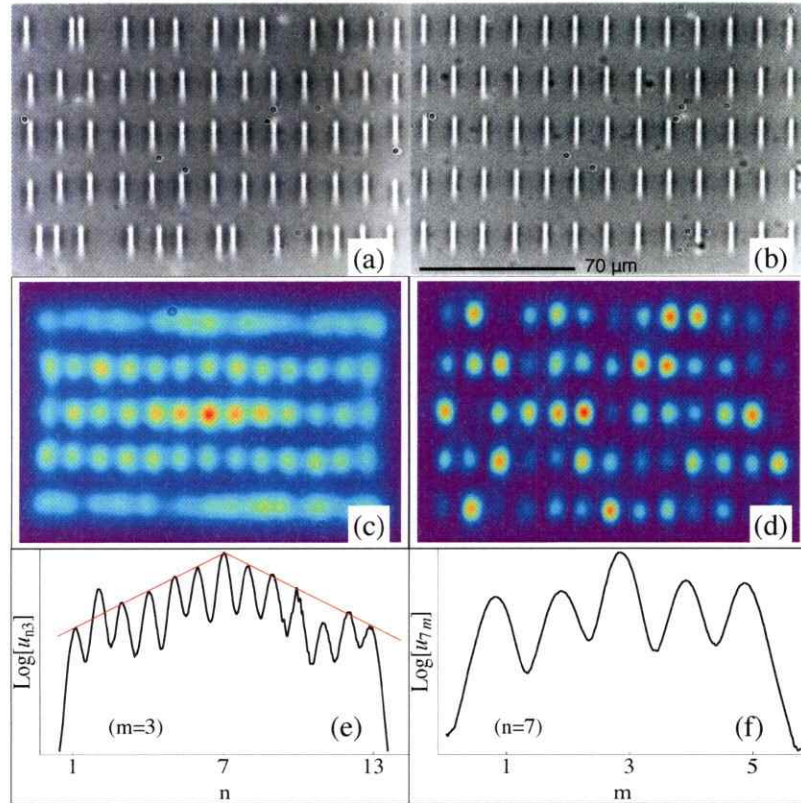


**Figure 5.7.:** Experimental results for the  $13 \times 5$  arrays: (a) Microscope image of one configuration of boundary-disordered, (b) ordered array, (c) mean output of 30 realizations of the boundary-disordered waveguide array,  $\lambda = 840 \text{ nm}$  (d) output of the ordered array, (e), (f) logarithmic plots of  $|u_{n,c}|$ ,  $|u_{n,c,m}|$ .

The experimental results, shown in Fig. 5.7, demonstrate a clear localization tendency around the position of the input beam. A microscopic image of a single realization of the  $13 \times 5$  boundary-disordered array is shown in Fig. 5.7(a), where the ordered center as well as the boundary layer with disordered spacing can be seen. For comparison we also show a microscopic image of the completely ordered  $13 \times 5$  waveguide array. In Fig. 5.7(c), the mean output intensity of 30 realizations is shown, where localization on the central input site is clearly observed. When comparing with the intensity distribution in an ordered array [Fig. 5.7(d)] we find

that the propagation distance is sufficiently long for complete delocalization in the ordered case. Thus, the observed localization effects can be attributed to the disordered boundary layer. The stronger coupling obtained in the  $13 \times 5$  array due to the longer wavelength leads to exponential localization in both coupling directions, shown in Figs. 5.7(e) and 5.7(f).

In summary, we have shown both, numerically and experimentally that the presence of weak disorder can lead to a smoothing of the light distribution for an initially localized optical beam in 1D and 2D waveguide arrays. Moreover, the addition of focusing nonlinearity facilitates the smoother spreading even further. The regions separating enhanced spreading (weak disorder) and localization (strong disorder) can be clearly identified and the general behavior can be explained by dynamical arguments.

Furthermore, we have investigated experimentally the influence of a disordered boundary in a finite 2D coupled waveguide array and found asymptotic partial localization of the wave packet in the center of the bulk region far away from the boundary. The presence of a disordered boundary can give rise to Anderson localization in regions away from the boundary. This result may be extrapolated to larger finite lattices, if one allows for a sufficiently long propagation distance.

## 6. Mobility

Mobility of localized solutions in nonlinear cubic waveguide arrays (WAs) is a well studied area. As far as the power stays low in an 1d system, the energy barrier imposed by the discreteness and the nonlinearity (usually called Peierls-Nabarro (PN) potential [39]) will stay small and solutions will move across the lattice by just giving them a judicious kick [151, 152]. For larger powers, the energy barrier grows and mobility is not possible anymore. In 2d, there is no mobility to be found at all. However, a particularly interesting property of the one-dimensional (1D) s-DNLS model [40]-[46] is the existence of certain “sliding velocities”, where localized discrete solitons may travel in the lattice without radiation. This behavior was connected to the existence of “transparent points” associated with the vanishing of a PN potential barrier, usually defined as the difference in energy (Hamiltonian) at constant power (norm) between the two fundamental localized stationary solutions centered at one site (odd mode) and symmetrically in between two sites (even mode). Close to the points of vanishing of this energy difference are regions of stability exchange between the even and odd solutions, associated in general with the appearance of a family of intermediate, asymmetric stationary solutions [47], connecting both types of



symmetric solutions at the bifurcation points [48]. The *effective* energy barrier caused by this intermediate solutions (IS) will strongly depend on them. The existence of regimes of enhanced mobility close to such bifurcation points is also well-known from studies of other one-dimensional lattice models [48, 153, 68]. In general d-dimensional lattice the s-DNLS is given by

$$i \frac{du_{\vec{n}}}{dz} + \sum_{\vec{m}} u_{\vec{m}} - \gamma \frac{u_{\vec{n}}}{1 + |u_{\vec{n}}|^2} = 0, \quad (6.1)$$

as usual  $u_{\vec{n}}$  represents the light amplitude at site  $\vec{n}$ ,  $\gamma$  the strength of the nonlinearity with respect to the coupling coefficient, and  $z$  a normalized propagation distance along the waveguides. The coupling to neighboring sites  $\vec{m}$  is represented by the sum. We use stationary solutions according to the definition (2.33) and obtain the same linear behavior as in Sec. 2.3: Small-amplitude plane waves in a d-dimensional system define the band  $\lambda \in [-2d - \gamma, 2d - \gamma]$ , while high-amplitude plane waves define a second band  $\lambda \in [-2d, 2d]$ . Therefore in-phase stationary localized solutions are limited to exist in the region  $\lambda \in [2d - \gamma, 2d]$ , bifurcating from the fundamental modes of those bands [47]. We remember the (6.1) two dynamically conserved quantities, the Hamiltonian (eq. 2.36) and the optical power (eq. 2.34).

### 6.1. 1D systems

It was shown in Ref. [40] that there exist points where the fundamental solution's energies coincide, what was interpreted as vanishing points of the PN barrier. Contrary to what is expected, the fundamental solutions remain immobile in these points. In order to achieve a good mobility it is necessary to increase the amount of power

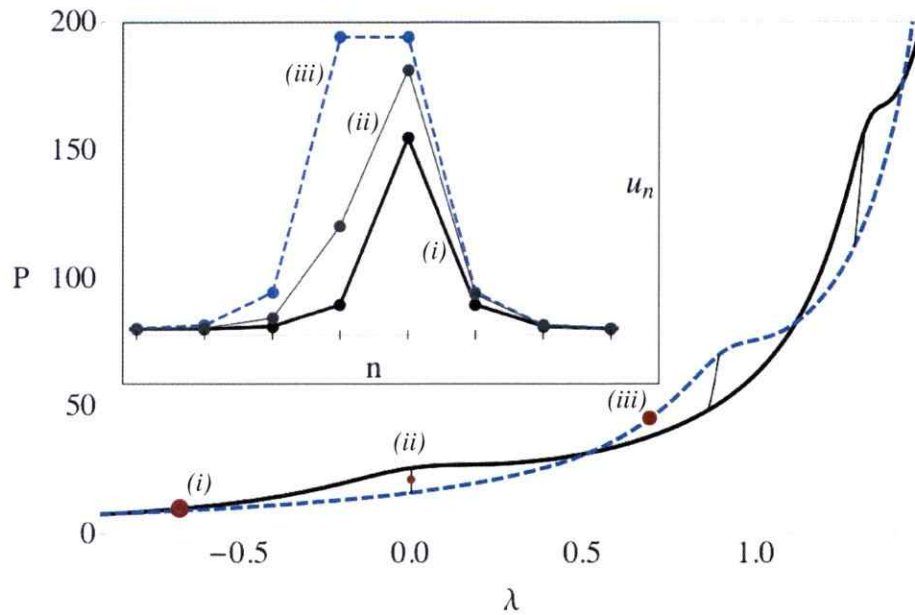


**Figure 6.1.:**  $P$  versus  $\lambda$  for odd, even, and intermediate solutions in full, dashed, and thin lines, respectively.

Inset: profiles corresponding to filled circles.

up to the bifurcation point where the IS disappears, which were not known at this moment. A constraint method [97, 98] (see section 3.2) can be used to identify the ISs and describe a pseudo-potential landscape among all stationary modes.

In the following, we discuss these properties for  $\gamma = 10$  (focusing nonlinearity). A different  $\gamma$  will produce different curves but the main saturable phenomenology will be preserved. Localized solutions are computed by using a standard Newton-Raphson method. Fig. 6.1 shows a power versus frequency diagram for both fundamental modes - the odd and the even solutions - including the IS. As expected, the IS corresponds to a non-symmetric profile connecting the two fundamental modes [see Fig. 6.1-inset]. The two fundamental solutions cross each other - repeatedly - as  $P$  increases. In regions where  $|P_{odd} - P_{even}|$  is large, a family of IS appears. It is remarkable that all the ISs of the first family have  $\lambda = 0$  and connect both (even and

odd) modes for this value. In such a situation, Eq.(6.1) corresponds to the integrable Ablowitz-Ladik equation [45], which has an analytic mobile solution. However, in the physical s-DNLS model, it is not expected to find radiationless travelling solutions, since mobile modes require to have the same power and not the same frequency. We perform a standard linear stability analysis (see Sec. 3.1) by computing the largest unstable eigenvalue of the linearized spectrum, denoted as " $g$ ". Fig. 6.2(a) shows our results where  $g = 0$  implies stable solutions and  $g > 0$  unstable ones. For all regions where the fundamental solutions are simultaneously stable (three regions in this plot, but infinite when  $P \rightarrow \infty$ ), the unstable IS appears. In these regions there are points where the energy of both fundamental solutions is exactly the same [see inset in Fig. 6.2(a) for the first bistable region ( $P \sim 20$ )]. However, the effective energy barrier is not zero if the IS is considered as well. In Fig. 6.2(b) we plot  $\Delta H_0 \equiv |H_{odd} - H_{even}|$  and  $\Delta H \equiv |H_{max} - H_{min}|$  versus power. For the first two "bistable" regions, we clearly see that  $\Delta H_0$  goes to zero as it was previously predicted in Ref. [40]. However, when we consider the energy barrier the solution really experiences ( i.e.  $\Delta H$  ), there is always a nonzero barrier to overcome in order to move a localized solution across the lattice. In fact, this barrier can be very small but it is - strictly speaking - nonzero. A first guess could be, that the most favorable region for mobility would be the one where  $\Delta H$  is a minima. However, this is not the case for stationary solutions. If we kick an odd or even mode, we are putting in motion an immobile-defined solution, therefore there is always radiation from tails. As a consequence, the power of the moving solution is lower than the initial one. So, if we initially take the solution where  $\Delta H$  is a minima ( $P_m$ ), the effective barrier will

increase [see Fig. 6.2(b)]. A better option would be the one where  $P > P_m$  where, due to radiation, the power and the effective barrier decrease. Now, in order to go deeper in the understanding of the dynamics of 1D saturable WAs, we construct an energy landscape. By defining the center of mass  $X \equiv \sum_n n|u_n|^2/P$  and using a constraint method (see Sec. 3.2), we compute  $H$  versus  $X$  and  $P$ . Fig. 6.2(c) shows our computations around the first bistable region. In this plot,  $X = n$  and  $n + 1$  correspond to odd modes while  $X = n + 0.5$  corresponds to even one. For low power, the potential is cubic-like in the sense that the odd mode is stable while the even one is unstable (lower curve for  $P = 15$ ). By increasing the power, both fundamental solutions are simultaneously stable because they are both a local minima in this potential. Consequently, a maxima in-between appears, the unstable IS (middle curve for  $P = 20.5$  where  $\Delta H_0 \approx 0$ ). Then, by further increasing the power, the odd solution transforms into an unstable maxima while the even one becomes the only minima of this potential (upper curve for  $P = 26$ ). The IS originates when the even mode stabilizes; then it changes its center of mass to an odd mode (symmetrically to the right and to the left due to the system symmetry). Finally, the IS disappears when the odd mode destabilizes. In that sense, the IS can be thought as a stability catalyzer for the two fundamental modes.

To the best of our knowledge, mobility in this kind of systems was never predicted for a more realistic experimental input condition like gaussian input profiles. Previous simulations, starting from stationary solutions, observed good mobility [40, 45, 47]. However, saturable solutions are not well localized in the power-exchange regions and, furthermore, by increasing the power they become broader. Therefore, in a

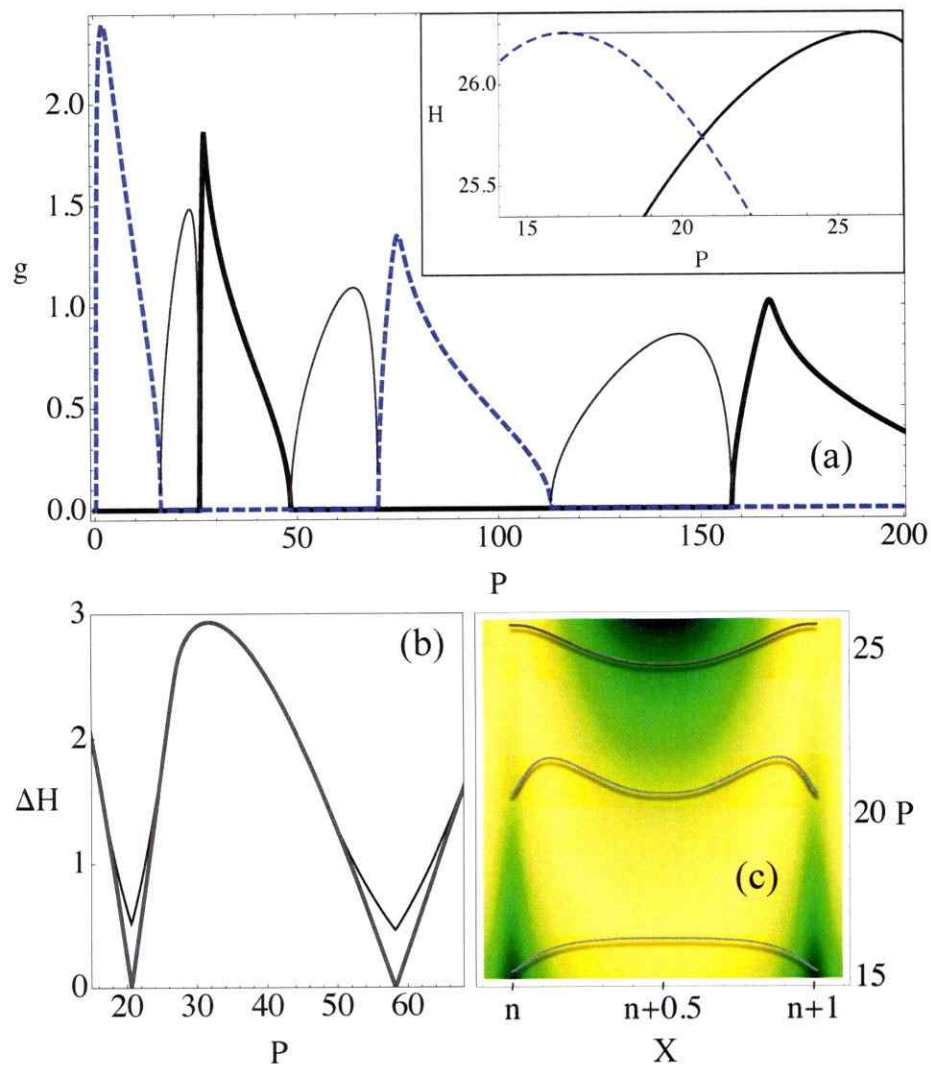


**Figure 6.2.:** (a)  $g$  versus  $P$  for odd, even, and intermediate solutions in full, dashed, and thin lines, respectively. Inset:  $H$  versus  $P$ . (b)  $\Delta H_0$  (thick line) and  $\Delta H$  (thin line) versus  $P$ . (c) Energy surface where light (dark) color denotes a high (low)  $H$ -value.

experiment, dynamics will be strongly determined by the power and shape of the chosen beam profile. We took as an input beam a five-site wide gaussian-like profile:  $u_n(0) = A \exp[-\alpha(n - n_c)^2] \exp[ik(n - n_c)]$  for  $n = n_c, n_c \pm 1, n_c \pm 2$ , and  $u_n(0) = 0$ , otherwise. The kick  $k$  is proportional to the experimental angle and it does not alter the power but adds a small amount of effective kinetic energy. With this initial condition, we numerically integrate model (6.1) from  $z = 0$  to  $z = z_f$  and measure the center of mass at the lattice output:  $X_f \equiv X(z_f)$ . Fig. 6.3(a) shows our results for different input power ( $P$ ). For very low power ( $P \sim 0$ ), the dynamics are essentially linear and mobility decreases as the system becomes nonlinear up to  $P \approx 50$ , when the saturable system behaves as a cubic one [see Fig. 6.3(b)]. Then, by further increasing the power, solutions start to move. When the power is increased, fundamental solutions are geometrically similar and differences in the Hamiltonian are very small, therefore the profile is allowed to move with  $k \neq 0$ , as it is observed in the average tendency of the curve [diagonal straight line with  $X_f \propto P$  in Fig. 6.3(a)]. However, some “resonant” dynamics is found for different levels of power. There are different regions where mobility is enhanced as shown in Figs.6.3(c) and (d). It is plausible to assume that this behavior corresponds to a manifestation of the continuously repeating bistable regions discussed for stationary solutions. Therefore, for even higher powers, there should be good mobility, in principle without limitations. The mobility windows for gaussian pulses do not coincide with the mobility regions for stationary solutions, since a gaussian pulse will always have a higher cost in power loss due to radiation. But, nevertheless, the recurrent appearance of enhanced mobility for certain powers shows an excellent

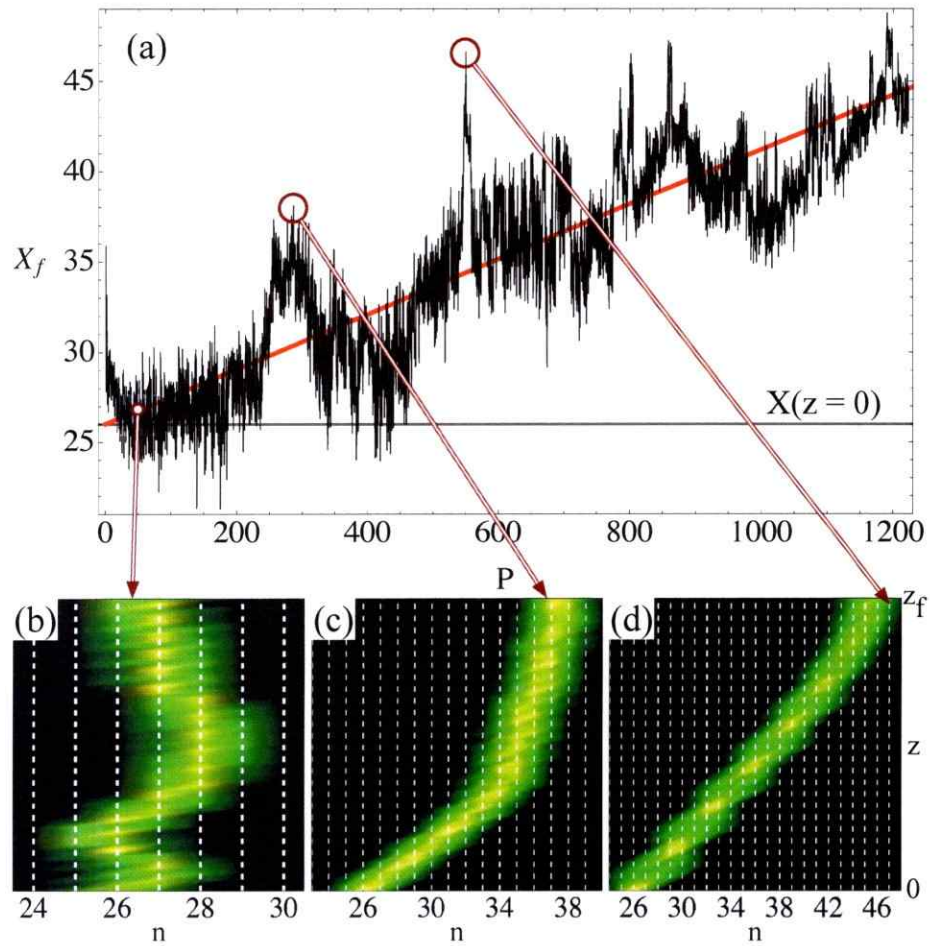


**Figure 6.3.:** (a) Output  $X_f$  versus input  $P$ . (b)-(d) Dynamical examples for  $P = 54, 300,$  and  $550,$  respectively.  $\gamma = 10, n_c = 26, k = 0.3, \alpha = 1/3, z_f = 50.$

agreement between gaussian and stationary profiles.

## 6.2. Directional mobility of discrete solitons in 2D lattices

It is still an open issue whether moving discrete solitons may exist as localized modes also in two-dimensional (2D) lattices. As was shown numerically in [47], a scenario with exchange of stability through bifurcations with asymmetric stationary solutions appears also for the 2D saturable model in an isotropic square lattice, involving in

this case three different types of fundamental solutions [158]: one-site (odd-odd, OO), two-site (odd-even, OE), and four-site (even-even, EE) modes. It was also shown numerically in [47], that solutions with good (but generally not radiationless) mobility in the axial directions may exist in these regimes, and that the necessary energy needed for rendering a mobile stable stationary solution agreed well with the concept of PN-barrier, if its definition was extended to take into account also the energy for the relevant intermediate stationary solution (an analogous situation is well-known for the PN potential of kinks [159]). Very similar observations were also made later for a 2D DNLS model with cubic-quintic nonlinearity [160]. Moreover, in the low-power regime of the 2D s-DNLS equations, good mobility was also observed in diagonal directions [47].

However, the relation between existence of regions of stability exchange, small PN-barrier and mobile localized solutions in 2D is not that trivial, as shown, e.g., for a model with cubic inter-site nonlinearities in [161]: even in regimes with small PN barrier and existence of intermediate solutions, the mobility may be very poor, if there is no continuous path in phase space passing close to the relevant stationary modes. On the other hand, as was observed for the low-power (i.e., close to continuum limit) regime of a 2D lattice with quadratic nonlinearity in [162], the effective Peierls-Nabarro potential may in some situations be weak enough to allow mobility in *arbitrary* directions, without any direct connection to bifurcations and symmetry-broken stationary solutions.

So there is clearly need for a better understanding of the conditions for mobility in 2D lattices. It is the purpose of the present section to generalize the concept



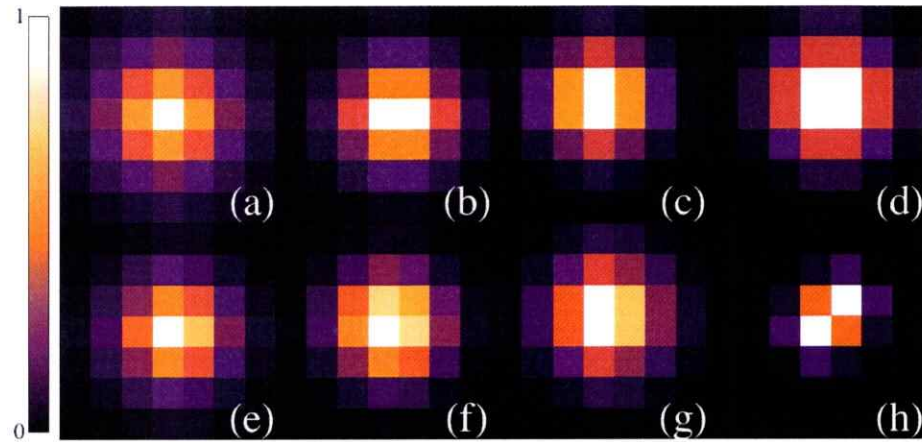


**Figure 6.4.:** Examples of spatial profiles for (a) one-site (OO), (b) two-site horizontal (EO), (c) two-site vertical (OE), (d) four-site solutions (EE), (e) IS1, (f) IS2, (g) IS3-vertical, and (h) diagonal solutions, respectively, illustrated for an isotropic lattice.

of PN-barrier as discussed above, and introduce a full 2D PN potential surface describing the pseudo-potential landscape in-between all stationary modes. We will use the numerical constrained Newton-Raphson (NR) method (sec. 3.2) to explicitly construct these surfaces for the 2D saturable model from [47], and show how parameter regimes and directions of good mobility may be immediately identified from smooth, flat parts of these surfaces. We will also illustrate how the interplay between translational motion in one lattice direction and oscillatory motion in the orthogonal direction can be intuitively understood from the topology of the corresponding PN surfaces.

The fundamental localized stationary solutions to Eq. (6.1), defined as solutions with real amplitudes  $u_{n,m}$  having a single maximum distributed on the sites in one unit-cell of the lattice, were described for the isotropic case in [47]. In general, we may

identify one-site (OO), two-site horizontal (EO), two-site vertical (OE), and four-site (EE) solutions. Figs. 6.4(a)-(d) show typical profiles for these types of excitations. As discussed in [47], all these in-phase localized solutions bifurcate from the fundamental linear mode, thus the upper band edge in the small-amplitude limit, and merge into the corresponding high-amplitude plane-wave mode in the infinite-power limit. As a consequence, they exist in the region  $\lambda \in [4 - \gamma, 4]$ , so that the size of the existence region will be just  $\gamma$ . [A two-site diagonal solution [163] [see Fig. 6.4(h)] could also be excited but only in frequency regimes where solutions are very localized with  $\lambda \lesssim 0$ , requiring large values of  $\gamma$  ( $\gamma \gtrsim 8.2$ )]. In addition, in certain parameter regimes there are also asymmetric, intermediate stationary solutions, associated with exchange of stability between the symmetric ones [47]. We may identify three types of such solutions, termed henceforth intermediate 1 (IS1), intermediate 2 (IS2), and intermediate 3 (IS3), respectively. IS1 and IS3 both connect a stable two-site mode, OE/EO, with another simultaneously stable solution: the one-site mode OO (IS1), or the four-site mode EE (IS3) [see Figs. 6.4(e) and (g)]. Thus, in these cases the unstable intermediate solutions act as carriers of instability between the corresponding fundamental modes. The unstable IS2 solution exists when both two-site solutions are stable. As can be seen in Fig. 6.6(c), it is a saddle point carrying a minimum, which connects the unstable one-site solution OO with the likewise unstable four-site solution EE, and stabilizes the latter mode upon reaching it [see Fig. 6.4(f)].

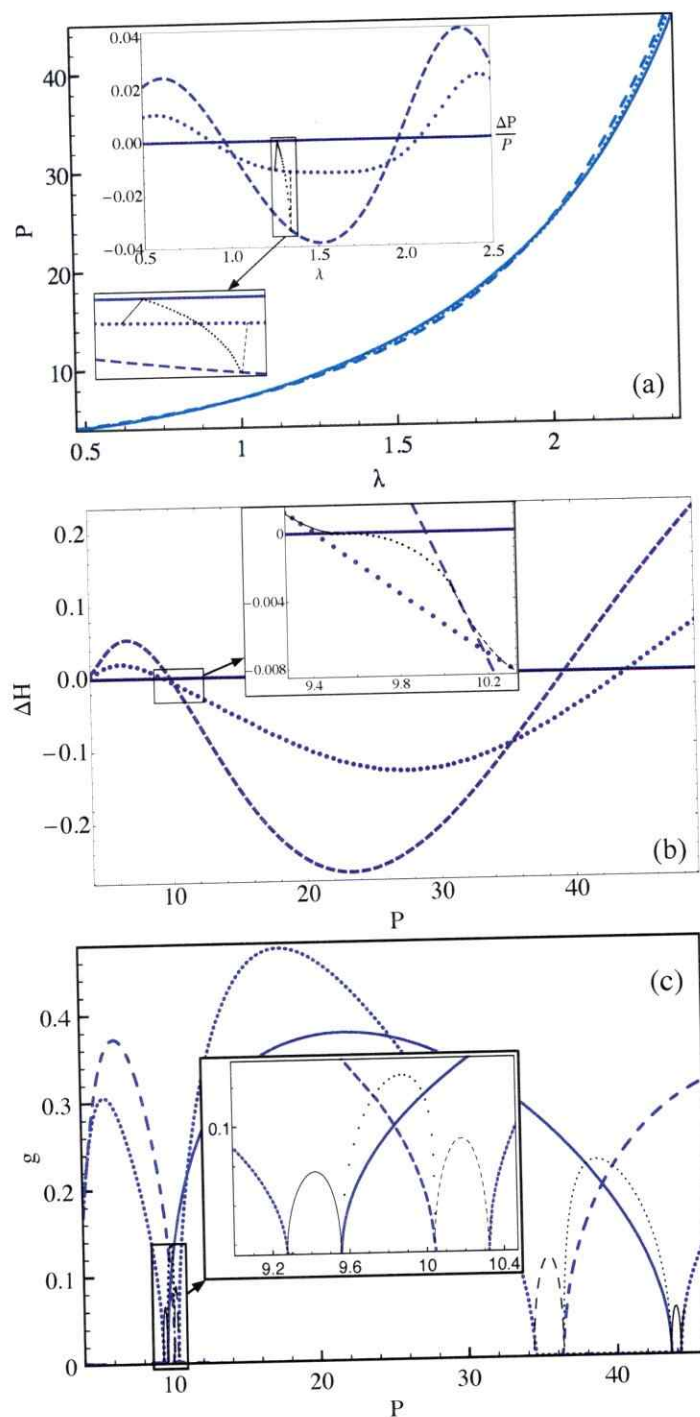


**Figure 6.5.:** Properties of fundamental stationary solutions for  $\gamma = 4$ : (a) Power versus frequency; (a)-inset:  $\Delta P/P$  versus  $\lambda$ ; (b)  $\Delta H$  versus power; (c) Stability versus power. Different solutions are plotted with different line-types: one-site (thick solid blue), two-site (thick dotted blue), four-site (thick dashed blue), IS1 (thin solid black), IS2 (thin dotted black), and IS3 (thin dashed black), respectively.

Figs. 6.5 shows fundamental properties of different stationary solutions for an isotropic lattice with  $\gamma = 4$ . Power versus frequency curve is shown in Fig. 6.5(a), where different solutions repeatedly cross each other in the whole range of parameters. In Fig. 6.5(a)-inset we plot  $\Delta P/P \equiv (P_i - P_{OO})/P_{OO}$  as a function of  $\lambda$ , for  $i = OO, EO/OE, EE, IS1, IS2, IS3$ . This figure shows clearly how solutions cross each other including many intermediate solutions appearing in the region  $\lambda \sim 1.3$ . Moreover, we also observe these crossings when plotting  $\Delta H \equiv H_i - H_{OO}$  versus power [Fig. 6.5(b)]. (We plot  $\Delta H$  instead of  $H$  because Hamiltonian differences between stationary solutions of the same power are generally quite small, which is indeed a favorable scenario for moving solutions). Inset in Fig. 6.5(b) shows a zoom in the region  $P \sim 9.8$  where the Hamiltonian of different fundamental solutions matches at some points. Good mobility may be expected close to these regions but, still, it will be strongly determined by the specific kick or perturbation given to the solution in order to put it in motion.

Stability versus power for the same solutions as in Figs. 6.5(a), (b) is shown in Fig. 6.5(c). From this figure, we can see how unstable intermediate solutions IS1, IS2, IS3 appear when two or three solutions (regarding OE and EO as different solutions) are simultaneously stable. Note that we never observed regions for simultaneously stable one and four-site solutions for isotropic coupling, but in the anisotropic case such regions do exist [164].

### 6.2.1. Description of PN surfaces

By exploring the parameter-space  $(\gamma, P)$ , we have identified regions where we were able to compute complete two-dimensional energy surfaces (using an constraint method as shown in Sec. 3.2) and regions where we cannot. In general, complete surfaces could not be obtained for large values of the nonlinearity constant,  $\gamma \gtrsim 6$ , when solutions get strongly localized. In some cases we were able to trace some specific mobility directions (e.g., along lattice axes or diagonal) connecting stationary solutions with almost equal Hamiltonian, but not the full two-dimensional scenario involving all fundamental solutions. Note also that, as remarked in [47], for large  $\gamma$  and small power the s-DNLS model essentially behaves as a cubic DNLS model with effective nonlinearity  $\gamma P$ . Consequently, we could not find complete energy surfaces with all fundamental solutions for the cubic DNLS either (although surfaces involving the two-site diagonal solution in place of the EE solution could be obtained as mentioned in Sec. 3.2; for the cubic DNLS this two-site solution does exist as a true stationary solution above some level of power [163]).

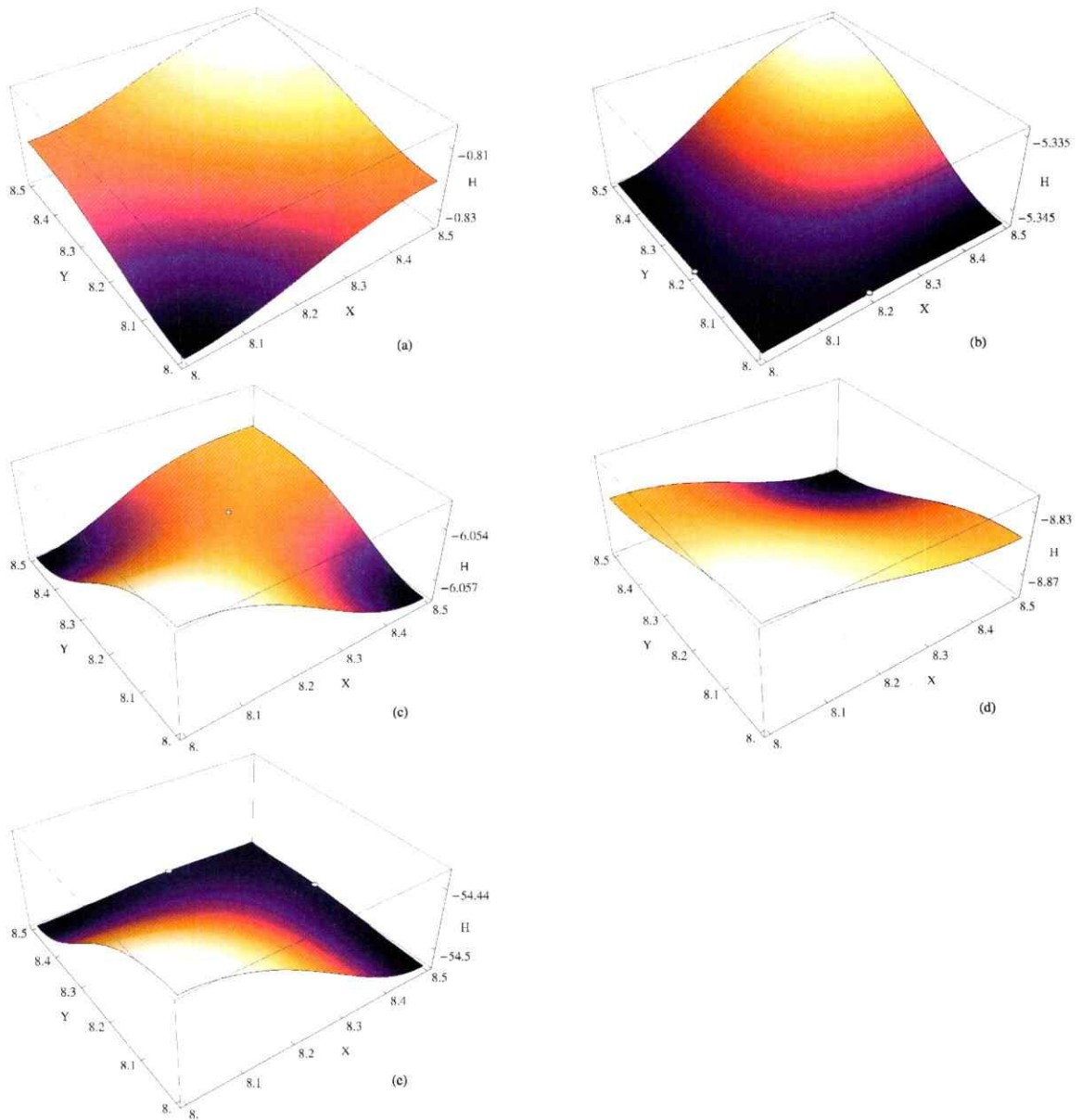


**Figure 6.6.:** Energy surfaces for  $\gamma = 4$ , in the five different power regimes discussed in the text : (a)  $P = 5$ ; (b)  $P = 9.45$ ; (c)  $P = 10$ ; (d)  $P = 12$ ; (e)  $P = 35.5$ . The center of mass  $\{X, Y\}$  for the four stationary solutions are:  $\{8, 8\}$  (OO),  $\{8.5, 8\}$  (EO),  $\{8, 8.5\}$  (OE), and  $\{8.5, 8.5\}$  (EE). White dots denote local extrema corresponding to intermediate solutions. (System size  $N = M = 15$  and fixed boundary conditions were used.)

On the other hand, for very small values of  $\gamma$ , the computation of energy surfaces becomes difficult for technical reasons: due to the widening of the solutions, considerably larger lattices are needed to remove the influence from boundary effects. Therefore, in the following, we will present the main phenomenology for the isotropic case found for intermediate values of  $\gamma$ ,  $3 \lesssim \gamma \lesssim 5$ , where complete surfaces involving all four fundamental solutions were obtained for all values of the power. We will present results for the particular value  $\gamma = 4$ , but the scenario is found to be qualitatively the same for all  $\gamma$  in this interval.

From Fig. 6.5(c), we may identify essentially five different regimes where energy surfaces of qualitatively different nature should be expected, depending on the level of power. The first one is for low power, where (similarly to the cubic DNLS) the one-site solution is always stable and the other fundamental stationary solutions are all unstable. The corresponding energy surface is illustrated in Fig. 6.6(a), where the one-site solution yields the energy minimum, the two-site solutions saddle points and the four-site solution the maximum. Note that, in this low-power regime, the surfaces for this value of  $\gamma$  are still rather flat, and therefore some mobility may result if the one-site solution is kicked to overcome the barriers, in the axial as well as in the diagonal directions, as illustrated by Figs. 4(a) and (c) in Ref. [47]. (Another example of mobility in this regime is discussed in Sec. 6.2.2 below.)

The saturable nature of the system becomes evident at higher powers. In the second regime, appearing for the first time when  $9.27 \lesssim P \lesssim 9.55$ , the one- and the two-site solutions are stable simultaneously and, as shown in Fig. 6.6(b), these three points all correspond to local minima of the surface. Intermediate solutions IS1 connecting

the one- with the two-site solutions in the horizontal and vertical directions appear as saddle points [white dots in Fig. 6.6(b)]. Note that the energy landscape for the parameter values in Fig. 6.6(b) is almost flat between the one-site and two-site solutions in the axial directions, leading to the very good axial mobility shown in Fig. 4 (d) of Ref. [47], while the maximum corresponding to the unstable four-site solution creates a too large effective barrier to overcome in the diagonal direction.

The third power region is the one in which only the two-site solutions are stable. It appears for the first time when  $9.55 \lesssim P \lesssim 10.04$ , and is illustrated in Fig. 6.6(c). Here, the stable two-site solutions correspond to two local minima of the surface, and the unstable one- and four-site solutions both to local maxima. The two unstable solutions are connected by the intermediate solution IS2 (white dot at the surface), corresponding to a saddle point which for symmetry reasons (for the isotropic lattice) will lie along the diagonal connecting the unstable solutions. As will be illustrated in Sec. 6.2.2, the easiest mobility in this case is expected to occur in a diagonal direction, connecting the two stable stationary solutions.

The fourth regime corresponds to simultaneously stable two- and four-site solutions. Such a regime appears for the first time when  $10.04 \lesssim P \lesssim 10.32$ . If we further increase the power, we will find a similar region with these three simultaneously stable solutions for  $34.5 \lesssim P \lesssim 36.25$ . In this regime, as illustrated in Fig. 6.6(e), the two- and four-site solutions all correspond to minima, the unstable intermediate solutions IS3 to saddle points, and the one-site solution to a maximum. Thus, comparing Figs. 6.6(b) and (e), we see that the structure of the potential has been completely inverted. Now, a big "hill" is located at the one-site solution, and as a



consequence no mobility is expected involving this solution. As will be shown below in Sec. 6.2.2, the simplest mobility scenario will now be the one in which the two-site solutions travel through the four-site one across the lattice.

The fifth regime, with the four-site solution being the only stable one, occurs for the first time when  $10.32 \lesssim P \lesssim 34.5$ . As illustrated in Fig. 6.6(d), the four-site solution is now a minimum of the PN potential, while the other three unstable solutions correspond to saddle points (EO and OE) and maximum (OO), respectively. (There are no intermediate solutions in this regime.) Thus, by increasing the power we have now reverted the surface compared to the low-power regime in Fig. 6.6(a).

Further increasing of power for  $36.25 \lesssim P \lesssim 43.6$  exhibits a new region of stable two-site solutions, corresponding to the third regime. For  $43.6 \lesssim P \lesssim 44.2$  the one- and two-site solutions are simultaneously stable, so the scenario is equivalent to the second regime, followed again for  $P \gtrsim 44.2$  by the first regime, respectively. This second complete inversion thus corresponds to a regain of the low-power characteristics of the surface. Furthermore, repetition of these scenarios can be found for  $P \gtrsim 118$ , and we confirmed, e.g., the existence of a complete, smooth surface, analogous to the one shown in Fig. 6.6(d) for the fifth regime (for  $P = 120$ ).

### 6.2.2. Mobility dynamics for isotropic lattices

To explicitly show the connection between the different types of energy surfaces described in Sec. 6.2.1 and the mobility of localized solutions, we numerically integrate model (6.1) by taking as initial condition a stationary solution  $u_{n,m}$  perturbed with a small kick:

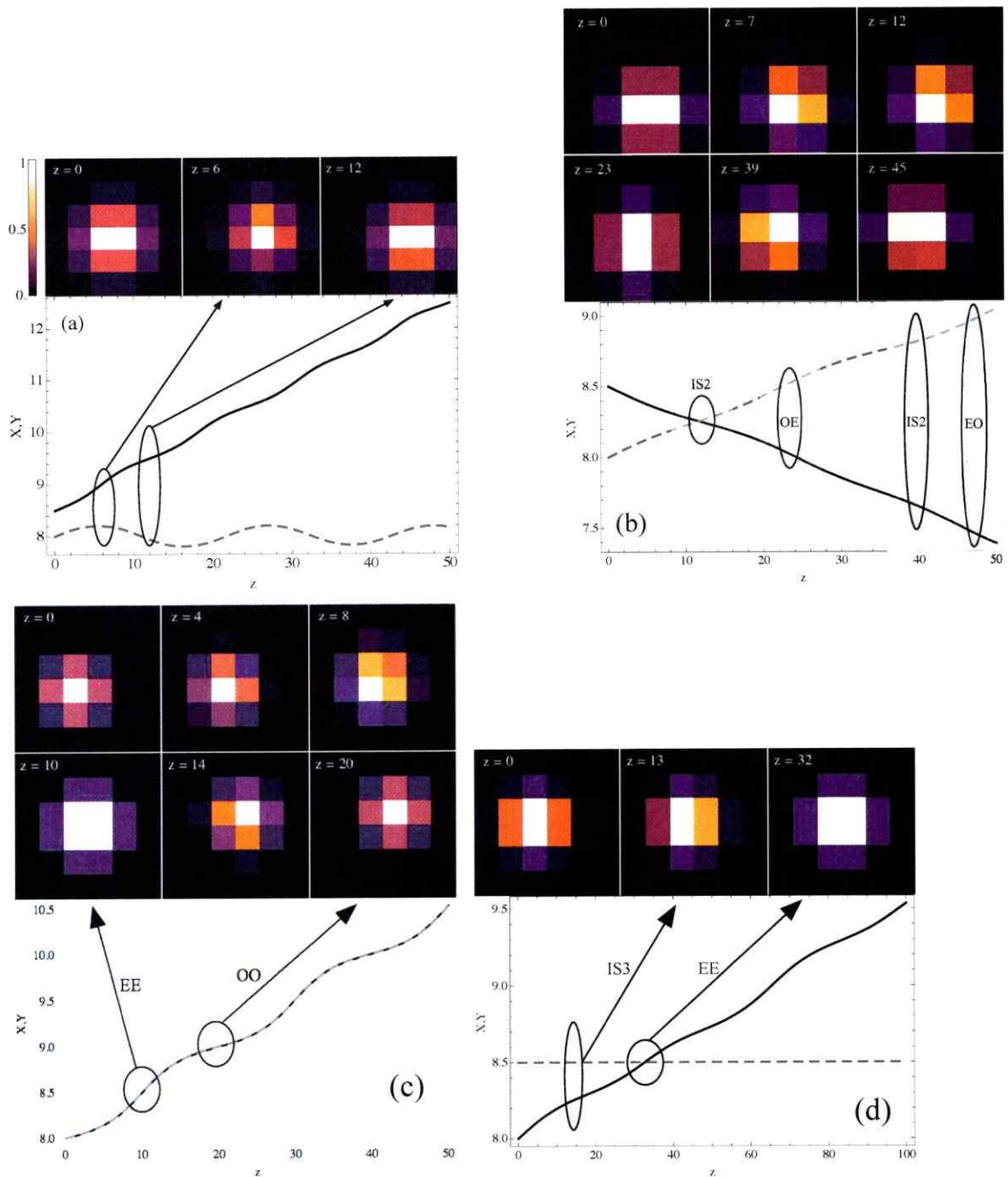


**Figure 6.7.:** Examples of mobility dynamics in the propagation direction  $z$ , corresponding to surfaces shown in Fig. 6.6(a), (c), (d), and (e), respectively. In each subfigure, top figures show profiles movement [(a) shows a colormap where colors were normalized to the maximum amplitude of each plot; this colormap also applies to (b)-(d)], and bottom figures center of mass evolution for  $X$  (full line) and  $Y$  (dashed line). (a)  $P = 5$ ,  $k_x = k_y = 0.038$ ; (b)  $P = 10$ ,  $-k_x = k_y = 0.018$ ; (c)  $P = 12$ ,  $k_x = k_y = 0.015$ ; (d)  $P = 35.5$ ,  $k_x = 0.015$  and  $k_y = 0$ . (Other parameter values are the same as in Fig. 6.6.)

$U_{n,m}(0) = u_{n,m} \exp[ik_x(n - n_c) + ik_y(m - m_c)]$ , where  $k_x$  and  $k_y$  correspond to the kick strength in the horizontal and vertical directions, respectively.

If the surfaces would be completely flat, solutions should move even with an infinitesimally small kick. However, as we have seen, in general surfaces are not flat due to the discreteness and the self-induced PN potential, and although the PN barrier can be very small in certain directions, it is generally non-zero. Therefore, in order to put a localized solution in movement, some amount of kinetic energy (represented by this kick) should be given to effectively overcome the energy barriers.

We first discuss an example from the first, low-power, regime corresponding to the energy surface in Fig. 6.6(a) (as mentioned above, different mobility examples from this regime were shown in Figs. 4 (a) and (c) in Ref. [47]). Here, we took the (unstable) EO solution and kicked it with very small  $k_x$  and  $k_y$  in both directions, yielding the dynamics numerically observed in Fig. 6.7(a). In the  $y$ -direction, the kinetic energy is not sufficient to overcome the barrier created by the four-site solution, while in the  $x$ -direction it can move towards the minimum corresponding to the one-site solution. The resulting dynamics for the center-of-mass positions show how the movement in the horizontal direction gets combined with oscillations in the vertical one. The dependence  $X$  vs  $z$  also clearly shows how the solution feels the potential in terms of its velocity: maximum velocities occur around integer lattice sites (where the potential is a minimum) while the minimum velocities occur close to middle points (see full line in Fig. 6.7(a); compare also with the analogous scenarios for the kicked OO mode in Figs. 4 (a) and (c) of Ref. [47]).

In the second power regime, with energy surfaces as in Fig. 6.6(b), good mobility

can be expected only in axial directions, with effective energy barrier determined by the intermediate solution between the one- and the two-site solutions (as discussed in Ref. [47]). The solution moves very slowly and adiabatically traces the shape of the potential with a minimal velocity at the places of the intermediate solutions.

In the third power regime, with surfaces as in Fig. 6.6(c), a very interesting kind of mobility is observed: a diagonal mobility between the (stable) horizontal and vertical two-site solutions as illustrated in Fig. 6.7(b). The initial EO solution, kicked equally in the  $(-x)$ - and  $y$ -directions, gets sufficient kinetic energy to pass over the small barrier created by the intermediate IS2 solution. It then continues through the OE solution, passes another IS2 barrier, and then to the other EO solution shifted by one site in both directions. Although the potential connecting these two solutions is not completely flat, there is a very good transport of energy in this direction, allowing mobility for more than one lattice diagonal in the considered  $15 \times 15$  lattice.

If we take a look at the surface in the fifth power regime [Fig. 6.6(d)], we realize that an initial (unstable) one-site solution may move in any direction by slightly kicking it since it corresponds to a maximum. Fig. 6.7(c) shows an example for kicking the one-site solution symmetrically in both directions in order to make it move passing through the four-site, i.e., a diagonal movement. The velocity has maximum in the minima of the potential (corresponding to the EE solution) and minimum in the potential maxima (OO solution) (no intermediate solutions appear in this regime).

Finally, in the fourth power regime, we see from the surface [Fig. 6.6(e)] that the two- and four-site solutions are stable simultaneously, presenting an intermediate solution in-between them, that will define the effective energy barrier. This barrier is very

small and, therefore, a very small kick is required. Figure 6.7(d) shows the evolution starting from a two-site vertical solution, passing through the intermediate one and arriving to the four-site solution.

As illustrated by the example in Fig. 6.7(a), the energy surfaces also provide intuitive interpretations to the observed dynamics of discrete solitons with additional perturbations *transverse* to the direction of motion.

In conclusion, we have carried out a deep study on the problem of mobility of localized modes. For nonlinear saturable 1D photonic lattices we found several regions of bistability where stationary solutions possess a small but nonzero energy barrier. The effective energy barrier among all stationary localized solutions was constructed, allowing us to get a deeper understanding of discrete saturable nonlinear systems. By using these properties with a more realistic input condition, we were able to observe very good mobility and also to find different regions of resonant response where the mobility is enhanced.

In two-dimensional saturable discrete systems we numerically implemented a constrained Newton-Raphson method to construct full Peierls-Nabarro energy surfaces, which appeared as very useful tools for predicting the dynamical properties of localized excitations. Although these surfaces were never found to be completely flat (and therefore the corresponding Peierls-Nabarro barriers is strictly never zero), parameter regimes and directions of good mobility were observed to correspond to smooth and flat parts of the surfaces.

Five different surface topologies could be identified in different power regimes, depending on the stability properties of the different fundamental stationary solitons.

By numerically studying the dynamics of perturbed stationary solutions, we showed how these different topologies yielded qualitatively different kinds of optimal mobility, generally in axial or diagonal directions and with velocities varying according to the shape of the potential while the profile is propagating across the lattice. The energy surfaces were also found to be very useful for interpreting the dynamics resulting from the interplay between translational and oscillatory motion in orthogonal directions.

Thus, the constraint method developed in this thesis appears to be a very good tool for the understanding of the mobility dynamics of localized excitations in higher-dimensional lattices, clearly showing the effective energy barriers that localized solutions experience.

## 7. Vortices in discrete saturable arrays

Periodic media and discrete systems can not only support localized modes with real amplitudes, but also solutions with an additional phase structure like discrete vortices. These modes have one or various phase singularities and were first theoretically studied in discrete lattices [50, 51] and in continuous models with an external potential [52, 53]. Experimentally, they were observed simultaneously by two groups [54, 55]. Since then, different vortex mode families and their stability, in the discrete nonlinear Schrödinger (DNLS) model [57, 56], have been analyzed. Discrete vortices (DV) come in many configurations. They are characterized by their topological charge or winding number  $S$ , which counts the number of phase turns between 0 and  $2\pi$  along a closed contour around the phase singularity. But additional phase singularities [126] can lead to multi-charged vortex modes [59, 165] and vortex clusters [166]. In contrast to square lattices, different lattice geometries can allow stability also for higher topological charges [60] or stable combinations of dipole vortices [61]. In the case of defocusing nonlinearity, higher-order modes were also found to be stable [62, 63]. Introduction of anisotropy in square lattices also has a strong influence on the stability of higher charged vortex clusters [168].

There are numerous ways to distribute the amplitudes around the phase singularity, for the continuous saturable lattice model various families of charge-1 ( $S = 1$ ) vortices were predicted to exist outside the linear bands [167].

One interesting aspect, which has not been studied yet is the excitation of nonlinear vortex modes bifurcating from a linear solution. Linear vortex modes can be formed as a linear combination of band modes and continued into the nonlinear regime. Furthermore, we will explore, which kinds of DV can be stable for charge  $S = 1, 2, 3$  in discrete saturable arrays in different amplitude geometries for a fixed nonlinearity  $\gamma = 10$ , which allows for well separated bands.

For a general complex stationary solution of the 2D version of equation (2.29) with frequency  $\lambda$  we can write  $u_{n,m}(z) = u_{n,m} \exp(i\lambda z) = (x_{n,m} + iy_{n,m}) \exp(i\lambda z)$  with  $x_{n,m}, y_{n,m} \in \mathbb{R}$ , what yields

$$\lambda x_{n,m} = \Delta x_{n,m} - \frac{\gamma x_{n,m}}{1 + x_{n,m}^2 + y_{n,m}^2}, \quad (7.1)$$

$$\lambda y_{n,m} = \Delta y_{n,m} - \frac{\gamma y_{n,m}}{1 + x_{n,m}^2 + y_{n,m}^2}.$$

Here  $\Delta u_{n,m} = u_{n-1,m} + u_{n+1,m} + u_{n,m-1} + u_{n,m+1}$  is the 2D linear interaction term.

In order to study the linear stability of stationary localized solutions we refer to the method described in section 3.1.

### 7.1. From discrete linear vortices to combined solutions

We already presented in Sec. 2.3 the two linear bands in the s-DNLS model. The first one is found in the limit of small amplitudes,  $\lambda \in [-4 - \gamma, 4 - \gamma]$ , the second one



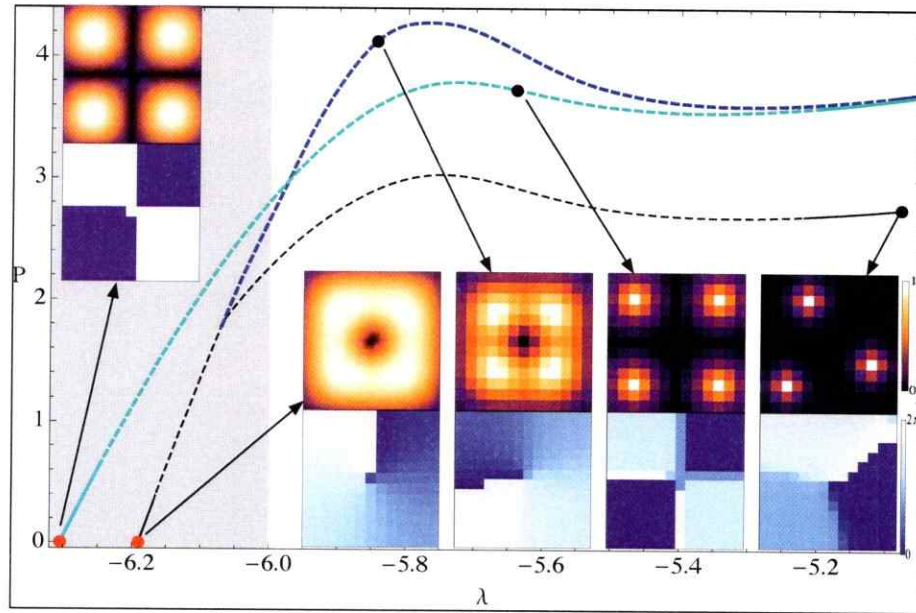


**Figure 7.1.:**  $P$  vs.  $\lambda$  continuation of linear vortices in the saturable case,  $\gamma = 10$ . For  $S = 1$ , two possible continuations were found (black and blue),  $S = 2$  is shown with a green line. The stable (unstable) regimes are plotted with full (dashed) lines, insets show amplitude and phase examples corresponding to the dots.

for high powers and  $\lambda \in [-4, 4]$ . To find the modes, we solve the linear Eigenvalue problem in the small amplitude limit of Eqs.(7.1) for an array of  $N^2$  sites. The Eigenmodes  $x_{n,m}$  and  $y_{n,m}$  are both denoted by  $v_{n,m}$  and given by:

$$v_{n,m}^{i,j} = \sin(k_i n) \sin(k_j m) \text{ for } i, j = 1, 2, \dots, N, \quad (7.2)$$

where  $k_l = \pi l / (N + 1)$  with Eigenfrequencies

$$\omega_{i,j} = 2[\cos(k_i) + \cos(k_j)]. \quad (7.3)$$

It is possible to construct discrete linear vortices(DLV): solutions consisting of superposition of Eigenmodes (7.2), which vanish at the lattice borders and have a defined

topological charge with a phase-singularity. A discrete linear vortex, with topological charge  $S = 1$ , is given by

$$u_{n,m} = (x_{n,m}^{1,2} + iy_{n,m}^{2,1}), \quad (7.4)$$

whereas the solution

$$u_{n,m} = (x_{n,m}^{2,2} + iy_{n,m}^{2,2}), \quad (7.5)$$

yields a discrete linear vortex with vorticity  $S = 2$ . To construct these combined linear modes an identical eigenfrequency  $\omega_{i,j}$  is necessary in order to excite a dynamically stationary pattern. Both DLV are marked in Fig. 7.1 with red dots. The respective nonlinear modes can be continued from linear modes inside the band in the limit of vanishing amplitude by using a multidimensional Newton-Raphson method. In Fig. 7.1 we plot Power  $P$  vs. frequency  $\lambda$  for a  $15 \times 15$  array and  $\gamma = 10$ . Additionally we perform a standard linear stability analysis. In Fig. 7.1 see, that the continuations of the linear vortex modes preserve at first the linear stability of the band modes, but with growing frequency  $\lambda$  they turn unstable, but return to stability for higher powers. This behavior is represented by full lines for stable modes and dashed curves marking instability, respectively. In the case of the  $S = 1$  modes, we found a very interesting behavior. At some point near, but below the band edge the donut-shaped solution bifurcates into two branches, which have either 3 or 4 local maxima, that get more and more pronounced with increasing frequency. These modes evolve into a combination of 3 and 4 peaks, respectively, conserving the

vorticity of  $S = 1$ . Examples are shown in the inset of Fig. 7.1. We assume, that in the case of larger lattice sizes other scenarios with more or less peaks may occur. For instance, for a  $25 \times 25$  array we found as well a two peak solution, but the symmetry of the lattice will nevertheless favour four-peaked modes (blue line). "Spatially compact" DV modes can not be formed as linear combination of band modes due to their intrinsic distribution over the whole lattice. Therefore, localized vortices do not bifurcate from the linear DLV and possess an unavoidable power threshold.

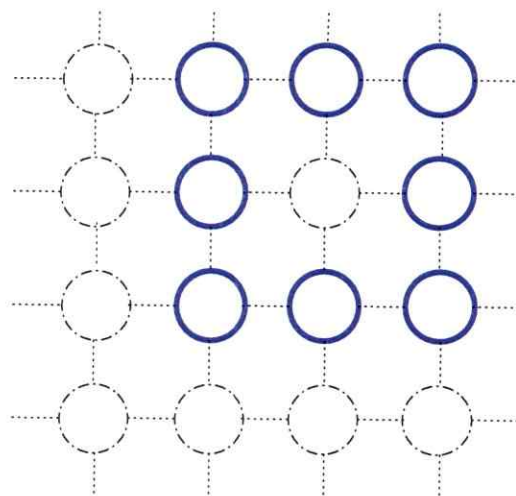


**Figure 7.2.:** Scheme of a  $c = 1$  vortex structure

## 7.2. Mode families

We will now construct the different families of DV solutions with their specific phase and amplitude profiles in a  $21 \times 21$  array. One can define several families, depending on the number of sites ( $c$ ) with small or vanishing amplitude in the center and topological charge ( $S$ ). An example of a scheme for an amplitude distribution with  $c = 1$  is shown in Fig. 7.2, where the blue sites denote the excited sites, whereas the

black dashed site in the center has a vanishing amplitude and a phase singularity. In the following, we explore possible configurations with  $c = 0, 1, 2, 4$  and  $S = 1, 2, 3$  and additionally perform the stability analysis.

For  $c = 0$ , the DV's correspond to the so called quadrupole solitons [62] and can only exist with charge  $S = 1, 2$  [56]. In the discrete saturable case both types can be marginally stable in a finite power-interval, as shown in Fig. 7.3(a) with full lines. It is important to note, that there is no bifurcation from a linear mode and both families exhibit coexistence of at least two possible solutions for fixed power. In the case of  $S = 2$ , there is even a power interval with 4 simultaneous solutions, one stable and three of them unstable. All curves are closed. This behavior can be understood as follows: One family has to be either connected to a linear mode or mode superposition or can start and cease to exist via saddle-node bifurcations. Since the low-power linear band is forbidden due to the localized character of the DV, there will be a bifurcation in the vicinity creating solution-pairs. Thus they have to disappear as well in pairs or both be connected into the high-power linear band.

Typical amplitude and phase examples corresponding to the dots in the plots are shown in the insets of Fig. 7.3.

For  $c = 1$ , shown in Fig. 7.3(b), we were able to find DV's with  $S = 1, 2, 3$ , again there are stable regimes for all solution types, the curves are closed and completely located outside the low power linear band. For two central sites,  $c = 2$  [ see Fig. 7.3(c)], we found only unstable vortices, which we assume to be caused by the asymmetry of the configuration.

For  $c = 4$  and  $S = 2, 3$ , [Fig. 7.4(a)] we found two families for either charge, one of them centered more in the corners of the vortex mode, the other one centered on the sides. Only the "corner centered" solution with  $S = 2$  presents a stable regime, all others were found to be unstable everywhere. The most interesting case can be found for  $c \geq 4$  and  $S = 1$ . Here we found the coexistence of at least 6 branches, one of them reaching the high-amplitude band. The continuation in the lower power regime showed signs of a multitudinous existence of branches, similar to the continuous case [167]. Remarkable is the coexistence of two simultaneously stable branches, which furthermore are nearly equal in power and frequency, examples are shown in Fig. 7.4(c4,c5) and in the right inset. All stable structures possess four pronounced peaks with some overlap with rather well separated phase distributions. In addition we show in Fig. 7.4(b) the continuation from the linear vortex mode outside the band into the high amplitude linear band. This mode has 4 peaks with a fixed phase for each of them around 4 central sides. This structure can be found to be stable in the same power regime, where the  $c \geq 4$  family stabilizes with comparable, only slightly different frequency. We interpret this behavior as follows: Due to the saturable nature of the system the modes are more extended close to the bands and more localized far from them. When the DV has very pronounced peaks, it can also be constructed from different discrete solitons with an additional phase structure. They can be stable, when they are far from each other. The appearance of the existence of extra branches can be understood as the "continuation and multiplication" of the behavior found in other families, where we observed up to 4 simultaneously existing solutions, but since for  $c \geq 4$  the peaks are more separated, the "directions" of

growth or saturation of the solution has more possibilities. The growing mechanism shifts the peak centers further and further away from the starting  $c = 4$  seed, the number of branches to be found will be mainly restricted by the system size. This very special modes should therefore be able to connect to the DLV modes in finite lattices; we found at least the continuation of one branch into the high-Power band. In conclusion, we observed the continuation of linear vortex modes in s-DNLS lattices into the nonlinear regime and constructed furthermore closed DV families located outside the linear bands. The special branching mechanisms found for the family with  $c \geq 4$  and  $S = 1$  were attributed to saturation effects.

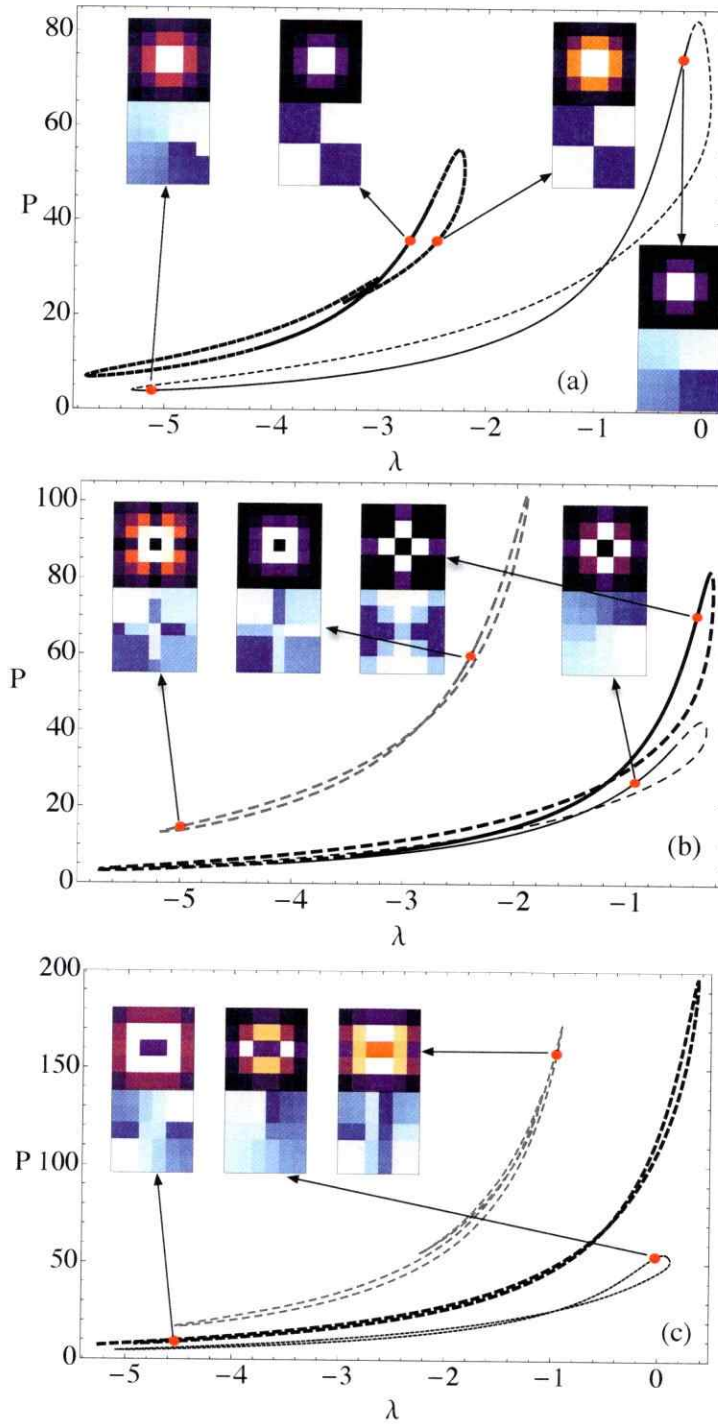


**Figure 7.3.:**  $P$  vs.  $\lambda$ , (a)  $c = 0$  for  $S = 1(2)$  shown with thin (thick) lines. (b) for  $c = 1$ ,  $S = 1(2,3)$  shown in thin (thick, gray), and (c)  $c = 2$ ,  $S = 1(2,3)$  showed in thin (thick, gray). The stable (unstable) regimes are plotted with full (dashed) lines, insets show amplitude and phase examples corresponding to the dots.

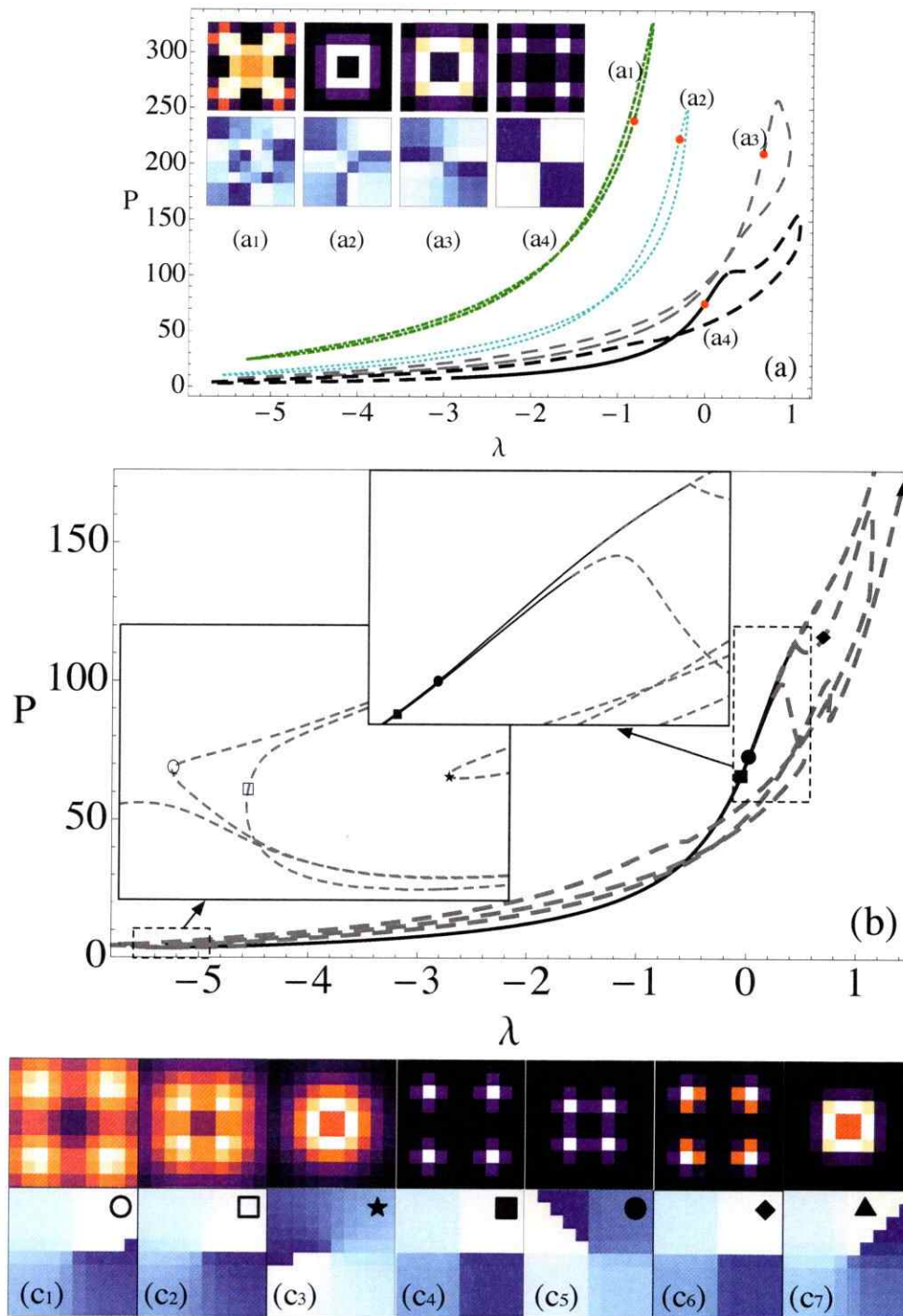


**Figure 7.4.:** (a)  $P$  vs.  $\lambda$ ,  $c = 4$  for two different families:  $S = 2$  is shown with a thick black line, where dashed parts denote the instability, while all other families are completely unstable.  $S = 3$  is plotted with a dotted (dotdashed) line. Amplitude and phase examples correspond to the dots. (b)  $P$  vs.  $\lambda$ , for  $S = 1$  and  $c \geq 4$ , (c) profiles and phases, from (1)-(7) corresponding to the empty circle, empty square, star, filled square, circle, diamond and triangle, respectively



## 8. Conclusion and Outlook

This thesis focused on spatially localized modes in nonlinear waveguide arrays. Special interest was taken in the effect on localization and wavepacket spreading caused by linear and nonlinear impurities and disorder in finite arrays. The mobility of localized modes in nonlinear saturable lattices is discussed and complex localized solutions with a nontrivial phase structure are studied.

A Coupled-Mode-Theory approach for nonlinear waveguide arrays leading to a Discrete Non Linear Schrödinger equation was introduced in Chapter 2. The nonlinear mechanisms were presented and linear - as well as some of the properties of nonlinear stationary solutions - of this equation set were discussed.

We introduced some numerical methods, which were used and improved in the present thesis, like the stability analysis presented for general *complex* stationary solutions as well as a constraint method used to construct pseudo-potential energy landscapes.

Chapter 4 discussed the problem of Fano resonances, with a focus on linear properties in the context of magnetic Metamaterials, whereas a nonlinear Fano problem was

discussed for saturable waveguide arrays.

We examined Fano resonance effects in split ring resonator arrays coupled to internal (capacitive) and external (inductive) defects. In the case of embedded defects, the presence of coupling to second neighbors, in addition to the usual first neighbor coupling, was necessary to induce the resonance phenomena. For external defects, the Fano phenomenon depended mainly of the geometric configuration between the defect(s) and the array. The position and strength of these resonances showed a clear example of the possibility of controlling the transport of electromagnetic waves across magnetic metamaterials. We also proposed a possible setup for observing Fano resonances in nonlinear optical waveguide arrays. A very good agreement between theory and numerical simulations was found showing the possibility to tune the resonance behavior by means of the amplitude of the localized mode. The allowed power interval of the localized modes necessary for the observation of Fano resonances was clearly identified and confirmed by direct numerical calculations.

Chapter 5 was dedicated to disorder. We presented a brief introduction to the concept of Anderson localization. We discussed the influence of disorder on wave propagation in finite nonlinear arrays. We showed, numerically and experimentally, that the presence of weak disorder can lead to the smoothing of the distribution of an initially localized optical beam in 1D and 2D waveguide arrays after a finite propagation length. Moreover, the addition of focusing nonlinearity facilitates this effect even further. The regions of smoothed distribution (weak disorder) and localization (strong disorder) could be clearly separated. The general behavior can be explained in terms of simple dynamical arguments.

We investigated experimentally the influence of a disordered boundary in a finite 2D coupled waveguide array and found asymptotic partial localization of the wave packet in the center of the bulk region far away from the boundary. We concluded, that the presence of a disordered boundary can give rise to localization in regions away from the boundary. This result could be extrapolated to larger finite lattices, if one allows for a sufficiently long propagation distance.

The mobility of nonlinear localized solutions in 1D and 2D saturable lattices were discussed in Chapter 6. In 1D photonic lattices several regions of bistability were found, where stationary solutions possess a small but nonzero energy barrier. The effective energy barrier among all stationary localized solutions was constructed allowing us to get a deeper understanding of discrete saturable nonlinear systems. By using these properties with a more realistic input condition, we were able to observe very good mobility and also to find different regions of resonant response where the mobility is enhanced. In two-dimensional saturable discrete systems we numerically implemented an improved constrained Newton-Raphson method to construct full Peierls-Nabarro energy surfaces, which appeared as very useful tools for predicting the dynamical properties of localized excitations. Five different surface topologies could be identified in different power regimes, depending on the stability properties of the different fundamental stationary solitons. Although these surfaces were never found to be completely flat (and therefore the corresponding Peierls-Nabarro barriers is strictly never zero), parameter regimes and directions of good mobility were shown to correspond to smooth, flat parts of the surfaces.

Discrete vortices, complex localized solutions with a phase singularity, were studied in Chapter 7 in the context of saturable waveguide arrays. We observed the continuation of linear vortex modes with topological charge  $S = 1$  and  $S = 2$  into the nonlinear regime, where different distributions of the amplitudes were found. Furthermore, we constructed closed families of discrete vortices located outside the linear bands. The special branching mechanisms leading to numerous simultaneous solutions with additional simultaneous stability, found for the family with  $c \geq 4$  and  $S = 1$ , were interpreted. Due to the saturable nature of the system the modes were more extended close to the bands and more localized far from them. The appearance of the existence of extra branches could be understood as the "continuation and multiplication" of the behavior found in other families, where we observed up to 4 simultaneously existing solutions.

For sure only some aspects of the physics of localized modes in nonlinear discrete systems were considered in this thesis and there remain many open questions. Along this thesis we considered only conservative systems, but including losses and gain certainly will make the picture more complete, rich and for sure is a wide field to explore. Also, taking into account correlations in the disorder gives rise to mobility edges and a partially delocalized spectrum and could show very interesting effects. Also, one interesting question could be, what happens to the pseudopotential landscapes, when an asymmetric and zero-mean driving potential is added.

## Bibliography

- [1] C. Denz, S. Flach, and Y.S. Kivshar (editors), "Nonlinearities in Periodic Structures and Metamaterials", Springer Series in Optical Sciences **150** (2010).
- [2] F. Lederer *et al.*, Phys. Rep. **463**, 1 (2008).
- [3] S. Flach and A.V. Gorbach, Phys. Rep. **467**, 1 (2008).
- [4] Y.V. Kartashov, V.A. Vysloukh, and L. Torner, Prog. Opt. **52**, 63 (2009).
- [5] U. Fano, Phys. Rev. **124**, 1866 (1961).
- [6] K. Kobayashi, H. Aikawa, S. Katsumoto, Y. Iye, Phys. Rev. Lett. **88**, 256806 (2002)
- [7] J. Gores, D. Goldhaber-Gordon, S. Heemeyer, M.A. Kastner, H.Shtrikman, D. Mahalu, and U. Meirav, Phys.Rev. B **62**, 2188 (2000).
- [8] C. Genet, M.P. van Exter, and J.P. Woerdman, Opt. Com. **225**, 331 (2003).
- [9] H. Schmidt, K.L. Campman, A.C. Gossard, A. Imamoglu, App. Phys. Lett. **70**, 3455 (1997).

- [10] E.Tekman, P.F. Bagwell, Phys.Rev. B **48**, 2553 (1993).
- [11] K. Kobayashi, H. Aikawa, A. Sano, S. Katsumoto, and Y. Iye, Y (Iye, Y), Phys.Rev. B **70**, 035319 (2004).
- [12] D.E. Nikonov, A. Imamoglu, R.O. Scully, and RO (Scully, RO), Phys.Rev. B **59**, 12212 (1999).
- [13] I.G. Zacharia, D. Goldhaber-Gordon, G. Granger, M.A. Kastner, Y.B. Khavin, H. Shtrikman, D. Mahalu, and U. Meirav, Phys.Rev. B **64**, 155311(2001).
- [14] S. Glutsch, U. Siegner, M.A. Mycek, and D.S. Chemla, PhysRevB **50**, 17009(1994).
- [15] C.P. Holfeld, F. Loser, M. Sudzius, K. Leo, D.M. Whittaker, K. Kohler, Phys. Rev. Lett.**81**, 874 (1998).
- [16] J. Kim, J.R. Kim, J.O. Lee, J.W. Park, H.M. So, N. Kim, K. Kang, K.H. Yoo, J.J. Kim, Phys. Rev. Lett.**90**, 166403 (2003).
- [17] A. Christ, Y. Ekinci, H.H. Solak, N.A. Gippius, S.G. Tikhodeev, and O.J.F, Phys. Rev. B **76** , 201405(2007).
- [18] A. E. Miroschnichenko, S. Flach, and Y. S. Kivshar, Rev. Mod. Phys. **82**, 2257 (2010).
- [19] A. E. Miroschnichenko, S. F. Mingaleev, S. Flach, and Y. S. Kivshar, Phys, Rev. E **71**, 036626 (2005).

- [20] A.E. Miroshnichenko, Y.S. Kivshar, R.A. Vicencio, and M.I. Molina, *Opt. Lett.* **30**, 872 (2005).
- [21] R.A. Vicencio, J. Brand, and S. Flach, *Phys. Rev. Lett.* **98**, 184102 (2007).
- [22] M. Kroner, A. O. Govorov, S. Remi, B. Biedermann, S. Seidl, A. Badolato, P. M. Petroff, W. Zhang, R. Barbour, B. D. Gerardot, R. J. Warburton, and K. Karrai, *Nature* **451**, 311 (2008).
- [23] H. Liu, G. X. Li, K. F. Li, S. M. Chen, S. N. Zhu, C. T. Chan, and K. W. Cheah, *Phys. Rev. B* **84**, 235437 (2011).
- [24] P.W. Anderson, *Phys. Rev.* **109**,1492(1958).
- [25] E. Abrahams, P.W. Anderson, D.C. Licciardello, and T.V. Ramakrishnan, *Phys. Rev. Lett.* **42** 673 (1979).
- [26] B. Deissler, M. Zaccantu, G. Roati, C. D'Errico, M. Fattori, M. Modugno, G. Modugno, and M. Inguscio, *Nature Physics* **6**, 354 (2010).
- [27] P. Sheng, *Introduction to Wave Scattering, Localization, and Mesoscopic Phenomena* (Springer, New York, 2006).
- [28] R.L. Weaver, *WaveMotion* **12**, 129 (1990).
- [29] R. Dalichaouch, J.P. Armstrong, S. Schulz, P.M. Platzman, and S.L. McCal, *Nature* **354**, 55 (1991).
- [30] R. Bruinsma and S. N. Coppersmith, *Phys. Rev. B* **33**, 6541 (1986).

- [31] J. Billy, V. Josse, Z. C. Zuo, A. Bernard, B. Hambrecht, P. Lugan, C. Clement, L. Sanchez-Palencia, and P. Bouyer, A. Aspect, *Nature* **453**, 891 (2008); L. Sanchez-Palencia and M. Lewenstein, *Nature Phys.* **6**, 87 (2010).
- [32] M.V. Ivanchenko, T.V. Lapyeva, and S. Flach, *Phys. Rev. Lett* **107**, 240602 (2011).
- [33] M.I. Molina, *Phys. Lett. A* **375**, 2056 (2011).
- [34] D.K.Campbell, S.Flach, Y.S. Kivshar, *Phys.. Today* **57**, 43-49 (2004).
- [35] F. Lederer, S. Darmanyan, A. Kobayakov, *Discrete Solitons: Spatial Solitons*, Eds.: S. Trillo, W.E. Torruelas (Springer-Verlag, Berlin 2001).
- [36] D.N.Christodoulides,R.I.Joseph, *Opt. Lett.* **13**, 794-796 (1988).
- [37] H.Eisenberg, Y.Silberberg, R.Morandotti, A.Boyd, J.Aitchison, *Phys. Rev. Lett.* **81**, 3383 (1998).
- [38] J. W. Fleischer, M. Segev, N. K. Efremidis, and D. N. Christodoulides, *Nature* **422**, 147 (2003).
- [39] Yu.S. Kivshar and D.K. Campbell, *Phys. Rev. E* **48**, 3077 (1993).
- [40] Lj. Hadžievski, A. Maluckov, M. Stepić, and D. Kip, *Phys. Rev. Lett.* **93**, 033901 (2004).
- [41] M. Stepić, D. Kip, Lj. Hadžievski, and A. Maluckov, *Phys. Rev. E* **69**, 066618 (2004).



- [42] A. Maluckov, M. Stepić, D. Kip, and Lj. Hadžievski, *Eur. Phys. J. B* **45**, 539 (2005); A. Maluckov, Lj. Hadžievski, and M. Stepić, *Physica D* **216**, 95 (2006).  
*Eur. Phys. J. B* **53**, 333 (2006).
- [43] A. Khare, K.Ø. Rasmussen, M.R. Samuelsen, and A. Saxena, *J. Phys. A* **38**, 807(2005); *ibid.* **42**, 085002 (2009); *ibid.* **43**, 375209 (2010).
- [44] J. Cuevas and J.C. Eilbeck, *Phys. Lett. A* **358**, 15 (2006).
- [45] T.R.O. Melvin, A.R. Champneys, P.G. Kevrekidis, and J. Cuevas, *Phys. Rev. Lett.* **97**, 124101 (2006); *Physica D* **237**, 551 (2008).
- [46] O.F. Oxtoby and I.V. Barashenkov, *Phys. Rev. E* **76**, 036603 (2007).
- [47] R.A. Vicencio and M. Johansson, *Phys. Rev. E* **73**, 046602 (2006).
- [48] T. Cretegny, Ph.D. thesis (in French), École Normale Supérieure de Lyon, 1998;  
S. Aubry, *Physica D* **216**, 1 (2006).
- [49] A. S. Desyatnikov, L. Torner, and Y. S. Kivshar, *Progr. in Optics* **47**, 1 (2005).
- [50] M. Johansson, S. Aubry, Y. B. Gaididei, P. L. Christiansen, K.O. Rasmussen, *Phys. D* **119**, 115 (1998).
- [51] B. A. Malomed, and P.G. Kevrekidis, *Phys. Rev. E* **64**, 026601 (2001).
- [52] J. Yang, and Z.H. Musslimani, *Opt. Lett.* **28**, 2094 (2003).
- [53] B.B. Baizakov, B.A. Malomed, and M. Salerno, *Europhys. Lett.* **63**, 642(2003).
- [54] D.N. Neshev T.J. Alexander, E.A. Ostrovskaya, Y.S. Kivshar, H. Martin, I. Makasyuk, and Z. Chen, *Phys. Rev. Lett* **92**, 123903 (2004).

- [55] J.W. Fleischer, G. Bartal, O. Cohen, O. Manela, M. Segev, J. Hudock, and D.N. Christodoulides, *Phys. Rev. Lett* **92**, 123904 (2004).
- [56] D.E. Pelinovsky, P.G. Kevrekidis, and D.J. Frantzeskakis, *Phys. D* **212**, 20(2005)
- [57] M. Öster, and M. Johansson, *Phys. Rev. E* **73**, 066608 (2006).
- [58] M.-A. García-March, A. Ferrando, M. Zacarés, S. Sahu, and D. E. Ceballos-Herrera, *Phys. Rev. A* **79**, 053820 (2009).
- [59] C. Mejía-Cortés, J. M. Soto-Crespo, M.I. Molina, and R.A. Vicencio, *Phys.Rev. A* **82**,063818 (2010).
- [60] K.J.H: Law, A. Saxena, P.G. Kevrekidis, and A.R. Bishop, *Phys. Rev. A* **82**, 035802 (2010).
- [61] Y. V. Kartashov, A. Ferrando, and M.-A. García-March, *Opt. Lett.* **32**, 2155 (2007).
- [62] P.G. Kevrekidis, H. Susanto, and Z. Chen , *Phys. Rev. E* **74**, 066606 (2006).
- [63] H. Susanto, K.J.H. Law, P.G. Kevrekidis , L. Tang, C. Lou, X. Wang, and Z. Chen, *Phys. D* **237**, 3123 (2008).
- [64] R.A. Vicencio, Ph.D. thesis (in Spanish), Universidad de Chile (2004).
- [65] M. Peccianti, K. A. Brzdakiewicz, and G. Assanto, *Opt. Lett.* **27**, 1460 (2002).
- [66] A. G. Litvak, V. A. Mironov, G. M. Fraiman, and A. D. Yunakovskii, *Sov. J. Plasma Phys.* **1**, 31 (1975).

- [67] A. V. Mamaev, A. A. Zozulya, V. K. Mezentsev, D. Z. Anderson, and M. Saffman, *Phys. Rev. A* **56**, R1110 (1997).
- [68] M. Öster, M. Johansson, and A. Eriksson, *Phys. Rev. E* **67**, 056606 (2003).
- [69] C. Weilmann, M. Ahles, J. Petter, D. Träger, J. Schröder, C. Denz, *Ann. Phys* **11**, 573-629 (2002).
- [70] D.N. Christodoulides, I.C. Khoo, G.J. Salamo, G.I. Stegeman, and E. W. Van Stryland, *Adv. in Opt.* **22**, 60 (2010).
- [71] N. Kukhtarev, V.B. Markov, S.G. Odulov, M.S. Soskin, V.L. Vinetskii, *Ferroelectrics* **22**, 949(1979).
- [72] S. Orlov, M. Segev, A. Yariv, and R.R. Neurgaonkar, *Opt. Lett.* **19**, 1293 (1995).
- [73] D.N.Christodoulides, M.I.Carvalho, *J. Opt. Soc. Am. B* **12**, 1628 (1995).
- [74] M.Segev, G.C.Valley, B.Crosignani, P.D.Porter, A.Yariv, *Phys. Rev. Lett.* **73**, 3211 (1994).
- [75] N.K. Efremidis, S. Sears, D.N. Christodoulides, J.W. Fleischer, and M. Segev, *Phys. Rev. E* **66**, 046602 (2002).
- [76] J.W. Fleischer, T. Carmon, M. Segev, N.K. Efremidis, and D.N. Christodoulides, *Phys. Rev. Lett.* **90**, 023902 (2003).
- [77] Z. Chen and K. McCarthy, *Opt. Lett.* **27**, 2019 (2002).

- [78] Z. Chen, K. MacCarthy and H. Martin, *Optics and Photonic News*, December 2002.
- [79] D. Neshev, Y. S. Kivshar, H. Martin, and Z. Chen, *Opt. Lett.* **29**, 486, (2004).
- [80] M. Petrovic, D. Träger, A. Strinic, M. Belic, J. Schröder, and C. Denz, *Phys. Rev. E* **68**, 055601 (2003).
- [81] J. Petter, J. Schröder, D. Träger, and C. Denz, *Optics Lett.* **28**, 438 (2003).
- [82] H. Trompeter, U. Peschel, T. Pertsch, F. Lederer, Tailoring guided modes in waveguide arrays, *Opt. Express* **11**, 3404(2003).
- [83] C. Zener, *Proc. R. Soc. Lond. A* **145**, 523 (1934).
- [84] C. Waschke, H. Roskos, R. Schwedler, K. Leo, H. Kurz, K. Köhler, *Phys. Rev. Lett.* **70**, 3319(1993).
- [85] U. Peschel, T. Pertsch, F. Lederer, *Opt. Lett.* **23**, 1701(1998).
- [86] G. Lenz, I. Talanina, C.M. de Sterke, *Phys. Rev. Lett.* **83**, 963 (1999).
- [87] H. Trompeter, T. Pertsch, F. Lederer, D. Michaelis, U. Streppel, A. Bräuer, U. Peschel, *Phys. Rev. Lett.* **96** 023901(2006).
- [88] H. Trompeter, W. Krolikowski, D.N. Neshev, A.S. Desyatnikov, A.A. Sukhorukov, Yu.S. Kivshar, T. Pertsch, U. Peschel, F. Lederer, *Phys. Rev. Lett.* **96**, 053903 (2006).
- [89] S. Longhi, M. Marangoni, M. Lobino, R. Ramponi, P. Laporta, E. Cianci, V. Foglietti, *Phys. Rev. Lett.* **96**, 243901(2006).

- [90] T. Pertsch, T. Zentgraf, U. Peschel, A. Brauer, and F. Lederer, *Phys. Rev. Lett.* **88**, 093901 (2002).
- [91] D.N. Christodoulides, F. Lederer, and Y. Silberberg, *Nature* **424**, 817 (2003).
- [92] N.K. Efremidis, D.N. Christodoulides, *Phys. Rev. A* **67**, 063608 (2003).
- [93] A. Szameit, T. Pertsch, F. Dreisow, S. Nolte, A. Tünnermann, U. Peschel, and F. Lederer, *Phys. Rev. A* **75**, 053814 (2007).
- [94] A.V. Savin, Y. Zolotaryuk and J.C. Eilbeck, *Physica D* **138**, 267 (2000).
- [95] T. Ahn, R.S. MacKay, and J.-A. Sepulchre, *Nonlinear Dynamics* **25**, 157 (2001).
- [96] R.S. MacKay and J.-A. Sepulchre, *J. Phys. A: Math. Gen.* **35**, 3985 (2002).
- [97] M.I. Molina, R.A. Vicencio, and Yu.S. Kivshar, *Opt. Lett.* **31**, 1693 (2006).
- [98] C.R. Rosberg, D.N. Neshev, W. Krolikowski, A. Mitchell, R.A. Vicencio, M.I. Molina, and Yu.S. Kivshar, *Phys. Rev. Lett.* **97**, 083901 (2006).
- [99] W.H. Press, *Numerical recipes*, Second edition, Cambridge Press (1988).
- [100] K.M. Davis, K. Miura, N. Sugimoto, and K. Hirao, *Opt. Lett.* **21**, 1729(1996).
- [101] K. Itoh, W. Watanabe, S. Nolte, and C.B. Schaffer *MRS Bulletin* **31**, 620 (2006).
- [102] A. Szameit, D. Blomer, J. Burghoff, T. Schreiber, T. Pertsch, S. Nolte, A. Tünnermann, and F. Lederer, *Opt. Exp.* **13**, 10552 (2005).

- [103] A. Szameit, F. Dreisow, T. Pertsch, S. Nolte, and A. Tuennermann, *Opt. Exp.* **15**, 1579 (2006).
- [104] A. Szameit and S. Nolte, *J. Phys. B* **43**, 163001 (2010).
- [105] D. R. Smith, W. J. Padilla, D. C. Wier, S. C. Nemat Nasser, S. Schultz, *Phys. Rev. Lett.* **84**, 4184 (2000).
- [106] J. B. Pendry, *Phys. Rev. Lett.* **85**, 3966 (2000).
- [107] S. Linden, C. Enkrich, G. Dolling, M. W. Klein, J. Zhou, T. Koschny, C. M. Soukoulis, S. Burger, F. Schmidt, and M. Wegener, *IEEE J. Sel. Top. Quant. Electron.* **12**, 1097 (2006); T. J. Yen, W. J. Padilla, N. Fang, D. C. Vier, D. R. Smith, J. B. Pendry, D. N. Basov, and X. Zhang, *Science* **303**, 1494 (2004).
- [108] M. Gorkunov, M. Lapine, E. Shamonina, K.H. Ringhofer, *Eur. Phys. J. B* **28**, 263 (2002).
- [109] M.C.K. Wiltshire, E. Shamonina, I.R. Young, L. Solymar, *Electron. Lett.* **39**, 215 (2003).
- [110] R.R.A. Syms, E. Shamonina, V. Kalinin, L. Solymar, *J. Appl. Phys.* **97**, 64909 (2005).
- [111] E. Shamonina, V.A. Kalinin, K.H. Ringhofer, L. Solymar, *J. Appl. Phys.* **92**, 6252 (2002).
- [112] E. Shamonina, L. Solymar, *J. Phys. D-Appl. Phys.* **37**, 362 (2004).

- [113] M.J. Freire, R. Marques, F. Medina, M.A.G. Laso, F. Martin, *Appl. Phys. Lett.* **85**, 4439 (2004).
- [114] I. V. Shadrivov, A. N. Reznik and Y. S. Kivshar, *Physics B* **394**, 180 (2007).
- [115] R.R.A. Syms, E. Shamonina and L. Solymar, *IEE Proc.-Microw. Antennas Propag.*, **153**, 111 (2006).
- [116] E. Smirnov *et al.*, *Opt. Exp.* **14**, 11248 (2006).
- [117] M. Stepic *et al.*, *Phys. Rev. E* **74**,046614 (2006).
- [118] S. John, *Phys. Rev. Lett.***53**, 2169(1984).
- [119] V.D. Freilikher, S.A. Gredeskul, *Prog. Opt.* **30** ,137 (1992).
- [120] D.S. Wiersma, P. Bartolini, A. Legendijk, R. Righini, *Nature***390**, 671(1997).
- [121] T. Schwartz, G. Bartal, S. Fishman, M. Segev, *Nature* **446**, 52 (2007).
- [122] Y. Lahini, A. Avidan, F. Pozzi, M. Sorel, R. Morandotti, D.N. Christodoulides, Y. Silberberg, *Phys. Rev. Lett.***100**, 013906 (2008).
- [123] A. Szameit, Y. V. Kartashov, P. Zeil, F. Dreisow, M. Heinrich, R. Keil, S. Nolte, A. Tünnermann, V. A. Vysloukh, and L. Torner , *Opt. Lett.* **35**, 1172 (2010).
- [124] B. Kramer, A. MacKinnon, *Rep.Prog.Phys* **56**,1469 (1993).
- [125] L. Martin, G. Di Giuseppe, A. Perez-Leija, R. Keil, F. Dreisow, M. Heinrich, S. Nolte, A. Szameit, A.F. Abouraddy, D.N. Christodoulides, and B.E.A. Saleh, *Opt. Express* **19**, 13636 (2011).

- [126] A. García-Martín, J.A. Torres, J.J. Sáenz, and M. Nieto.Vesperinas, Appl. Phys. Lett. **71**, 1912 (1997).
- [127] A. García-Martín, J.A. Torres, J.J. Sáenz, and M. Nieto.Vesperinas, Phys. Rev. Lett. **80**, 4165 (1999).
- [128] A. García-Martín, J.J. Sáenz, and M. Nieto.Vesperinas, Phys. Rev. Lett. **84**, 3578 (2000).
- [129] V.D. Freilikher, N.M. Makarov, and I.V. Yurkevich, Phys. Rev. B **41**, 8033 (1990).
- [130] J.A. Sánchez-Gil, V.D. Freilikher, I.V. Yurkevich, and A.A. Maradudin, Phys. Rev. Lett. **80**, 948 (1998).
- [131] J.A. Sánchez-Gil, V.D. Freilikher, A.A. Maradudin, and I.V. Yurkevich, Phys. Rev. B **59**, 5915 (1999).
- [132] M. Rendón, N. M. Makarov, F. M. Izrailev, Phys. Rev. E **83**, 051124 (2011).
- [133] Yu. S. Kivshar *et al.*, Phys. Rev. Lett. **64**, 1693 (1990).
- [134] M. I. Molina, Phys. Rev. B **58**, 12547 (1998).
- [135] G. Kopidakis and S. Aubry, Phys. Rev. Lett. **100**, 084103 (2008).
- [136] G. Kopidakis *et al.*, Phys. Rev. Lett. **100**, 084103 (2008).
- [137] A. S. Pikovsky and D. L. Shepelyansky, Phys. Rev. Lett. **100**, 094101 (2008).
- [138] S. Flach, D. O. Krimer, and Ch. Skokos, Phys. Rev. Lett. **102**, 024101 (2009).



- [139] S. Fishman, Y. Krivolapov, and A. Soffer, *Nonlinearity* **25**, R53-R72 (2012).
- [140] T. Pertsch, U. Peschel, J. Kobelke, K. Schuster, H. Bartelt, S. Nolte, A. Tünnermann, and F. Lederer, *Phys. Rev. Lett* **93**, 053901 (2004).
- [141] S. Flach, *Phys. Part. Nucl.* **41**, 1020 (2010).
- [142] L. Levi, M. Rechtsman, B. Freedman, T. Schwartz, O. Manela, and M. Segev, *Science* **332**, 1541 (2011).
- [143] D. Weaire and A.R. Williams, *J. Phys. C: Solid State Phys.* **10**, 1239 (1977).
- [144] R.A. Vicencio and S. Flach, *Phys. Rev. E* **79**, 016217 (2009).
- [145] D. N. Christodoulides and R. I. Joseph, *Opt. Lett.* **13**, 794 (1988).
- [146] M. I. Molina and G. P. Tsironis, *Physica D* **65**, 267 (1993).
- [147] S. Longhi, *Phys. Rev. A* **79**, 033847 (2009).
- [148] F. M. Izrailev, T. Kottos, A. Politi, and G. P. Tsironis, *Phys. Rev. E* **55**, 4951 (1997).
- [149] S. Stützer, Y. V. Kartashov, V. A. Vysloukh, A. Tünnermann, S. Nolte, M. Lewenstein, L. Torner, and A. Szameit, *Opt. Lett.* **37**, 1715 (2012).
- [150] M.I. Molina, R.A. Vicencio, and Y.S. Kivshar, *Phys. Lett. A* **350**, 134 (2006).
- [151] U. Peschel, R. Morandotti, J.M. Arnold, J.S. Aitchison, H.S. Eisenberg, Y. Silberberg, T. Pertsch, and F. Lederer, *Jour. Opt. Soc. Am. B* **19**, 2637 (2003).
- [152] R.A. Vicencio, M.I. Molina, and Yu.S. Kivshar, *Opt. Lett.* **28**, 1942 (2003).

- [153] S. Aubry and T. Cretegny, *Physica D* **119**, 1 (1998).
- [154] A. Khare, K.Ø. Rasmussen, M.R. Samuelsen, and A. Saxena, *J. Phys. A* **38**, 807 (2005).
- [155] D.N. Christodoulides and R.I. Joseph, *Opt. Lett.* **13**, 794 (1988).
- [156] J.C. Eilbeck and M. Johansson, in *Localization and Energy Transfer in Nonlinear Systems*, Proceedings of the Third Conference, San Lorenzo de El Escorial Madrid, edited by L. Vázquez, R.S. MacKay, and M.P. Zorzano (World Scientific, Singapore, 2003), p.44.
- [157] V.M. Rothos, H.E. Nistazakis, P.G. Kevrekidis, and D.J. Frantzeskakis, *J. Phys. A* **42**, 025207 (2009).
- [158] P.G. Kevrekidis, K.Ø. Rasmussen, and A.R. Bishop, *Phys. Rev. E* **61**, R2006 (2000).
- [159] M. Peyrard and M. Remoissenet, *Phys. Rev. B* **26**, 2886 (1982).
- [160] C. Chong, R. Carretero-González, B.A. Malomed, and P.G. Kevrekidis, *Physica D* **238**, 126 (2009).
- [161] M. Öster and M. Johansson, *Physica D* **238**, 88 (2009).
- [162] H. Susanto, P.G. Kevrekidis, R. Carretero-González, B.A. Malomed, and D.J. Frantzeskakis, *Phys. Rev. Lett.* **99**, 214103 (2007).
- [163] G. Kalosakas, *Physica D* **216**, 44 (2006).
- [164] U. Naether, R.A. Vicencio, and M. Johansson, *Phys. Rev. E* **83** (2011).

- 
- [165] C. Mejía-Cortés, J. M. Soto-Crespo, M.I. Molina, and R.A. Vicencio, Phys.Rev. A **83**, 043837 (2011).
- [166] D. Leykam, A. S. Desyatnikov, Opt. Lett. **36**, 4806 (2011).
- [167] J. Wang, and J. Yang, Phys. Rev. A **77**, 033834 (2008).
- [168] J. Stockhofe, P. G. Kevrekidis, P. Schmelcher, "Existence, stability and non-linear dynamics of vortices and vortex clusters in anisotropic Bose-Einstein condensates" in Springer Series, Progress in Optical Science and Photonics, Editor B. Malomed, (2012).
- [169] C.R.Menyuk, Physica D **11**, 109(1984).
- [170] G. Benettin, and A. Giorgilli, J. Stat. Phys. **74**, 1117 (1994).
- [171] E. Hairer, and Ch. Lubich, Numer. Math. **76**, 441(1997).

## A. Multidimensional Newton Raphson

In one dimension, the Newton-Raphson method [99] consists in the following steps, when searching for the roots of a function located in the neighborhood to the starting guess (seed)  $x$ :

$$\begin{aligned} 0 &= f(x + \delta) = f(x) + f'(x)\delta + \frac{f''(x)}{2}\delta^2 + \dots \\ \Rightarrow \delta &\approx -\frac{f(x)}{f'(x)}. \end{aligned}$$

Thus, one iteration step consist in calculating

$$x_{i+1} = x_i - \frac{f(x_i)}{f'(x_i)}. \quad (\text{A.1})$$

This method is a very useful tool, because its convergency is quadratic and therefore faster than other methods[99], provided that the derivative of the function is analytically known and does not vanish in the roots. The main drawback is, that it gives no guarantee of convergency, the seed has to be close to the root.

The generalization to a multidimensional setting with a vectorial seed  $\mathbf{x}$  is straightforward:

$$\begin{aligned}
0 &= \mathbf{f}(\mathbf{x} + \delta) \approx \mathbf{f}(\mathbf{x}) + \mathbf{J}(\mathbf{x})\delta \\
\Rightarrow \delta &\approx -\mathbf{J}^{-1}(\mathbf{x})\mathbf{f}(\mathbf{x}) \\
\mathbf{x}_{i+1} &= \mathbf{x}_i - \mathbf{J}^{-1}(\mathbf{x}_i)\mathbf{f}(\mathbf{x}_i),
\end{aligned} \tag{A.2}$$

with the Jacobian matrix

$$J = \begin{pmatrix} \frac{\partial f_1}{\partial x_1} & \dots & \frac{\partial f_1}{\partial x_n} \\ \vdots & \ddots & \vdots \\ \frac{\partial f_m}{\partial x_1} & \dots & \frac{\partial f_m}{\partial x_n} \end{pmatrix} \tag{A.3}$$

In sets of DNLS equations, the Jacobian is analytical and in general non singular, so we can use the Newton-Raphson method to find stationary solutions. For example, it is more convenient in a cubic DNLS to start with a seed in the anti-continuous (high-power) limit, where the initial seed is expected to be more similar to the actual solution. Once found one solution, the power or nonlinearity can be slightly changed, to continue the solution branch to more extended solution, which for example can be found close to the band edges.

## B. Finding the Hamiltonian for the symplectic integrator

Symplectic integrators are a very useful tool in the long-time integration of conservative Hamiltonian systems, since they conserve the phase-space volume (symplectic manifold) and thus the energy. General numerical methods such as the ordinary Runge-Kutta methods [99] can introduce non-Hamiltonian perturbations leading to the introduction of an artificial dissipation term caused only by the numerical integrator. Because of this problem methods of symplectic integration for Hamiltonian systems were introduced, which do preserve the features of the Hamiltonian structure by doing canonical or symplectic transformation in each integration step [169, 170, 171]. They are especially used in long-term integrations of Hamiltonian systems like In DNLS lattices with disorder and nonlinearity [138].

We used a symplectic Runge-Kutta integrator implemented in *Mathematica* for separable Hamiltonian systems of the form  $H(p, q) = T(p) + V(q)$ , which asks for the canonical equations. Therefore it is necessary to find an Hamiltonian for the problem of coupled SRR described in Sec. 4.1. Following any classical mechanics textbook

procedure, we start with the Lagrangian

$$L = T - V \quad (\text{B.1})$$

$$= \frac{1}{2} \sum_n^N [\dot{q}_n^2 - q_n^2] + \sum_n^{N-1} \lambda \dot{q}_n \lambda \dot{q}_{n+1}, \quad (\text{B.2})$$

to derive the equation for the canonical momentum

$$p_n = \frac{\partial L}{\partial \dot{q}_n} = \dot{q}_n + \lambda[\dot{q}_{n+1} + \dot{q}_{n-1}]. \quad (\text{B.3})$$

We can express this equation set more compact, using  $\vec{P} = p_n$  and  $\vec{Q} = \dot{q}_n$  and the matrix

$$\mathbf{M} = \begin{pmatrix} 1 & \lambda & 0 & \dots & \dots & \dots & \dots \\ \lambda & 1 & \lambda & 0 & \dots & \dots & \dots \\ 0 & \lambda & 1 & \lambda & 0 & \dots & \dots \\ \dots & 0 & \lambda & 1 & \lambda & 0 & \dots \\ \ddots & \ddots & \ddots & \ddots & \ddots & \ddots & \ddots \\ \dots & \dots & \dots & \dots & 0 & \lambda & 1 \end{pmatrix}. \quad (\text{B.4})$$

This leads to the expression

$$\vec{P} = \mathbf{M} \cdot \vec{Q} \Rightarrow \vec{Q} = \mathbf{M}^{(-1)} \cdot \vec{P} \quad \text{and} \quad \dot{q}_n \equiv f_n(\vec{P})$$

The inverse of  $\mathbf{M}$  in this case has to be obtained numerically. The separable Hamiltonian is then defined as

$$\begin{aligned}
H &= \sum_n \dot{q}_n p_n - L \\
&= \vec{Q} \cdot \vec{P} - \frac{1}{2} \vec{Q} \cdot \vec{Q} + \frac{1}{2} \vec{Q} \cdot \vec{Q} - \lambda \sum_n^{N-1} \dot{q}_n \dot{q}_{n+1} \\
&= \mathbf{M}^{(-1)} |\vec{P}|^2 - \frac{1}{2} |\mathbf{M}^{(-1)} \vec{P}|^2 + \frac{1}{2} |\vec{Q}|^2 - \lambda \sum_n^{N-1} f_n(\vec{P}) f_{n+1}(\vec{P}) \\
H &= \frac{1}{2} \sum_n \left[ 2f_n(\vec{P}) p_n - f_n(\vec{P})^2 + q_n^2 \right] - \lambda \sum_n^{N-1} f_n(\vec{P}) f_{n+1}(\vec{P}). \quad (\text{B.5})
\end{aligned}$$

Once this equation set is obtained for any specific lattice geometry, it can be implemented and integrated with better control of the error and more stable than using an ordinary Runge-Kutta integrator.



## C. Fs-laser written waveguides

When ultrashort laser pulses are tightly focused into glasses, permanent refractive index changes can be achieved [100]. When the intensity in the focal region becomes high enough, multi-photon absorption and tunneling ionization in addition with an ionization avalanche can lead to the formation of a localized plasma and initiate the rearrangement of the network structure [101, 102]. To produce the waveguide arrays, a Ti:sapphire laser system (RegA/Mira, Coherent Inc.) with a repetition rate of 100 kHz and a pulse duration of about 150 fs at a wavelength of  $\lambda = 800$  nm is used. The beam is focused into a polished fused-silica sample using a  $20\times$  microscope objective with a numerical aperture of 0.45, a sketch of the writing process is shown in Fig. C.1(a). A high precision positioning system (ALS 130, Aerotech) allows for the control of the positions of individual waveguides as well as the writing velocities. Each guide has dimensions of  $4 \times 12 \mu\text{m}^2$  and exhibits a refractive index increase of  $\approx 5 \times 10^{-4}$ [103, 104], as shown in Fig. C.1(c). The nearfield of an exemplary mode is shown in Fig. C.1(b).

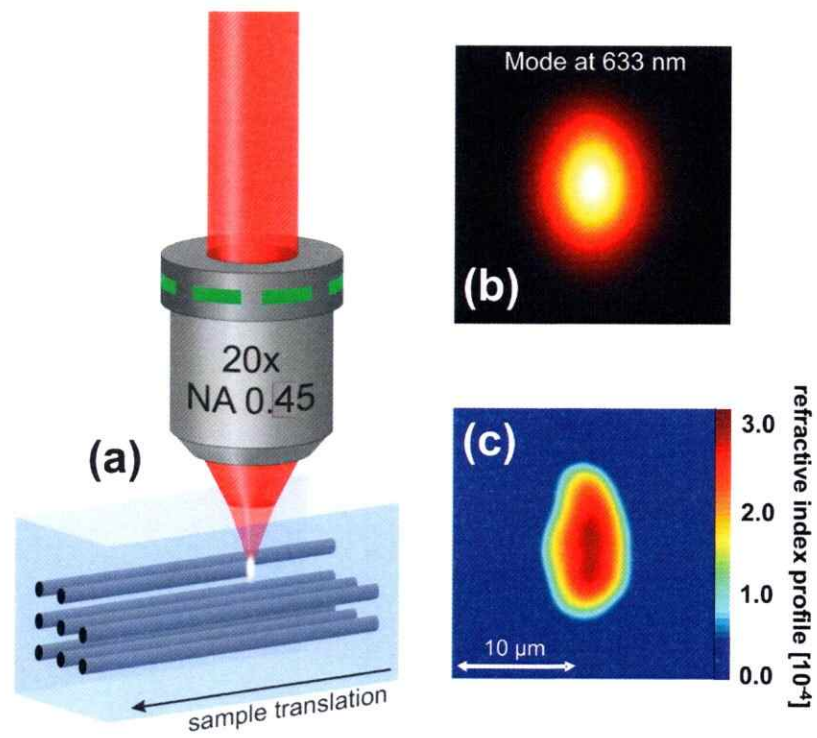


Figure C.1.: Sketch of the fs-laser writing process

## D. Publications

September 15, 2009 / Vol. 34, No. 18 / OPTICS LETTERS 2721

## Fano resonances in waveguide arrays with saturable nonlinearity

Uta Naether,\* Daniel E. Rivas, Manuel A. Larenas, Mario I. Molina, and Rodrigo A. Vicencio  
*Departamento de Física, Facultad de Ciencias, and Centro de Óptica y Fotónica (CEFOP), Universidad de Chile,  
Casilla 653, Santiago, Chile*

\*Corresponding author: unaether@u.chile.cl

Received May 21, 2009; revised July 27, 2009; accepted July 29, 2009;  
posted August 18, 2009 (Doc. ID 111749); published September 4, 2009

We study a waveguide array with an embedded nonlinear saturable impurity. We solve the impurity problem in closed form and find the nonlinear localized modes. Next, we consider the scattering of a small-amplitude plane wave by a nonlinear impurity mode, and discover regions in parameter space where transmission is fully suppressed. We relate these findings with Fano resonances and propose this setup as a means to control the transport of light across the array. © 2009 Optical Society of America

OCIS codes: 190.0190, 190.5530, 190.6135, 230.4320.

PHYSICAL REVIEW E 83, 036601 (2011)

## Peierls-Nabarro energy surfaces and directional mobility of discrete solitons in two-dimensional saturable nonlinear Schrödinger lattices

Uta Naether,<sup>1,2</sup> Rodrigo A. Vicencio,<sup>1,2</sup> and Magnus Johansson<sup>3,\*</sup>

<sup>1</sup>*Departamento de Física, Facultad de Ciencias, Universidad de Chile, Santiago, Chile*

<sup>2</sup>*Center for Optics and Photonics, Universidad de Concepción, Casilla 4016, Concepción, Chile*

<sup>3</sup>*Department of Physics, Chemistry and Biology, Linköping University, SE-581 83 Linköping, Sweden*

(Received 8 October 2010; published 7 March 2011)

We address the problem of directional mobility of discrete solitons in two-dimensional rectangular lattices, in the framework of a discrete nonlinear Schrödinger model with saturable on-site nonlinearity. A numerical constrained Newton-Raphson method is used to calculate two-dimensional Peierls-Nabarro energy surfaces, which describe a pseudopotential landscape for the slow mobility of coherent localized excitations, corresponding to continuous phase-space trajectories passing close to stationary modes. Investigating the two-parameter space of the model through independent variations of the nonlinearity constant and the power, we show how parameter regimes and directions of good mobility are connected to the existence of smooth surfaces connecting the stationary states. In particular, directions where solutions can move with minimum radiation can be predicted from flatter parts of the surfaces. For such mobile solutions, slight perturbations in the transverse direction yield additional transverse oscillations with frequencies determined by the curvature of the energy surfaces, and with amplitudes that for certain velocities may grow rapidly. We also describe how the mobility properties and surface topologies are affected by inclusion of weak lattice anisotropy.

DOI: 10.1103/PhysRevE.83.036601

PACS number(s): 05.45.Yv, 42.65.Wi, 63.20.Pw, 63.20.Ry

April 15, 2011 / Vol. 36, No. 8 / OPTICS LETTERS 1467

## Mobility of high-power solitons in saturable nonlinear photonic lattices

Uta Naether,<sup>1,2,\*</sup> Rodrigo A. Vicencio,<sup>1,2</sup> and Milutin Stepić<sup>3</sup><sup>1</sup>*Departamento de Física, Facultad de Ciencias, Universidad de Chile, Casilla 653, Santiago, Chile*<sup>2</sup>*Center for Optics and Photonics, Universidad de Concepción, Casilla 4016, Concepción, Chile*<sup>3</sup>*Vinča Institute of Nuclear Sciences, University of Belgrade, P.O.B. 522, 11001 Belgrade, Serbia*

\*Corresponding author: unaether@u.uchile.cl

Received January 27, 2011; accepted March 5, 2011;

posted March 24, 2011 (Doc. ID 141866); published April 15, 2011

We theoretically study the properties of one-dimensional nonlinear saturable photonic lattices exhibiting multiple mobility windows for stationary solutions. The effective energy barrier decreases to a minimum in those power regions where a new intermediate stationary solution appears. As an application, we investigate the dynamics of high-power Gaussian-like beams finding several regions where the light transport is enhanced. © 2011 Optical Society of America

OCIS codes: 190.0190, 190.5330, 190.6135, 230.4320.

PHYSICAL REVIEW A 84, 043808 (2011)

### Fano resonances in magnetic metamaterials

Uta Naether and Mario I. Molina

*Departamento de Física, Facultad de Ciencias, Universidad de Chile, Casilla 653, Santiago, Chile and  
Center for Optics and Photonics (CEFOP), Casilla 4016, Concepción, Chile*

(Received 3 March 2011; revised manuscript received 8 August 2011; published 5 October 2011)

We study the scattering of magnetoinductive plane waves by internal (external) capacitive (inductive) defects coupled to a one-dimensional split-ring resonator array. We examine a number of simple defect configurations where Fano resonances occur and study the behavior of the transmission coefficient as a function of the controllable external parameters. We find that for embedded capacitive defects, the addition of a small amount of coupling to second neighbors is necessary for the occurrence of Fano resonance. For external inductive defects, Fano resonances are commonplace, and they can be tuned by changing the relative orientation or distance between the defect and the SSR array.

DOI: 10.1103/PhysRevA.84.043808

PACS number(s): 42.25.Bs, 42.70.-a, 78.67.Pt, 78.20.Bh

February 15, 2012 / Vol. 37, No. 4 / OPTICS LETTERS 485

## Anderson localization in a periodic photonic lattice with a disordered boundary

U. Naether<sup>1,2,3</sup>, J. M. Meyer<sup>3</sup>, S. Stützer<sup>3</sup>, A. Tünnermann<sup>3</sup>, S. Nolte<sup>3</sup>, M. I. Molina<sup>1,2</sup>, and A. Szameit<sup>3</sup><sup>1</sup>*Departamento de Física, Facultad de Ciencias, Universidad de Chile, Santiago, Chile*<sup>2</sup>*Center for Optics and Photonics (CEFOP), Casilla 4016, Concepción, Chile*<sup>3</sup>*University Jena, Institute of Applied Physics, D-07743 Jena, Germany**\*Corresponding author: unaether@u.uchile.cl*Received October 17, 2011; accepted December 9, 2011;  
posted December 13, 2011 (Doc. ID 156537); published February 6, 2012

We investigate experimentally the light evolution inside a two-dimensional finite periodic array of weakly coupled optical waveguides with a disordered boundary. For a completely localized initial condition away from the surface, we find that the disordered boundary induces an asymptotic localization in the bulk, centered around the initial position of the input beam. © 2012 Optical Society of America

OCIS codes: 130.2790, 240.6700, 290.5825.

February 15, 2012 / Vol. 37, No. 4 / OPTICS LETTERS 693

## Observation of the gradual transition from one-dimensional to two-dimensional Anderson localization

U. Naether,<sup>1,2\*</sup> Y. V. Kartashov,<sup>3,4</sup> V. A. Vysloukh,<sup>5</sup> S. Nolte,<sup>6</sup> A. Tünnermann,<sup>6</sup> L. Torner,<sup>2</sup> and A. Szameit<sup>6,\*</sup><sup>1</sup>*Departamento de Física, Facultad de Ciencias, Universidad de Chile, Santiago, Chile*<sup>2</sup>*Center for Optics and Photonics (CEFOP), Casilla 4016, Concepción, Chile*<sup>3</sup>*ICFO-Institut de Ciències Fotoniques, and Universitat Politècnica de Catalunya, Mediterranean Technology Park, 08860 Castelldefels (Barcelona), Spain*<sup>4</sup>*Institute of Spectroscopy, Russian Academy of Sciences, Troitsk, Moscow Region 142190, Russia*<sup>5</sup>*Departamento de Física y Matemáticas, Universidad de las Américas—Puebla, 72820 Puebla, Mexico*<sup>6</sup>*Institute of Applied Physics, Friedrich-Schiller-Universität Jena, Max-Wien-Platz 1, 07743 Jena, Germany**\*Corresponding author: szameit@iap.uni-jena.de*Received November 28, 2011; accepted December 23, 2011;  
posted January 3, 2012 (Doc. ID 159020); published February 9, 2012

June 1, 2012 / Vol. 37, No. 11 / OPTICS LETTERS 1865

## Nonlinear localized modes in Glauber–Fock photonic lattices

A. J. Martínez,<sup>1,2,\*</sup> U. Naether,<sup>1,2</sup> A. Szameit,<sup>3</sup> and R. A. Vicencio<sup>1,2</sup><sup>1</sup>*Departamento de Física and MSI-Nucleus on Advanced Optics, Facultad de Ciencias, Universidad de Chile, Santiago, Chile*<sup>2</sup>*Center for Optics and Photonics (CEFOP), Casilla 4016, Concepción, Chile*<sup>3</sup>*Institute of Applied Physics, Friedrich-Schiller-Universität Jena, Max-Wien-Platz 1, 07743 Jena, Germany*\*Corresponding author: [amartinez@cefop.cl](mailto:amartinez@cefop.cl)Received January 18, 2012; revised March 27, 2012; accepted March 27, 2012;  
posted March 28, 2012 (Doc. ID 161786); published May 21, 2012

We study a nonlinear Glauber–Fock lattice and the conditions for the excitation of localized structures. We investigate the particular linear properties of these lattices, including linear localized modes. We investigate numerically nonlinear modes centered in each site of the lattice. We found a strong disagreement of the general tendency between the stationary and the dynamical excitation thresholds. We define a new parameter that takes into account the stationary and dynamical properties of localized excitations. © 2012 Optical Society of America

OCIS codes: 190.0190, 190.5530, 190.6135, 230.4320.

## Disorder-enhanced nonlinear delocalization in segmented waveguide arrays

Matthias Heinrich<sup>1,4</sup>, Robert Keil<sup>1</sup>, Yoav Lahini<sup>2</sup>, Uta Naether<sup>3</sup>,  
Felix Dreisow<sup>1</sup>, Andreas Tünnermann<sup>1</sup>, Stefan Nolte<sup>1</sup>  
and Alexander Szameit<sup>1</sup>

<sup>1</sup> Institute of Applied Physics, Abbe Center of Photonics,  
Friedrich-Schiller-Universität, Max-Wien-Platz 1, 07743 Jena, Germany

<sup>2</sup> Department of Physics of Complex Systems, The Weizmann Institute of  
Science, Rehovot 76100, Israel

<sup>3</sup> Departamento de Física, Center for Optics and Photonics (CEFOP), and  
MSI-Nucleus on Advanced Optics, Facultad de Ciencias, Universidad de Chile,  
Santiago, Chile

E-mail: p2hema@googlemail.com

*New Journal of Physics* 14 (2012) 073026 (10pp)

Received 30 April 2012

Published 12 July 2012

Online at <http://www.njp.org/>

doi:10.1088/1367-2630/14/7/073026

**Abstract.** Nonlinearity and disorder in discrete systems give rise to fascinating dynamics in various fields of physics. Photonic lattices allow investigation of them in an optical context. The very nature of discrete propagation allows perfect reconstruction of arbitrary initial wave packets by introducing phase shifts to specific lattice sites. We investigate, both numerically and experimentally, the interplay of nonlinearity with this so-called segmentation imaging in the presence of disorder. We find that whereas in the linear regime perfect imaging is achieved for arbitrary amounts of coupling disorder, the onset of nonlinear self-focusing generally destroys imaging. Interestingly, the influence of Anderson localization in strongly disordered lattices renders the imaging significantly more susceptible to nonlinear perturbations.



Submitted or to be submitted (2012)

**Experimental observation of super-diffusive transport in random dimer lattices**U. Naether<sup>1,\*</sup>, S. Stützer<sup>2,\*</sup>, R. Vicencio<sup>1</sup>, M. Molina<sup>1</sup>, A. Tünnermann<sup>2</sup>,  
S. Nolte<sup>2</sup>, T. Kottos<sup>3</sup>, D. Christodoulides<sup>4</sup>, and A. Szameit<sup>2</sup><sup>1</sup>*Departamento de Física, MSI-Nucleus on Advanced Optics,  
and Center for Optics and Photonics (CEFOP),  
Facultad de Ciencias, Universidad de Chile, Santiago, Chile*<sup>2</sup>*Institute of Applied Physics, Abbe Center of Photonics,  
Friedrich-Schiller-Universität Jena, Max-Wien-Platz 1, 07743 Jena, Germany*<sup>3</sup>*Department of Physics, Wesleyan University, Middletown, Connecticut 06459, USA*<sup>4</sup>*CREOL, The College of Optics & Photonics, University of Central Florida, Orlando, FL 32816, USA and*  
\* *these authors contributed equally*

(Dated: October 15, 2012)

We experimentally observe anomalous wavepacket evolution in a realization of a one-dimensional finite binary Anderson model in the presence of short-range correlations. To this end, we employ weakly-coupled optical waveguides with propagation constants  $\epsilon_1$  and  $\epsilon_2$ . The correlations enforce the creation of dimers, i.e., two adjacent waveguides with the same  $\epsilon$ , randomly placed along the lattice. A transition from a ballistic to a super-diffusive wavepacket expansion and, eventually, to localization is observed as the contrast between the two propagation constants increases.

PACS numbers: 42.82.Et, 42.25.Bs, 11.30.Er

**Enhanced distribution of a wave-packet in lattices with disorder and nonlinearity**Uta Naether<sup>1</sup>, Santiago Rojas-Rojas<sup>1</sup>, Alejandro J. Martínez<sup>1</sup>, Simon  
Stützer<sup>2</sup>, Andreas Tünnermann<sup>2</sup>, Stefan Nolte<sup>2</sup>, Mario I. Molina<sup>1</sup>,  
Rodrigo A. Vicencio<sup>1</sup>, and Alexander Szameit<sup>2</sup><sup>1</sup>*Departamento de Física, MSI-Nucleus on Advanced Optics, and Center for Optics and  
Photonics (CEFOP), Facultad de Ciencias, Universidad de Chile, Santiago, Chile*<sup>2</sup>*Institute of Applied Physics, Friedrich-Schiller-Universität Jena, Max-Wien-Platz 1, 07743  
Jena, Germany*[unaether@u.uchile.cl](mailto:unaether@u.uchile.cl)

**Abstract:** We show, numerically and experimentally, that the presence of weak disorder results in an enhanced energy distribution of an initially localized wave-packet, in one- and two-dimensional finite lattices. The addition of a focusing nonlinearity facilitates the spreading effect even further by increasing the wave-packet effective size. We find a clear transition between the regions of enhanced spreading (weak disorder) and localization (strong localization).

© 2012 Optical Society of America

OCIS codes: (070.7345) Wave propagation; (130.2790) Guided waves; (190.0190) Nonlinear Optics.

### Self-trapping transition in nonlinear cubic lattices

Uta Naether, Alejandro J. Martínez, Diego Guzmán-Silva, Mario I. Molina, and Rodrigo A. Vicencio  
*Departamento de Física, MSI-Nucleus on Advanced Optics,  
and Center for Optics and Photonics (CEFOP),  
Facultad de Ciencias, Universidad de Chile, Santiago, Chile*  
(Dated: October 15, 2012)

We explore the fundamental question about the critical nonlinearity value needed to dynamically localize energy in diverse discrete nonlinear (Kerr) lattices. A simple criterium is developed - for the case of an initially localized excitation - that defines the transition regions in parameter space ("dynamical tongues") from a delocalized to a localized profile. An estimate of the critical nonlinearity value for which this transition occurs is obtained with numerical computations performed in one-, two-, and three-dimensional nonlinear lattices. We discuss the validity and possible extensions of this criterium to more complex lattices.

PACS numbers: 42.25.Dd, 42.65.Tg, 72.15.Rn

### Existence of intermediate solutions in a saturable nonlinear coupler

Diego Guzmán-Silva<sup>1</sup>, Cibo Lou<sup>2</sup>, Uta Naether<sup>1</sup>, Christian E. Rüter<sup>2</sup>, Detlef Kip<sup>2</sup> and Rodrigo A. Vicencio<sup>1</sup>  
<sup>1</sup>*Departamento de Física, MSI-Nucleus on Advanced Optics,  
and Center for Optics and Photonics (CEFOP),  
Facultad de Ciencias, Universidad de Chile, Santiago, Chile and*  
<sup>2</sup>*Faculty of Electrical Engineering, Helmut Schmidt University, 22043 Hamburg, Germany*  
(Dated: October 3, 2012)

We show, theoretically and experimentally, the existence of intermediate modes in a nonlinear saturable coupler. In spite of its simplicity, we found that this model shows generic and fundamental properties of saturable lattices that can be applied to understand larger non-integrable systems. The study of this basic unit becomes crucial to understand localization mechanisms and dynamical properties of discrete nonlinear saturable systems. We theoretically predict the regions of existence of intermediate solutions, and experimentally confirm it by observing a multi-stable regime.

PACS numbers: 42.65.Wi, 63.20.Pw, 63.20.Ry, 05.45.Yv